UNIVERSITY OF CUKUROVA
INSTITUTE OF NATURAL AND APPLIED SCIENCES

Ph.D. THESIS

Candan DÖZEN ALTUNTAŞ

MEASUREMENT of B_s^0 MESON MASS SPECTRA IN PROTON-PROTON AND LEAD-LEAD COLLISIONS AT $\sqrt{s}$ = 5.02 TeV

DEPARTMENT OF PHYSICS

ADANA-2019

UNIVERSITY OF CUKUROVA

INSTITUTE OF NATURAL AND APPLIED SCIENCES

MEASUREMENT of B_s^0 MESON MASS SPECTRA IN PROTON-PROTON AND LEAD-LEAD COLLISIONS AT $\sqrt{s}$ = 5.02 TeV

Candan DÖZEN ALTUNTAŞ

Ph.D. THESIS

DEPARTMENT OF PHYSICS

We certify that the thesis titled above was reviewed and approved for the award of degree of the Doctor of Physics by the board of jury on 31/01/2019.

....	....	....
Prof. Dr. Ayşe POLATÖZ	Prof. Dr. Eda EŞKUT	Prof. Dr. Sefa ERTÜRK
SUPERVISOR	MEMBER	MEMBER
....	....	
Prof. Dr. İsa DUMANOĞLU	Prof. Dr. Kenan SÖĞÜT	
MEMBER	MEMBER	

This Ph.D.Thesis is performed in Department of Physics of Institute of Natural and Applied Sciences of Çukurova University.
Registration Number:

Prof. Dr. Mustafa GÖK
Director
The Institute of Natural and Applied Sciences

This study was supported by Çukurova University Scientific Research Fund.
Proje No: FEF2011D6

Sevgili Anne ve Babama

ABSTRACT

Ph.D THESIS

MEASUREMENT of B_s^0 MESON MASS SPECTRA IN PROTON-PROTON AND LEAD-LEAD COLLISIONS AT $\sqrt{s}$ = 5.02 TeV

Candan DÖZEN ALTUNTAŞ

DEPARTMENT OF PHYSICS
INSTITUTE OF NATURAL AND APPLIED SCIENCES
UNIVERSITY OF ÇUKUROVA

Supervisor : Prof. Dr. Ayşe POLATÖZ
Co-Supervisor : Senior Research Physicist Samim ERHAN
Year : 2019, Pages : 172
Jury : Prof. Dr. Ayşe POLATÖZ
Prof. Dr. Eda EŞKUT
Prof. Dr. Sefa ERTÜRK
Prof. Dr. İsa DUMANOĞLU
Prof. Dr. Kenan SÖĞÜT

The production cross sections of B_s^0 mesons and their charge conjugates are measured in proton-proton and nucleus-nucleus collisions via the exclusive decay channel $B_s^0 \rightarrow J/\psi\ \phi \rightarrow \mu^+\mu^-\ K^+K^-$ at a center-of-mass energy $\sqrt{s_{NN}}$ = 5.02 TeV per nucleon pair and within the rapidity range ($|y|$ <2.4) using the CMS detector at the LHC. The proton-proton measurement is performed as a function of transverse momentum p_T in the B_s^0 meson transverse momentum range from 7 to 50 GeV/c and compared to the predictions of next-to-leading order perturbative calculations. The B_s^0 production yield in lead-lead collisions is measured in two p_T intervals, 7 to 15 and 15 to 50 GeV/c, and compared to the pp production yield in the same kinematic region.

Key Words: Cross section, B_s^0 Meson, PbPb Collision, CMS

ÖZ

DOKTORA TEZİ

B_s^0 MEZONLARININ $\sqrt{s}$ = 5.02 TeV ENERJİDE PROTON-PROTON VE KURŞUN-KURŞUN ÇARPIŞMALARINDAKİ KÜTLE SPEKTRUM ÖLÇÜMLERİ

Candan DÖZEN ALTUNTAŞ

ÇUKUROVA ÜNİVERSİTESİ
FEN BİLİMLERİ ENSTİTÜSÜ
FiZiK ANABİLİM DALI

Danışman : Prof. Dr. Ayşe POLATÖZ
İkinci Danışman : Kıdemli Araştırmacı Fizikçi Samim ERHAN
Yıl : 2019, Sayfa : 172
Jüri : Prof. Dr. Ayşe POLATÖZ
Prof. Dr. Eda EŞKUT
Prof. Dr. Sefa ERTÜRK
Prof. Dr. İsa DUMANOĞLU
Prof. Dr. Kenan SÖĞÜT

B_s^0 mezonlarının üretim tesir kesitleri, LHC nin CMS deneyinde $\sqrt{s_{NN}}$ = 5.02 TeV enerjide proton-proton ve çekirdek-çekirdek çarpışmalarında rapidite aralığı ($|y|$ <2.4) alınarak $B_s^0 \to J/\psi\, \phi \to \mu^+\mu^-\ K^+K^-$ bozunum kanalı için ölçülmüştür. Proton-proton çarpışmalarında tesir kesiti ölçümü B_s^0 mezonlarının enine momentum aralığı 7-50 GeV/c alınarak hesaplanmış ve elde edilen sonuçlar next-to-leading order perturbative hesaplamalar ile karşılaştırılmıştır. Kurşun-kurşun çarpışmalarında B_s^0 üretimi 7-15 ve 15-50 GeV/c olmak üzere iki farklı p_T aralığı kullanılarak hesaplanmış ve aynı kinematik seçimlerde proton-proton çarpışmalarından elde edilen sonuçlar ile karşılaştırılmıştır.

Anahtar Kelimeler: Tesir kesiti, B_s^0 Meson, PbPb Çarpışmaları, CMS

GENİŞLETİLMİŞ ÖZET

Doğanın birleşik bir tanımını bulmak için parçacık fiziği maddenin en küçük bileşenleri ve bunlar arasındaki temel kuvvetleri inceler. Standart Model (SM) maddeyi oluşturan temel parçacıklar ve bu parçacıklar arasındaki etkileşimleri açıklayan bir kuramdır. Bu kurama göre yukarı (u), aşağı (d), çekici (c), garıp (s), üst (t) ve alt (b) olmak üzere altı farklı çeşni kuark bulunmaktadır.

Çekici ve alt kuarkları içeren ağır çeşnili hadronlar, Kuantum Renk Dinamiğinin (KRD) çeşitli yönlerini anlamak için gerekli araçlardan biridir. Ayrıca, ağır iyon çarpışmalarında, ağır çeşnili mezonlar, bu çarpışmalarda üretilen Kuark-Gluon Plasma (KGP) olarak bilinen sıcak ve yoğun ortamın araştırılmasında çok önemli bir rol oynamaktadır. Ağır kuark üretimi, ağır iyon çarpışmalarının ilk aşamalarında meydana gelir ve bu nedenle, KGP'nin özellikleri hakkında bilgi taşırlar. Hafif kuarklar ve gluonlarla karşılaştırıldığında ağır kuarkların daha küçük renk yükü taşımaları nedeniyle daha az enerji kaybetmeleri beklenir.

Güçlü etkileşimdeki parçacıklar sıcak ve yoğun kuark gluon plazmasını oluşturulurlar. Bu durum, ağır çekirdeklerin yüksek enerjili çarpışmalarında ulaşılan şartlarla yaratılabilmektedir. Zamanla bu sıcak ortam soğumaya başlar ve hadronizasyon sürecinin ardından genişler. Ağır kuark çarpışmasının ilk aşamasında kuark-karşıt quark çiftleri üretilir. Bu sıcak ve yoğun ortam içinde ağır quarklar ortamdaki parçacıklarla çarpışma süreçlerinden ve gluon ışımasından dolayı enerji kaybederler. Bu kayıp enerji, ağır çekirdekli çarpışmalarda (PbPb veya AuAu) proton-proton (pp) çarpışmaları ölçek alınarak hesaplanan dik momentum dağılımının modifikasyonu ile açıklanabilir. Bu Nükleer Modifikasyon Faktörü (NMF) çekirdek-çekirdek çarpışmalarındaki tesir kesitinin pp çarpışmalarından elde edilen tesir kesitine oranı olarak hesaplanır. Bu oranın 1'e yakın çıkması durumunda pp ve PbPb çarpışmalarında herhangi bir nükleer etkinin olmadığı, 1'den küçük olması durumunda B_s^0 parçacıklarının baskılanmasının ortaya çıktığı ve 1'den büyük olması durumunda ise çoklu etkileşimlerin gerçekleştiği sonucuna varılır.

Bu olayın bir sonucu olarak, çeşitli kuramsal hesaplamalar, merkezi PbPb çarpışmalarında, hafif parçacıkların enerji spektrumlarında, çekici ve alt mezonlarınkine oranla önemli farklılıklar olduğunu öne sürmektedir. Kompakt Muon Solenoid (CMS) Büyük Hadron Çarpıştırıcısının (BHÇ) yüksek ışınlılık ile elde ettiği pp ve PbPb çarpışmalarından alınan veriler ile yüklü parçacıkların nükleer modifikasyon faktörünü kullanarak bu enerji farklılığını açıklama özelliğine sahiptir. Her iki çarpışmadan elde edilen hesaplamalar sonucunda geniş açısal momentum aralığında (2GeV-100GeV) benzer sonuçlar elde edilmektedir.

Bu çalısmanın amacı, B_s^0 mezonlarının üretim tesir kesitlerini pp ve PbPb çarpışmalarında hesaplayarak, alt (b) kuarkların hadronizasyonunu ve çeşnilere bağlı enerji kaybını ölçmektir.

Ayrıca, ağır iyon çarpışmalarında B_s^0 parçacıklarının baskılanmasının ölçümü, hadronizasyon mekanizmasını anlamakta önemli rol oynamaktadır.

B_s^0 mezonun üretiminin ölçümü, zayıf kuvvetlerin araştırılması ve madde antimadde asimetrisinden kaynaklanan SM tarafından öngörülmeyen yeni parçacık ve kuvvetleri gözleme olanağı sağlamaktadır..

B_s^0 mezonlarının üretim tesir kesitleri, BHÇ' nin CMS deneyinde 2015 yılında $\sqrt{s_{NN}}$ = 5.02 TeV'lik kütle merkezi enerjisinde pp ve PbPb çarpışmalarından elde edilen veriler kullanılarak ve ($|y|$ <2.4) rapidite aralığında, dallanma oranı $B = (3.12 \pm 0.24) \times 10^{-5}$ olan $B_s^0 \rightarrow J/\psi\ \phi \rightarrow \mu^+\mu^-\ K^+K^-$ bozunum kanalı için ölçülmüştür.

pp çarpışmalarında tesir kesiti ölçümü B_s^0 mezonlarının dik momentum aralığı 7-50 GeV/c alınarak hesaplanmış ve elde edilen sonuçlar kuramsal hesaplamalar (FONLL: Fixed Order Next to Leading Logarithms) ile karşılaştırılmıştır. PbPb çarpışmalarında B_s^0 üretimi 7-15 ve 15-50 GeV/c olmak üzere iki farklı p_T aralığı kullanılarak hesaplanmış ve aynı kinematik seçimlerde pp çarpışmalarından elde edilen sonuçlar ile karşılaştırıp son olarak B_s^0 mezonları için nükleer modifikasyon faktörü hesaplanmıstır. Buna ek olarak B_s^0 mezonu ile B^+ mezonunun nükleer modifikasyon karşılaştırılmaları hem PbPb hemde pp çarpışmaları için hesaplanmış ve PbPb çarpışmalarındakı nükleer etkilerin pp çarpışmalarına oranla beklenildiği gibi daha baskın olduğu görülmüştür.

ACKNOWLEDGEMENTS

The research study presented in this dissertation would not have been possible without my close association with many people. I take this opportunity to extend my sincere gratitude and appreciation to all those who made this PhD. thesis possible.

First and foremost, I am extremely grateful to my amazing family for their love, support, and constant encouragement I have gotten over the years. In particular, my heartfelt gratitude to my husband Bahadır Altuntaş and our four leg friend Evaa for their unwavering support, patience, sacrifices and being always by my side in any condition. They are the salt of the earth, and I undoubtedly could not have done this without them.

I would like to to express my sincere gratitude to my supervisor, Prof. Ayşe Polatöz for her guidance, continues support, patience, motivation, enthusiasm, and immense knowledge over the years. She has set an example of excellence as a researcher, mentor, and instructor.

I would also like to thank my committee members, Prof. Eda Eşkut, Prof. İsa Dumanoğlu, Prof. Sefa Ertürk, and Prof. Kenan Söğüt for their time, comments and suggestions.

Thanks to the funding agency, Turkish Atomic Energy Authority to be sponsored.

My special words of thanks should also go to Samim Erhan for his guidance, wisdom, persistent help and encouraging my research. I would also like to a special thank Gulsen Önengüt and Aysel Kayış Topaksu for her constructive suggestions. Their advice on both research as well as on my career have been invaluable.

I would like to express my deepest appreciation to Hyunchul Kim and Zekeriya Uysal, for all of their guidance through this process; commitment to collaboration, their discussion, ideas, and feedback have been absolutely invaluable. I owe my deepest gratitude to Adriana Milic and Sinem Şimşek, for their fruitful friendship and insightful comments.

To my colleagues and friends, Gül Gökbulut, Fatma Boran, Furkan Dölek and Uğur Kiminsu and Özgün Kara I thank them for their companionship and for supporting me along the way. The moments of leisure shared together helped to overcome some more difficult moments.

CONTENTS **PAGE**

LIST OF TABLES **PAGE**

LIST OF FIGURES **PAGE**

ABBREVATIONS

σ	: Cross Section
ATLAS	: A Toroidal LHC ApparatuS
B_s^0	: Neutral B meson which includes strange quark
CMS	: Compact Muon Selenoid
CERN	: Conceil Europeenne pour la Recherche Nucleaire
DAQ	: Data Acquisition
ECAL	: Electromagnetic Calorimeter
HCAL	: Hadronic Calorimeter
LHC	: Large Hadronic Collider
FONLL	: Fixed Order Next to Leading Logarithm

XXXVIII

1. INTRODUCTION

Heavy flavor hadrons containing charm and beauty quarks provide one of the essential tools to understand the various aspect of Quantum Chromodynamics (QCD). Furthermore, in heavy-ion collisions, heavy-flavour mesons play a crucial role as they have long been proposed as ideal probes of the hot and deconfined medium, known as Quark-Gluon Plasma (QGP), which is produced in such collisions. Heavy quarks production occurs in the very first stages of heavy-ion collisions, and therefore they carry information about the prethermalization properties of the QGP. The heavy quarks are expected to lose less energy due to smaller colour charge and the dead cone effect (Dokshitzer and Kharzeev, 2001) by comparison with light quarks and gluons. As a consequence of this phenomenon, several theoretical calculations predict sizable differences in the suppression pattern of light particle versus that of charmed and beauty mesons, in central Lead-Lead (PbPb) collisions. The Compact Muon Solenoid (CMS) collaboration was able to measure the nuclear modification factor (R_{AA}) of charged particles with using the high luminosity LHC runs of proton-proton (pp) and lead-lead (PbPb) collisions (CMS Collaboration, 2016b). The two measurements show a very similar suppression in a vast transverse momentum interval (from 2 to 100 GeV/c). This study aims to test the flavour dependence of energy loss and the hadronisation of beauty quark, by measuring the exclusive production of B_s^0 mesons in PbPb collisions in a similar kinematic range ($7 < p_T < 50$ GeV/c). The measurement of the suppression of strange beauty particles in heavy ion collisions is also vital to understand the mechanism of beauty hadronisation. In the presence of a medium with increased strangeness content, the relative yield of B_s^0 mesons with respect to non-strange beauty mesons at low-intermediate p_T can be enhanced in nucleus-nucleus collisions as compared to pp interactions if recombination is a relevant mechanism of beauty hadronisation in the QGP.

This thesis describes the production of heavy-flavour in heavy-ion collisions. In particular, the analysis of the B_s^0 meson transverse momentum spectra in pp and PbPb collisions at the centre-of-mass energy 5.02 TeV is presented. The measurement of the production of B_s^0 mesons probes the weak interaction and includes the possibility to observe sizable particle anti-particle asymmetries caused by heavy particles and new forces between them which are not predicted by the Standart Model (SM).

The analysis has been performed on the both pp and PbPb data collected by CMS, through the full reconstruction of the decay channel $B_s^0 \rightarrow J/\psi\, \phi$ with branching fraction $B = (3.12 \pm 0.24) \times 10^{-5}$ in rapidity region $|\eta| < 2.4$. The J/ψ is reconstructed in the $\mu^+ \ \mu_-$ decay channel and ϕ is reconstructed to K^+K^-. The pp B_s^0 differential cross section is also presented. Besides, the R_{AA}, described as the ratio of B_s^0 cross-sections in pp and PbPb scaled by the number of nucleon-nucleon scattering, is represented in the centrality range 0-100%.

The results have finally been compared to Fixed Order Next to Leading Logarithms (FONLL) calculations (Cacciari, 1998) (expectations from scaled pp collisions) at the same centre-of-mass energy to study possible modifications of the production.

The results are presented for the data recorded during the year 2015 with the CMS. It is designed to explore a wide range of physics in pp and PbPb collisions. The analysis presented here assess and benchmark the performance of a variety of detector components including track and muon reconstruction. For reconstruction of long-lived particles, like the b hadrons, the silicon pixel detector provides the most significant information.

2. THEORETICAL OVERVIEW

2.1. Standard Model (SM) of Particle Physics

The SM is a quantum field theory which describes the elementary particles and their interactions including three of the four fundamental forces in physics: the weak force, the strong force, and the electromagnetic force, with the gravity the notable exception. The SM is classified with twelve fermion fields (spin-1/2 matter particles, quarks and leptons) and twelve gauge boson fields (spin-1 force carriers, eight gluons, (W^+, W^-, Z^0 and γ) as well as a complex scalar doublet field (the Higgs boson). All the fundamental particles in the SM that have been experimentally observed and their interactions are represented in Figure 2.1.. Quarks are categorized based on their electric charge (up-type (Q=+2/3) and down-type (Q=-1/3)) and for each quark there exists a charge conjugated anti-quark. The up-type quarks consist of the up (u), top (t) and charm (c) whereas the down-type quarks contain the down (d), bottom (b) and strange (s) quarks. Leptons can be classified into three different flavours: the electron (e), the muon (μ), and the tau (τ), each with a flavour-specific neutrino (ν_e, ν_μ and ν_τ) and all leptons have corresponding antiparticles. While neutrinos have no electrical charge, electrons, muons and taus have one unit of electrical charge.

The second category of fundamental particles, the gauge bosons, are the force carriers between the four fundamental forces in physics. The electromagnetism is described by Quantum Electrodynamics (QED) and responsible for phenomena including electricity, magnetism, the structure of matter as well as the chemical interactions. The electromagnetic force is a long-range force and decreasing proportionally to the square of the distance between charged particle interaction. The charge of the interaction is called electric charge and its mediator is a neutral and massless photon (gamma) and couples to all of the charged fermions.

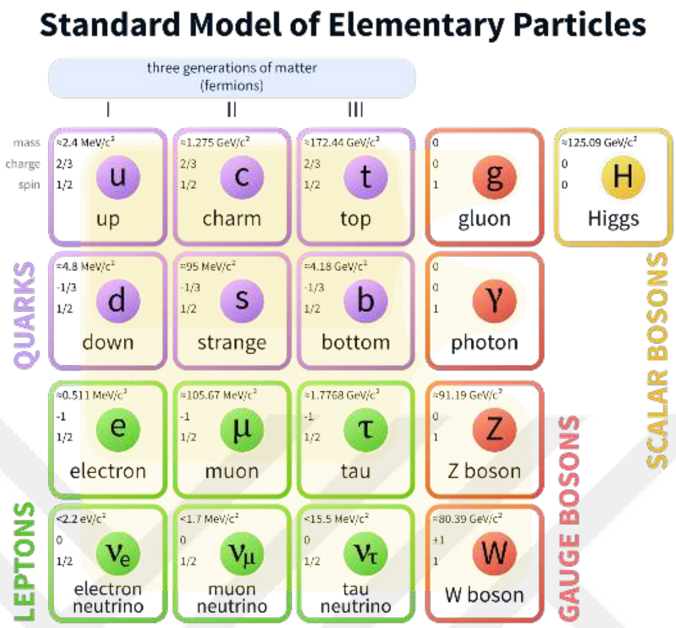

Figure 2.1. The particle content of the SM (Wiki, 2018)

The weak interaction is a short-range force due to the mediator particles, $W^{\pm}$ and Z^0, are massive. All elementary particles participate in the weak interaction via charged W or neutral Z^0 . The charge of the weak interaction is called weak isospin and the weak force can change quark flavour. The electromagnetic and weak interactions are indistinguishable at higher energies and can be unified by a single electroweak theory with the electric and flavour charges combined into a single weak "hypercharge".

The strong interaction is well defined by the QCD and mediated by exchanges of the massless gluons. It is responsible for holding the quarks together in particles. There are two types of quark combinations are established as existing in nature: quark anti-quark pair state (q $\bar{q}$) called mesons and three-quark state (qqq) called baryon. The quantum numbers of the hadrons are determined by quarks which are called valence quarks. Each hadron may contain an indefinite number of virtual (sea) quarks, antiquarks, and gluons which do not influence the quantum numbers. The sea quarks dominate the dynamics of hadrons in reactions at high energies, while at energies below 10 GeV the valence quarks are dominated. The B_s^0 mesons are composed of the valence quarks anti-b and s (strange) quark combinations. The corresponding anti B_s^0 meson consists of a b and an anti-s quarks). As an example of baryons, proton and neutron, composed of uud and udd valence quark combinations, respectively. The proton components are shown in Figure 2.2.

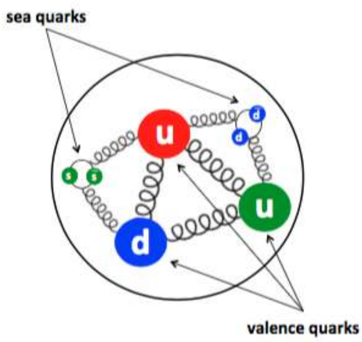

Figure 2.2. Proton constituents

The presence of multiple quarks with the same quantum numbers is possible in baryons. However, this violates the Pauli exclusion principle for identical fermions. In order to avoid this, a new degree of freedom called colour charge was introduced by Greenberg (1964). This charge is the source of the inter-quark force or called colour force. Each quarks contains color values 'red', 'green' or 'blue' (R, G, B), and for antiquarks the color values are 'anti-red', 'anti-green' or 'anti-blue' ($\bar{R}$, $\bar{G}$, $\bar{B}$). Additionally, the neutral combinations of colour charges can be formed from either a colour with its anti-colour or the sum of all three colours or anti-colours: $R\bar{R} = G\bar{G} = B\bar{B} = RGB = \bar{R}\bar{G}\bar{B}=0$.

The last particle in the SM is the Higgs boson, a neutral scalar particle. which is responsible to give mass to the heavy gauge bosons and the rest of the particles. The Higgs boson has been discovered recently by the ATLAS and CMS Collaborations in July 2012 with a mass of 125.09 GeV (Aad et al., 2012; Aad et al., 2015; Chartchyan et al., 2012).

Although the SM is very successful theory which has been observed experimentally very precisely, there are some phenomena can not be explained within the SM framework. The SM is inconsistent with the theory of gravitation described by general relativity. Another open question raises from the nature of the electroweak symmetry breaking which is related to a hierarchy problem. Furthermore, SM can not explain the matter/antimatter asymmetry observed in the universe. In addition, the SM does not explain the dark matter and dark energy.

2.2. Heavy quark production at the Large Hadron Collider (LHC)

The heavy quark production measurements in high energy hadronic interactions are important tests of QCD. The collisions at the LHC produce b and anti b ($\bar{b}$) quark pairs which combine with other quarks to form B mesons. The QCD theory well describes the primary collision between hadron constituents. It is categorized according to variables that define the momentum and angular ranges of the reaction products:

- The transverse momentump_T is the momentum in the plane perpendicular to the direction of the collisions,
- The pseudo-rapidity (θ) is the spatial coordinate that describes the angle of a particle relative to the beam direction. It is expressed by the following equation:

$$\eta = -ln[tan(\frac{\theta}{2})], \tag{2.1}$$

where θ is the angle between the beam direction and the particle momentum $\vec{p}$.

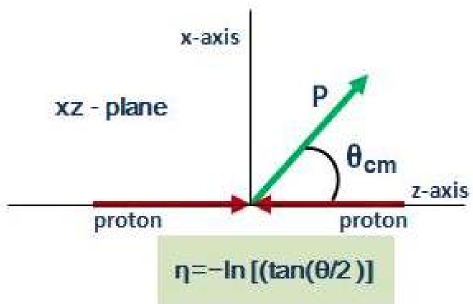

Figure 2.3. The pseudo-rapidity (Xabier Cid Vidal, 2018)

Since the particle production is constant as function of θ, in hadron collider physics, the pseudo-rapidity is preferred over rapidity.

The B_s^0 mesons are produced with two separate production processes, $b\bar{b}$ quark pair production and hadronisation,

- $b\bar{b}$ quark pairs are produced at the collisions through elementary quark or gluon processes,
- The hadronisation stage which are more complex quark combinations, b-quarks separate and turn into hadrons.

The hadronisation process starts when a $b\bar{b}$ quark pair is produced. In case of a single quark or gluon is not observed, the quarks could permanently confine within hadrons which is called as quark confinement by the QCD property. As two quarks separate, the potential energy due to the colour force attraction between them increases until it is more energetically sufficient to generate a virtual quark anti-quark pair from the vacuum sea into physical reality. This process creates hadrons with constituent b-quarks (b-hadrons). The $b\bar{b}$ quark pair production is shown in Figure 2.4.

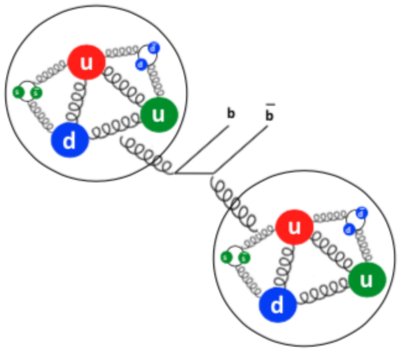

Figure 2.4. Hadron production from the interaction between gluons at LHC. The constituent quarks in different colors (uud) and the sea quarks and gluons are shown (Cerizza, 2012)

The heavy quark productions are special interest because it helps to understand the mechanisms of heavy quark interaction at the very high temperature and density medium created in heavy ion collisions. Since the heavy quarks (charm and bottom quarks) are primarily produced at the early stage of heavy ion collisions, they carry information about the pre-thermalization properties of the QGP. In contrast to light quarks and gluons, the heavy quarks are expected to lose less energy because of the smaller colour charge and the dead cone effect (Dokshitzer and Kharzeev, 2001). The study of the exclusive production of B_s^0 mesons in PbPb collisions provides for testing the flavour dependence of energy loss. Furthermore, the suppression of strange beauty particles measurement in heavy-ion collisions is considered of fundamental importance to study the mechanisms of beauty hadronisation. In the presence of a medium with increased strangeness content, the relative yield of B_s^0 mesons concerning non-strange beauty mesons at low intermediate p_T can be enhanced in nucleus-nucleus collisions as compared to pp interactions if recombination is a relevant mechanism of beauty hadronisation in the QGP.

2.3. B Mesons

In particle physics, B mesons are bound states of a b quark and light anti-quark. The binding among the quarks is provided by the strong interaction whereas B mesons can only decay by the weak interaction. The list of B mesons and their quarks contents are represented in Table 2.1. (Wikimedia, 2018)

Table 2.1. List of B mesons

Particle	Symbol	Anti-particle	Quark content	Charge	Rest Mass (MeVc^2)	Mean Lifetime(s)
B meson	B^+	B^-	$u\bar{b}$	+1	5279.29 ± 0.15	$(1.638 \pm 0.004) \times 10^{-12}$
B meson	B^0	$\bar{B}^0$	$d\bar{b}$	0	5279.61 ± 0.16	$(1.520 \pm 0.004) \times 10^{-12}$
Strange B meson	B_s^0	$\bar{B}_s^0$	$s\bar{b}$	0	5366.79 ± 0.23	$(1.510 \pm 0.005) \times 10^{-12}$
Charmed B meson	B_c^+	$\bar{B}_c^-$	$c\bar{b}$	+1	6275.1 ± 1.0	$(0.507 \pm 0.009) \times 10^{-12}$

2.3.1. The $B_s^0 \to J/\psi\ \phi(1020)$ Decay

This dissertation focuses on the B_s^0 meson decay into the J/ψ ($c\bar{c}$) and ϕ ($s\bar{s}$) particles. The decay diagrams of the $B_s^0 \to J/\psi\phi$ are presented in Figure 2.5..

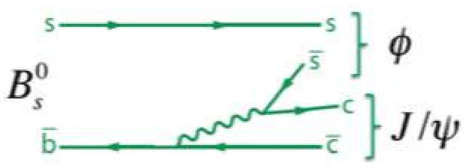

Figure 2.5. The tree-level Feynman diagrams for the B_s^0 meson decay into J/ψ and ϕ. The quark pair $c\bar{c}$ and $s\bar{s}$ form the J/ψ and ϕ particles, respectively.

The final state $J/\psi\ \phi(1020)$ is analyzed with the J/ψ decays to a muon pair($\mu^+\mu^-$) and $\phi(1020)$ decaying to $K^+\ K^-$. The possible additional contributions from the B meson decays are also considered and analyzed as well. The detailed information about these contributions can be found in Section 4.14..

In this dissertation, the measurement of the B_s^0 meson transverse momentum (p_T)spectra in pp and PbPb collisions at 5.02 TeV is studied. The B_s^0 mesons production is measured in rapidity region $|\eta| < 2.4$, via the full reconstruction of the decay channel of $B_s^0 \to J/\psi\ \phi$ with branching fraction,

$$\mathrm{BR}(B_s^0 \to J/\psi\phi) = (3.12 \pm 0.24) \times 10^{-5}. \tag{2.2}$$

Furthermore, the pp B_s^0 differential cross section is measured and compared to theoretical calculations. Besides that, the nuclear modification factor which is defined as the ratio of B_s^0 cross-section in PbPb and pp collisions scaled by the number of nucleon-nucleon scattering are represented.

3. EXPERIMENTAL APPARATUS

3.1. The LHC and CMS Experiment

The LHC (LHC, 1995) is the largest and most powerful pp collider for High Energy Physics (HEP). It was installed in an existing 27 km long underground tunnel near Geneva, Switzerland. The LHC accelerate and collide proton beams at a center of mass energy of $\sqrt{s}$ = 14 TeV with instantaneous luminosity of L =$10^{34} cm^{-2} s^{-1}$. Some of the motivations for the construction of the LHC is to shed light on the possible new phenomena beyond the SM (Turner, 1998), the nature of electroweak symmetry breaking and it led to the discovery of the Higgs boson (CMS Collaboration, 2016c), (Atlas Collaboration, 2016).

Furthermore, the LHC is able to accelerate and collide beam of heavy ions (lead:Pb) with a center of mass energy of $\sqrt{s}$= 2.76 TeV per nucleon and a design luminosity of $10^{27} cm^{-2} s^{-1}$. Heavy ion collisions produce a QGP as it was present in the first moments of the universe which will help to further investigate the properties of the strong interaction (Florian, 2012) which binds quarks together to mesons and hadrons.

The particles are accelerated in two beams in opposite direction before they are brought collision in the four different interaction points that host four of the LHC experiments: CMS (CMS Collabration, 2008), ATLAS (Atlas Collaboration, 2008), ALICE (Alice Collaboration, 2008), and LHCb (LHCb Collaboration, 2008). CMS and ATLAS are general purpose experiments which examine a wide range of physics at the TeV scale like extra dimensions, SuperSymmetry (SUSY), dark matter, and string theory. One of their main goals has already been reached: to find the Higgs boson. LHC beauty (LHCb) focuses on the physics of the b-quark to understand the matter and antimatter asymmetries in the universe. A Large Ion Collider Experiment

(ALICE) studies lead-ion collisions to produce QGP.

The accelerator complex at CERN, shown in Figure 3.1., consists of linear and circular accelerators which accelerate particles to increasingly higher energies. The energy of a beam of particles is boosted by each accelerator before the beam is injected from one machine to the next.

The proton beam starts from a bottle of hydrogen gas and to extract the protons, an electric field is applied to strip hydrogen atoms of their electrons. The protons are accelerated with a time-dependent electric field applied to Radio-Frequency (RF) cavities in the Linear Accelerator 2 (LINAC 2) (Tronc, 2002).

The LINAC2 boosts the particles energies up to 50 MeV. The protons are then sent to the Proton Synchrotron Booster (PSB) (LHC, 1995; Evans and Bryant, 2008) the first circular accelerator in the chain, the energy to increases to 1.4 GeV, followed by the Proton Synchrotron (PS) (LHC, 1995; Evans and Bryant, 2008) where the energy of the particles reaches 25 GeV. The beam of particles is then fed to the Super Proton Synchrotron (SPS) (LHC, 1995; Evans and Bryant, 2008) where it is accelerated to 450 GeV. Afterwards, it is injected into the LHC, in clockwise and anticlockwise direction, where it reaches its nominal energy of 7 TeV.

The LHC accelerates only one type of lead, namely Pb(208). The lead ion beams start with a piece of pure lead. A small number of atoms are vaporised by heating them to about 500°C. In order to create ions, a few of the electrons from each atom are removed by an electrical current. The newly created ions start to travel from a linear accelerator called LINAC 3 (Tronc, 2002) which boosts the energy to 4.5 MeV per nucleon. The ions are then sent to the Low Energy Ion Ring (LEIR) (Chanel, 2002) which allows an increase of the energy to 72 MeV per nucleon. Vaporization and acceleration in LINAC 3 and LEIR are the only different stages in the acceleration process for ions. After they leave the LEIR they pass through the PS and then SPS where the lead ions reach their energy of 5.9 GeV and 177 GeV per nucleon, respectively. They are finally injected into the LHC in two opposite directions and reach energies of up to 1.38 TeV (1380 GeV) per nucleon before they are brought to collision.

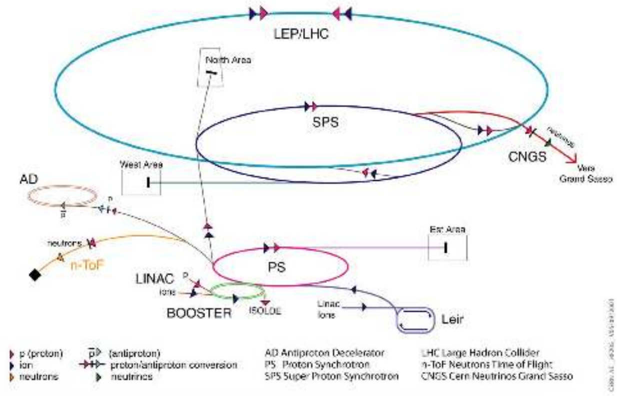

Figure 3.1. The accelerator chain at the CERN complex. The arrows show the direction of beams in the accelerators and the energy of the beam at these points. Filled circles show the locations of the four major detectors on the LHC (Haffner, 2013).

3.2. The Large Hadron Collider (LHC)

In the LHC, each beam is composed of bunches which contains about 10^{11} protons. Superconducting magnets guide the bunches of protons with a magnetic field of 8.3 T operated at a temperature of 1.9 K and cooled by liquid helium. The dipole magnets allow the charged particles to bend while quadrupole magnets focus the beam around the ring. The list of LHC parameters is shown in Table 3.1. (Bruning, 2004; Evans and Bryant, 2008).

After reaching the nominal energy of 7 TeV, the protons collide every 25 ns at the collision points where CMS, ATLAS, LHCb and ALICE experiments are located. Operating the LHC at the energy scale of TeV leads to the generation of new particles.

Table 3.1. List of common LHC parameters

Circumference	26659 m
Dipole operating temperature	1.9 K ($-271.3°C$)
Number of magnets	9593
Number of main dipoles	1232
Number of main quadrupoles	392
Number of RF cavities	8 per beam
Nominal energy, protons	7 TeV
Nominal energy, ions (per nucleon)	2.76 TeV/u
Peak magnetic dipole field	8.33 T
Min. distance per bunches	$\sim$7 m
Design luminosity	$10^{34}cm^{-2}s^{-1}$
No. of bunches per proton beam	2808
No. of protons per bunch (at start)	1.1×10^{11}
Collision rate	40 MHz
RMS beam size	16.7 μm

In addition to the collision energy, the number of head-on interactions (events) plays a crucial role in accelerating physics. Measuring the ability of the particle accelerator to produce the required number of interactions is defined by the Luminosity. Luminosity (L) can be expressed as a proportionality factor between the number of events per second and the cross section σ which can be defined as an effective area assigned to two colliding particles.

$$\frac{dN_x}{dt} = \sigma_x \times L \tag{3.1}$$

where L is in units of $cm^{-2}s^{-1}$ while σ is expressed in barns, 1 barn = $10^{24}cm^{-2}s^{-1}$. In order to define the number of observed events in an experiment, the integrated luminosity is used. The integrated luminosity is defined as the integral of the instantaneous luminosity over time and can be formulated as follows:

$$L_{int} = \int L dt \tag{3.2}$$

The total amount of events N generated in a particular reaction can be defined as:

$$N = \sigma \int L dt \tag{3.3}$$

The main aim of a collider experiment is to maximize the integrated luminosity to collect as much data as possible available for physics analyses. During the year 2012 the instantaneous luminosity reached values of L = $7.67\times10^{33} cm^{-2}s^{-1}$ with a 50 ns bunch spacing. In 2015, the maximum luminosity reached values of L $\approx$ $5\times10^{33} cm^{-2}s^{-1}$ with a 25 ns bunch spacing. In Figure 3.2., the delivered luminosity versus time from 2010 to 2016 for pp data is shown (Lujan, 2018).

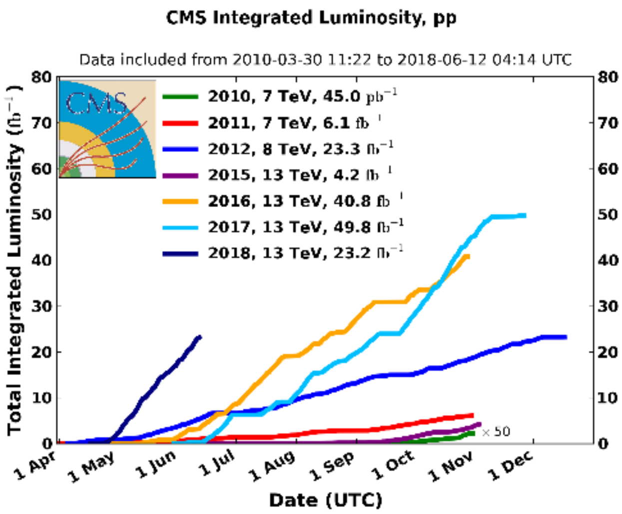

Figure 3.2. Delivered Luminosity versus time for 2010, 2011,2012, 2015 and 2016 for pp data only.The green, red, blue, purple and yellow colours refers to years 2010, 2011, 2012, 2015 and 2016, respectively.

In 2015, the operation of the LHC started with a bunch spacing of 50 ns and was then switched to 25 ns bunch spacing. The values for the integrated luminosities for both pp and PbPb collisions recorded by the CMS experiment in 2015 are shown in Figure 3.3.

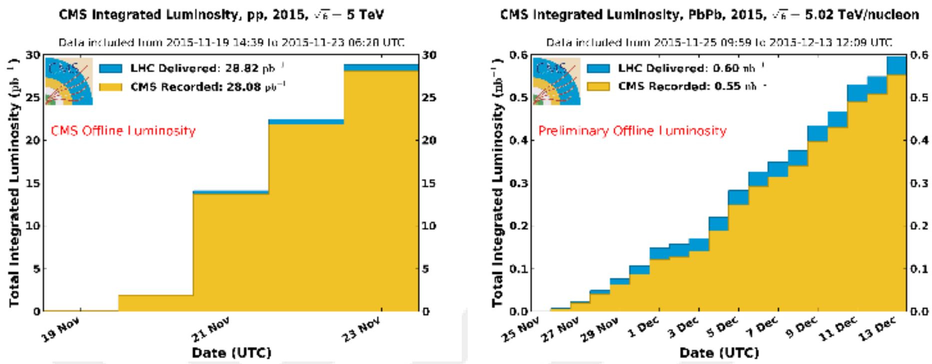

Figure 3.3. Total Integrated Luminosity for pp (left) and PbPb (right) as a function of days as recorded by the LHC (in blue) and by CMS (in yellow) at 5.02 TeV centre of mass energy in 2015.

3.3. The CMS Experiment

The CMS stands for Compact Muon Solenoid is a multi-purpose particle detector which is designed to explore a wide range of particles and phenomena generated in high energy collisions at the LHC. The CMS detector structure is based on sub-detectors which are located around the beam pipe in a cylindrical onion-like shape as shown in Figure 3.4.. The purpose of this geometry is to cover the whole interaction region. The sub-detectors consist of layers of material which absorb particles and measure their energy and momentum.

From inside out, the sub-detectors are the tracking system (Karimaki, 1997), which consists of the pixel detector and silicon tracker, the Electromagnetic Calorimeter (ECAL) has a high resolution to detect and measure electrons and photons, the Hadron Calorimeter (HCAL) measures the energy of hadrons. All sub-detectors are surrounded by a superconducting solenoid magnet, followed by the muon system and

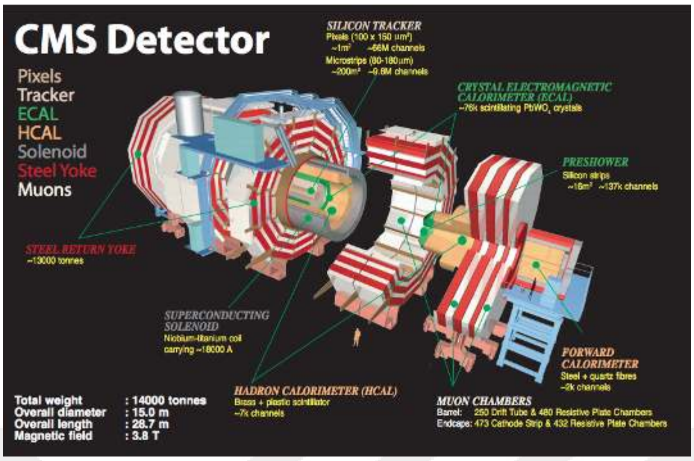

Figure 3.4. A perspective view of the CMS detector with all the internal sub-detectors including their names and some characteristic features also indicated (CMS Collaboration, 2010).

the iron yoke that controls the magnetic flux return. For easy construction and maintenance, the CMS detector was designed in fifteen separate slices which were built and tested on the surface and lowered down into the cavern.

3.3.1. Coordinate System

The CMS coordinate system is a right-handed reference system. The nominal interaction point is taken as the origin. The x-axis is defined as radially inward in the direction of the centre of the LHC, while the y-axis points vertically up towards the surface. The z-axis is pointing along the rotational axis of the detector towards the beam direction. The azimuthal angle φ is measured from the x-axis. The radial distance r is defined in the x-y plane. The polar angle regarding the beam axis is denoted by θ and is measured from the positive z-axis. The function of the production angle θ with respect to the positive z-axis is defined as pseudorapidity η which characterises the boost of the particles:

$$\eta = -ln(tan\theta/2) \tag{3.4}$$

where $-\eta$ is preferred over θ due to fact that it is Lorentz invariant for massless particles under boosts along the z-direction.

Figure 3.5. shows the relation between polar angle and pseudorapidity. These variables also allow defining the transverse momentum of particles $p_T = |p|cos\theta$ and the angular separation between two objects $\Delta R = \sqrt{(\Delta\eta)^2 + (\Delta\phi)^2}$.

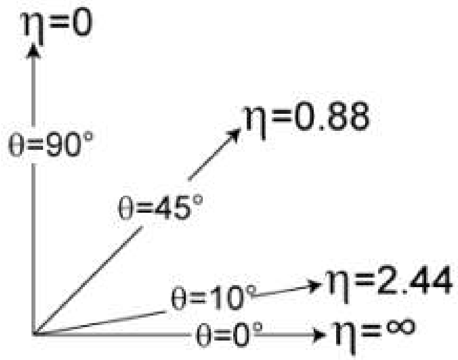

Figure 3.5. The relation between polar angle and pseudorapidity is inverse proportional. η goes towards infinity for small angles whereas θ approaches zero.

3.3.2. Superconducting Solenoid Magnet

The superconducting solenoid magnet is the central element of the CMS experiment. It is designed not only to produce a high magnetic field of 4 Tesla but also to preserve a highly uniform field. The CMS magnet (CMS Collaboration, 1997) is constructed of superconducting Niobium Titanium (NbTi) coils. The CMS solenoid has an active length of 12.5 m with an outer diameter of 6.9 m which surrounds the silicon tracker and both ECAL and HCAL. The muon system envelopes the magnet coils within a twelve-sided iron structure which guides the magnetic field. Additionally, the return yoke also acts as a filter by allowing only muons and weakly interacting particles like neutrinos to pass through. Due to the magnetic field, the paths of particles are bent in accordance with their mass and charge. The curvature of the particles tracks provide a high precision measurement of their momentum, their charge, as well as the determination of the particle positions in the tracker and the muon detectors.

3.3.3. Tracking System

The inner tracking system is located in the innermost part of the CMS detector surrounding the interaction point. At the LHC design luminosity of $10^{24} cm^{-2} s^{-1}$ there is a large amount of particles from pp interactions passing through the tracker system. To have a precise measurement with high track multiplicities, ten layers of silicon microstrip detectors are used. In addition, three layers of pixel detector improve the impact parameter of charged-particle tracks and the position of secondary vertices. An overview of the tracking system in the r-z plane is shown in Figure 3.6.

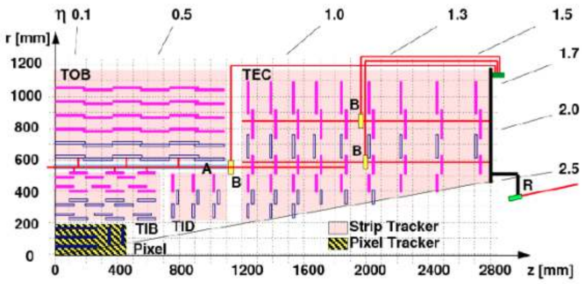

Figure 3.6. Schematic cross-section of one quarter of the CMS tracker in the r-z plane. The hashed yellow area represents the pixel detector which is located in the lower left corner. The strip tracker is placed around the pixel detector and is shown in pink (Chartchyan, 2010).

3.3.4. Pixel Detector

The pixel detectors are located in the innermost region of the tracking system, and it covers a pseudorapidity range $|\eta| < 2.5$. It contains 1440 pixel modules which are organised in three barrel layers (Barrel pixel: BPIX) with two endcap disks (Forward pixel: FPIX) as shown in Figure 3.7..

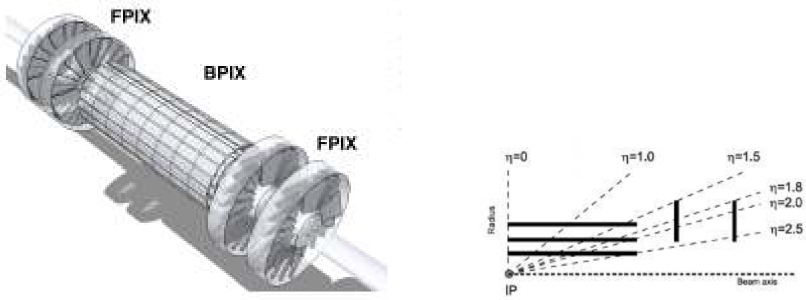

Figure 3.7. A schematic overview of the Pixel detector (left) and the geometrical layout of the pixel detector with hit coverage as a function of the pseudorapidity (right). IP refers to interaction point.

The barrel layers surround the interaction point with a radius in between 4.4 cm and 10.2 cm. The forward pixels are positioned 6-15 cm from the interaction point. With this layout, the pixel detector provides a 2D point with a resolution of 10 -15 μm. Hence, it can measure three tracking points for charged particles within the covered pseudorapidity range. Besides, it provides precise information for measuring secondary vertices from b-mesons and tau decays, as well as forming seed tracks for outer track reconstruction (CMS Collaboration, 1998).

3.3.4.1. Silicon Strip Tracker

The silicon strip detectors placed in the outer region of the tracking system and it surrounds the pixel detector at a radial distance of 20 cm up to 116 cm from the collision point. The strip tracker consists of four different modules: the Tracker Inner Barrel (TIB), the Tracker Outer Barrel (TOB), the Tracker Inner Disc (TID), and the Tracker Endcap (TEC). The TOB and the TIB are in the central pseudorapidity region of the tracker. The TIDs are forming the endcap tracker. The strips are placed parallel to the beam axis in the barrel region and perpendicular to the beam axis in the end cap region in order to have an accurate measurement of the $r - \phi$ coordinates. The resolution in $r - \phi$ coordinates varies from 23 μm to 35 μm.

3.3.5. Electromagnetic Calorimeter

A hermetic homogeneous electromagnetic calorimeter surrounds the inner tracking system. The ECAL consist of the ECAL barrel (EB), within which 61200 lead tungstate ($PbWO_4$) scintillating crystals are mounted, and an ECAL endcap (EE), which consists on each side of 7324 crystals. The barrel region covers a pseudorapidity range of $|\eta| < 1.479$ while the two endcaps extend the pseudorapidity coverage to $|\eta| < 3.0$. In front of the each ECAL endcap, a preshower detector is installed in order to reject the $\pi^0 \to \gamma\gamma$ decays in a pseudorapidity range of $1.65 < |\eta| < 2.6$. Figure 3.8. shows the longitudinal view of one-quarter of the ECAL.

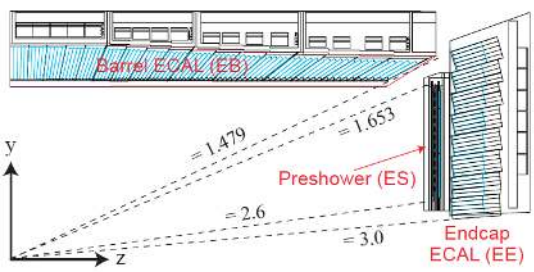

Figure 3.8. Schematic overview of one ECAL quarter with its subsystems. Dashed lines indicate the geometric acceptance and the blue color refers to the $PbWO_4$ crystals.

The ECAL is a homogeneous calorimeter which is built to measure the energy deposition of electromagnetically interacting particles. When these particles are stopped in the $PbWO_4$ crystals, a shower of particles is produced and the characteristic scintillation light emitted. The scintillation light is read out by a pair of avalanche photodiodes (APDs) in the barrel region and by Vacuum Photo Triodes (VPTs) in the endcaps. By measuring the scintillation light, the energy and the position of the primary particles are determined. The reason $PbWO_4$ crystal was chosen for ECAL is their radiation resistance and fast response time (80% of the light is emitted within 25 ns). The position resolution is optimised by requiring the small transverse size of the electromagnetic shower. The transverse profile of electromagnetic showers is expressed by the Moiler radius. The Moliere radius of the led tungstate crystals is 2.2 cm^2 and combined with a barrel crystal front face of 2.2 x 2.2 cm ensures that the core of the shower will be included in a 2x2 crystal area.

3.3.6. Hadronic Calorimeter

The Hadronic Calorimeter (HCAL) is placed between the ECAL and the CMS solenoid magnet. It is designed to measure the energy deposition and position of hadrons, particles made of quarks and gluons, as well as to determine the energy imbalance of each event which is caused by neutrinos or exotic particles. Neutral weakly interacting particles, like neutrinos, escape from detectors without producing any response in the detector elements. The presence of such particles is inferred from the imbalance of total momentum.The vector momentum imbalance in the plane perpendicular to the beam direction is known as missing transverse momentum E_T, and its magnitude is called missing transverse energy. It is an important variable to search for newly interacting, long-lived particles, including supersymmetry with the prediction of large E_T events. The colliding particles on poorly instrumented regions of the detector, cosmic-ray particles as well as the beam halo particles cause the artificial E_T. Therefore the reconstruction of E_T plays a crucial role in particle momentum mismeasurements, detector malfunctions, particle misidentification.

An overview of the CMS HCAL detector components is illustrated in Figure

3.9. The HCAL is composed of four distinct subsystems: the barrel (HB), endcap

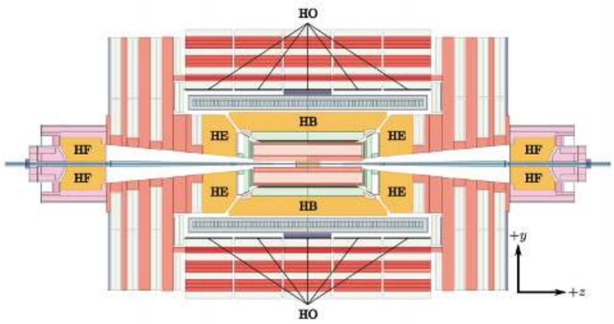

Figure 3.9. Schematic view of the CMS detector with HCAL components labeled in y-z projection

(HE), forward (HF), and outer calorimeters (HO). HB and HE are mounted hermetically and placed inside the cryostat of the CMS superconducting solenoid. HB covers a pseudorapidity range of up to $|\eta| < 1.4$, while HE extends the range to $1.3 < |\eta| < 3.0$. The HB is constructed in two half barrel sections HB+ and HB-, which consist of 36 identical azimuthal wedges aligned parallel to the beam axis. The brass absorber plates are used to construct the wedges that are segmented into four ϕ -sectors. The active medium is made of plastic scintillator trays split into 16 η-sectors and placed between the absorber plates. Within each tile, tiny optical wavelength shifting fibres (WLS) collect scintillating light and transmit the optical signal to the readout electronics. These optical signals are digitised by photosensors called Hybrid Photodiodes (HPD) and afterwards sent to the data acquisition system for event reconstruction and triggering. The endcaps are attached to the muon endcap yoke and cover the HCAL barrel part. It has a similar approach as the barrel calorimeter, consisting of scintillator layers which are interleaved with brass absorber layers The HF are symmetrically positioned at each side of the CMS endcap at a distance of 11.2 m from the interaction point. They cover the forward pseudorapidity region $2.8 < |\eta| < 5.2$

. Due to being very close to the beam pipe, the HF detectors are exposed to a very high particle flux. Thus a different detection system is used. The HF is a Cherenkov light detector made of scintillating quartz fibres, which act as the active medium, and steel absorbers. When the charged particles pass through the detector, they radiate Cherenkov light which gets transmitted to the photodetector behind the absorber.

The HF is designed for two main reasons: one is to improve the measurement of the missing transverse energy, and the other is to identify and reconstruct objects which do not interact with other detectors, such as very forward jets. The HO is located between the magnet and the muon system and measures the possible energy leakage from the HB. It covers the region of $0.4 < |\eta| < 1.26$ and consists of two layers of scintillator tiles located on each side of the barrel return yoke (YB). HO has the same principle as HB and HE for production, transmission, and readout of the light signal. The brass material has been chosen for the absorber of the barrel calorimeter due to the fact that it is a non-magnetic material and has a maximum number of interaction lengths for the hadronic showers. The HB is around 89 cm deep and the total absorber thickness at $90°$ is 5.82 nuclear interaction lengths (λ). At the edge of the barrel, the interaction length is 10.6 as the polar angle as 1/sin θ.

The total depth of the end-cap region is ten interaction lengths which include the electromagnetic calorimeter in front of it. The HF acts as an absorber with total depth 165 cm or $\approx$ 10 interaction lengths In consequence of using the outer calorimeter as an additional absorber in front of another 19.5 cm thick iron, the total depth is 11.8 interaction lengths.

3.3.7. The Muon System

The CMS muon system propose to distinguish muons from hadrons as performing a fast muon multiplicity count which allows to detect interesting events over very high backgrounds at the full LHC luminosity, such as the SM Higgs boson decaying into ZZ or ZZ^{*} and then further into four muons, the decay of new gauge bosons such as $Z' \rightarrow \mu^{+}\mu^{-}$ with $p_T > 1$ TeV, and the measurement of b hadron decays into J/ψ mesons, such as $B^{\pm}\rightarrow J/\psi K^{\pm}$ and $B_s^0 \rightarrow J/\psi\phi$.

Muons have a long lifetime of 2.2 μs in their rest frame, which allows them to survive up to the outer layers of the detector and a large rest-mass of 105.7 MeV/c^2, enabling them to penetrate the detector material. Furthermore, muons are not strongly interacting and can cross the full detector and reach the outside of the solenoid without losing much energy. For that matter, muon chambers are located on the outside of the experiment. The muon system is dedicated to the muon identification, momentum measurement and muon triggering. The system consists of three types of gaseous particle detectors, the Drift Tubes (DT), the Cathode Strip Chambers (CSC) (CMS Collaboration, 1997), and the Resistive Plate Chambers (RPC) (CMS Collaboration, 2013) which are interleaved with the iron return yoke as shown in Figure 3.10..

The muon system is divided into a cylindrical barrel and two planar endcap regions. The cylindrical barrel part consists of is 250 DTs in four stations, located inside the magnet yoke. It covers a pseudorapidity range of $|\eta| < 1.2$, where the background levels and muon rates are low and the magnetic field is uniform. Each DT chamber is mounted between two RPCs in the first two stations (MB1 and MB2), whilst in the last two stations (MB3 and MB4), each DT has one RPC fixed on the innermost part of the stations. The drift tube chambers are operated with a Ar/CO_2 (85%,15%) gas mixture.

The DT system is made of 12 layers, organized in three groups of four. Each

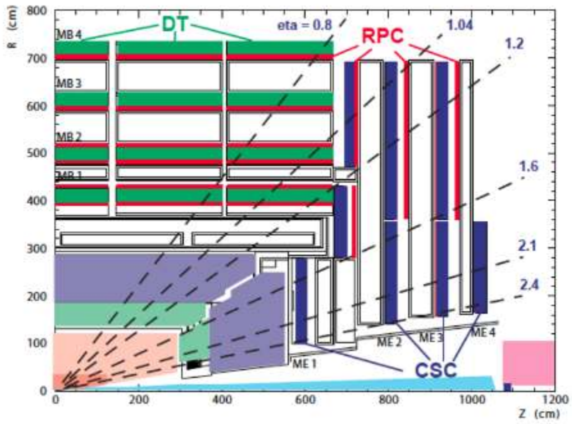

Figure 3.10. An overview of one quarter of the muon system. The barrel wheels (in green) host four DTs, four CSCs (in blue) in the endcap, and RPCs.

three Super-Layers (SL) contain four layers of drift tubes. The two outer SLs have wires parallel to the beam line which measure the tracking coordinate in the $r-\phi$ bending plane. The middle group, where the wires are perpendicular to the beam, measure the tracking coordinate in the z-direction. When a high p_T muon crosses up to six RPCs and four DT chambers, a muon track candidates can be built with measuring up to 44 produced points in the DT system.

The muon endcap (ME) system consists of 473 CSCs. The cathode strip chambers are placed in the two muon endcap (ME) regions providing a coverage of $0.9 < |\eta| < 2.4$, where the particle flux and background levels are high, and the magnetic field is large and non-uniform. The CSCs and RPCs are hosted in four stations in each endcap. The CSC is a trapezoidal multi wire proportional chamber which contains six gas gaps and operates with a nominal gas mixture of $Ar-CO_2-CF_4$ (40%,50%,10%). Each gas gap consists of a plane of cathode strips and anode wires running perpendicular to the strips.

When a charged particle traverses the plane of a chamber, a charge on the anode wire and an image charge on the plane of the cathode strips is generated. This leads to a gas ionization and a subsequent electron avalanche. Hence, each CSC measures the space coordinates (r, ϕ, z) in each of the six layers.The wires measure the beam crossing time of muons of 4.5 ns while the position measurement is made by determining the centre of gravity of the charge distribution produced on the cathode strips with a spatial resolution of about 200 μm and around ten mrad angular resolution.

The RPCs are gaseous parallel plate detectors which operate in avalanche mode with readout strips in between and contain a non-flammable gas mixture of $C_2H_2F_4$ or i-C_4H_10. The RPCs are mounted in both the barrel and endcap regions. They cover a pseudorapidity range of $|\eta| < 1.6$. There are six layers of RPCs embedded in the barrel muon system, where two layers are located in each of the first stations and one layer in each of the last two stations. The RPCs are attached to the DTs in the first two stations, where the RPCs provide the trigger algorithm for low p_T muons. In the endcap region, RPCs are located in each of the first three stations and positioned parallel to the CSCs in order to reduce background by using coincidence triggers between the stations, as well as improve the time resolution and to achieve a good p_T resolution. RPCs has a good time resolution of 3 ns with a precise assignment of a muon track to the correct bunch crossing while the space resolution is of the order of 1 cm.

3.3.8. The CMS Trigger

Besides the detection and energy measurement of particles, another challenge is the processing and filtering of the large volume of data coming from the particle detectors At the LHC design luminosity of $10^{34} cm^{-2} s^{-1}$, bunches of protons collide at a rate of 40 MHz, which leads to 10^9 interactions per second. Since it is technically impossible to store such amount of data, pre-selection needs to be applied to select as many of the interesting physics processes as possible and maximise their rate. Hence, two staged filter mechanisms are applied in the trigger system, which is a hardware-based Level 1 (L1) trigger and software based High-Level Trigger (HLT).

3.3.8.1. Level 1 Trigger System

The L1 trigger is designed to reduce the initial 40 MHz input to about 100 kHz within a period of 3.2 μs. The L1 trigger system has local, regional and global components which are operating in sequential order. The Local Trigger called Trigger Primitive Generators (TPG) is based on high energy deposits in the calorimeter system, and high momentum charged tracks in the muon system. Regional Triggers combine the information coming from HCAL and ECAL detectors in order to determine electron/photon candidates. The Global Calorimeter Trigger (GCT) and Global Muon Trigger (GMT) identify jets, the total transverse energy, the missing transverse energy, highest rank isolated and nonisolated objects and transfer them to the Global Trigger (GT). The data flow of the L1 system is shown in Figure 3.11.

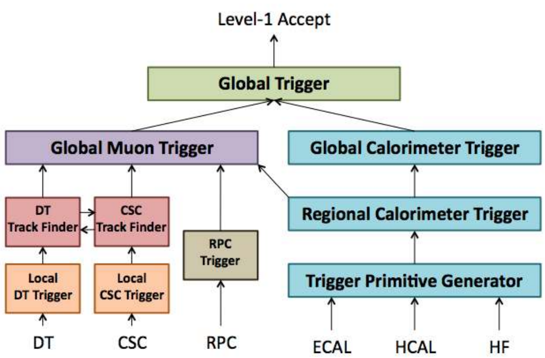

Figure 3.11. Architecture of the CMS L1 Trigger

All three subsystems (DTs, CSCs and RPCs) take part in the muon trigger system. The barrel DT chambers provide track segments in the - projection and hit patterns in the -projection, The endcap CSCs deliver track segments in three dimensions. The CSC and DT track finders calculate the transverse momentum, position, and quality of a track segment. Moreover, RPC trigger chambers provide an estimation of the p_T value which is extracted from regional hit patterns and send them to the GMT. The GMT receives p_T, charge, position and quality of pattern matching information for every muon candidate from DTs, CSCs, barrel and endcap RPCs. The GT collects all the information of trigger objects delivered by the GCT and GMT to accept or reject an event based on simple algorithmic criteria such as the object multiplicities exceeding certain values. If the collision event is considered interesting by the GT, it distributes a Level-1 Accept (L1A) decision to the individual sub-detectors in order to begin the Data Acquisition (DAQ) read-out of the event.

3.3.8.2. High Level Trigger System

The full detector information for an event ($\sim$1.5 MB) which is accepted by the L1 trigger system read out by the CMS DAQ system and transferred to the event filter farm as the HLT input. The HLT is purely based on software algorithms running on a large cluster of computers which is called the Event Filter farm (EVF). The L1 output of 100 kHz is reduced to 1 kHz by HLT farm for offline processing and storing.

In order to efficiently process events, the HLT focuses on the reconstruction of the minimum amount of detector information needed to apply a set of selection criteria to reject background events and keep the desired physics events for further processing. The reconstruction and selection in the HLT are performed in two level. Level 2 is the first selection step in the HLT process. It uses only information from the calorimeter and muon detectors. In contrast, Level 3 uses of the full information from all tracking detectors. The HLT is configured to trigger events according to a set of trigger menu. Each HLT menu consists of a list of trigger paths which have a specific trigger object selection with kinematic cuts. For example, studies of bottomonium (b$\bar{b}$) states such as B hadrons decaying into a J/ψ ($J/\psi \rightarrow \mu^+\mu^-$) , a set of unbiased trigger with loose muon selection criteria is provided. When an event is flagged one of the HLT trigger menus, the reconstructed physics objects are written along with the raw data file in ROOT format (Antcheva, 2009) and then the files can be used for offline physics analysis.

4. ANALYSIS OF THE DECAY $B_s^0 \to J/\psi\phi$

This analysis is present the measurement of the differential cross sections and the nuclear modification factor for exclusive final state of $B_s^0 \to J/\psi\phi$ in pp and PbPb collisions at the center-of-mass energy $\sqrt{s}$ = 5.02 TeV and in the rapidity range $|y| < 2.4$ with the CMS detector at CERN LHC. The production cross sections are measured in the p_T range between 7 and 50 GeV/c.

4.1. Data Samples

The data samples used in this analysis were recorded by the CMS detector in pp and PbPb collisions at $\sqrt{s_{NN}}$ = 5.02 TeV during 2015. The pp dataset corresponds to an integrated luminosity of 28 pb^{-1} and PbPb datasets corresponds to 351 mb^{-1} (Lujan, 2018). In order to perform this analysis, the dimuon primary datasets were used for both pp and PbPb collisions. The list of datasets are shown in Appendix G

To assure the data quality the JSON (JavaScript Object Notation) files are applied for each data samples. The used JSON files is defined for both pp and PbPb in Appendix H.

The events in this analysis are selected with a trigger containing two independent muon candidates. There is no selection applied to momentum or pseudo-rapidity. Several offline selections are implemented for each event due to derive pure collision events. At least one reconstructed primary vertex is needed for both pp and PbPb events. The primary vertex is constituted two or more associated tracks. In addition, it is necessary to have a distance from the nominal interaction region of less than 15 cm along to the beam axis and less than 0.15 in the transverse plane. In terms of filters which are used in this analysis, a scraping filter is applied for pp while a cluster compatibility filter is used for PbPb analysis. The detailed information of these filters can be found in Section 2.2 of (Dogra et al., 2017).

Besides, an additional selection of hadronic collisions is performed. It is required that a coincidence of at least 3 HF calorimeter towers from the HF detectors on from sides of the interaction point with more than 3 GeV of total energy.

4.2. Simulated (MC) Samples

In order to validate the analysis technique, the official pp and PbPb samples were generated, simulated, and reconstructed by using official CMS simulation productions. The simulated B_s^0 samples allow to determine the signal reconstruction efficiencies, evaluate systematic uncertainties and estimate the background components in the signal mass window. PYTHIA8 Tune CUETPM8 (**pythia**; Field, 2010) generator was used to generate the signal (B_s^0) at 5.02 TeV, by implemented inclusive (all quark/antiquark besides gluon initiated) QCD process, such as $qq \to qq$ and $gg \to qq$. At the EVTGEN stage, only signal events were stored with at least one B_s^0 which is forced to decay exclusively $J/\psi\phi$, with requirements on their total momentum $p_T > 5.0 GeV/c$, and pseudorapidity $|\eta| < 2.4$. Moreover J/ψ forced to decay into dimuon channel to have a pair of oppositely charged muons and ϕ meson forced to decay in the two kaons. The final state radiation (FSR) were generated with EVTGEN through PHOTOS package (Barberio and Was, 1991). In terms of the PbPb samples, for prompt and non-prompt J/ψ MC, the selected B hadrons PYTHIA8 events were embedded into a PbPb background simulated with HYDJET (version 1.8, tune"Drum") (Lokhtin and Snigirev, 2006) and for B_s^0 signal MC, they were tuned "Cymbal5Ev8" (**Lokhtin:2005px**) event generator. About fifty thousand events in both signal and embedded samples are generated in 5 p_T bin interval with boundaries of [0,5,15,30,50 GeV/c]. The events are reconstructed in the CMS software with release CMSSW_7_5_8_patch3 and tagged as 75X_mcRun2_HeavyIon_v13 for PbPb, and 75X_mcRun2_asymptotic_ppAt5TeV_v3 for the pp samples. A significant amount of events have been generated by forcing one of the b-quarks to hadronise as a B_s^0 or $\overline{B}_s^0$ meson and decay into $B_s^0 \to J/\psi\phi$ where $\phi \to K^+K^-$. In order to determine the peaking background appearing in the $\mu\mu KK$ mass spectrum, the inclusive non-prompt J/ψ samples which contain several different B mesons decaying into J/ψ channels, were also produced. The produced signal, prompt and non-prompt MC samples datasets names for pp and PbPb are listed in Appendix I1..

4.3. MC Reweighing

The aim of the reweighing is to alter the obtained distribution of the events from MC to describe the data distribution. It provides us to isolate the problems caused by generation or simulation. Noted that reweighing should not affect the normalisation of MC which is generated with a specific number of events plus accurate cross section. B_s^0 p_T spectrum obtained from MC samples are required to reweigh for both pp and PbPb collisions for matching the one calculated from FONLL. In the left panel of Figure 4.1. presents the B_s^0 p_T spectrum derived from MC simulations, in the middle panel shows the comparison of the results obtained from FONLL calculations at 5.02 TeV. The ratio between FONLL and the MC distributions represented in the right panel of the same figure. The weight function was derived by fitting with a 2nd order polynomial. Same calculations is done for PbPb MC simulations and it is shown in Figure 4.2..

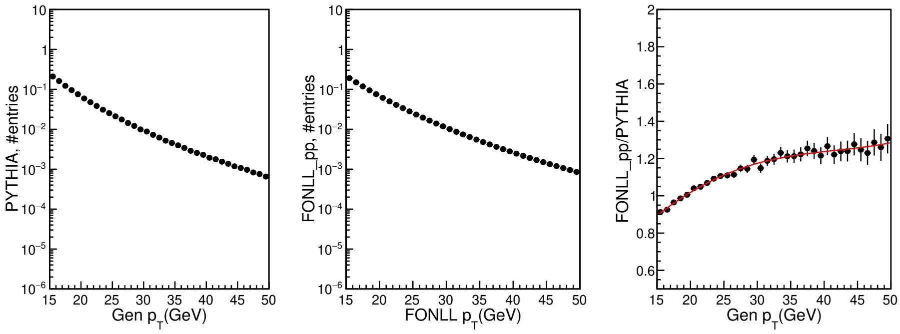

Figure 4.1. B_s^0 p_T spectrum in pp MC simulations (left panel) compared to the one calculated from FONLL (Fixed Order Next to Leading Logarithms) at 5.02 TeV (middle panel). The ratio between MC and FONLL distributions with fitting a 2nd order polynomial function (right panel).

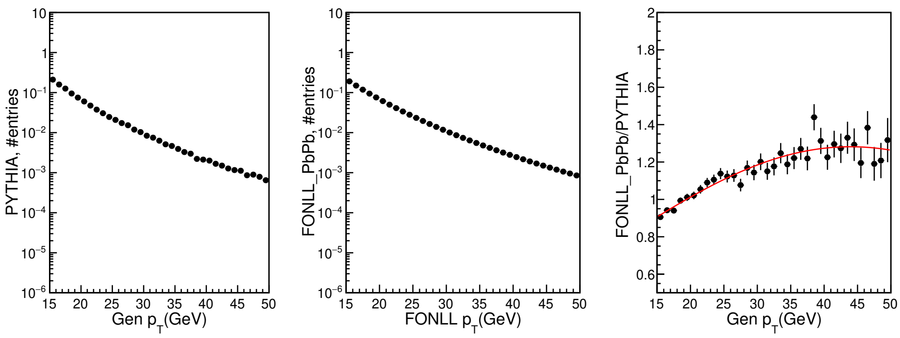

Figure 4.2. B_s^0 p_T spectrum derived in PbPb MC simulations (left panel) compared to the one obtained in FONLL calculations at 5.02 TeV (middle panel). Ratio between the MC and FONLL distributions, fitted with a 2nd order polynomial function (right).

Additionally, PbPb MC simulations are reweighed to have a good agreement with the centrality distribution in data. The centrality distribution of the MC simulations and data is compared in the left panel of the Figure 4.3.. On the x-axis, each unit (HiBin) corresponds to 0.5% centrality. The ratio between the centrality distribution from MC and data is represented on the right panel of the figure.

The weighting function is derived by fitting the ratio of the Data and MC dis-

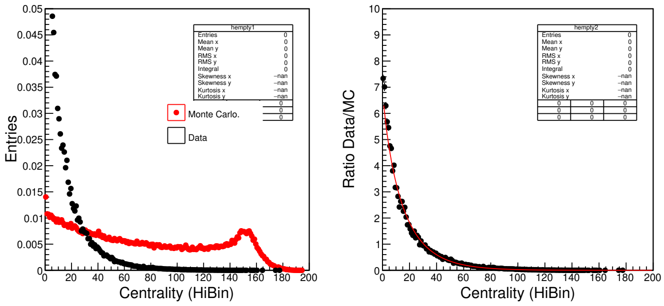

Figure 4.3. (Left) Centrality distribution of MC (red) and data (black) in PbPb collisions in the centrality interval 0-100%. (Right) Ratio between the centrality distribution of data and MC fitted with a exponential function.

tributions with using the following function:

$$p_1 e^{p_2(centrality - p_3))^{p_4}} \tag{4.1}$$

where p_1, p_2, p_3, p_4 are the fitting parameters. Besides, having the p_T shape and reweigh the centrality as above, the Minimum Bias (MB) samples are embedded for the PbPb signal MC samples (with Cymbal5Ev8 tune) with an offset in the primary vertex z position (PVz). Detailed information for re-weighting procedure has been conducted by the HighPt group and presented in:`https://twiki.cern.ch/twiki/pub/CMS/HiHighPt2017/170426_ZVertexWeightForMC.pdf`.

The signal B_s^0 for PbPb MC samples are re-weighted with the same procedure and the results are presented in Fig. 4.4.. On the left panel, after the re-weighting, the MCPVz distribution is shown with red markers while PbPb data is indicated in black. The right plot shows the ratio between MC and data. According to the ratio plot, a good agreement is observed between MC and data. However, the absolute value of V position is not finely tuned in this analysis. Because the B_s^0 reconstruction relies on the relative distance between PV and B_s^0 reconstructed vertex (presented in the following section). Hence, this effect is estimated by removing the re-weighting and calculated difference is only 1.3%. The results are derived with using MC samples

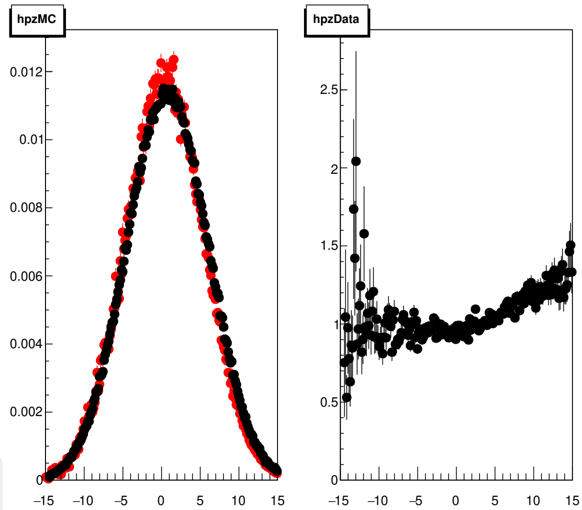

Figure 4.4. B_s^0 primary vertex z position (PVz) spectrum in PbPb MC simulations after applying the official re-weighting procedure (red marker) compared with PbPb data (black marker) at 5.02 TeV (left panel). Ratio between the MC and data distributions (right panel).

after applying the official re-weighting procedure with respect to the p_T shape of pp and PbPb, PVz of PbPb and centrality for PbPb.

4.4. B_s^0 meson Reconstruction and Base Selections

4.4.1. B_s^0 meson reconstruction

The goal of this section is to determine a set of criteria to minimise the background and maximising B_s^0 signal events as much as possible. The identification and the optimization of the selection criteria is studied using MC samples. Regarding to possible systematic conflict with data and MC samples, the event selection has to be consistent. The selection of B meson candidates is based on the determination of $J/\psi \to \mu^+\mu^-$ and $\phi(1020) \to K^+K^-$ decays. B_s^0 generation and the decay chain is represented in Figure 4.5.

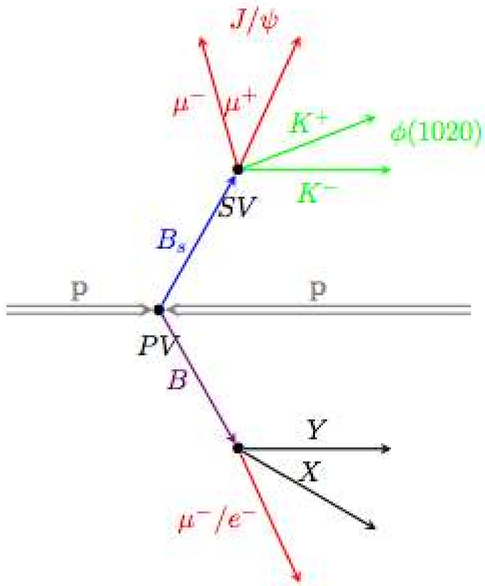

Figure 4.5. The schematic view of B_s^0 generation decaying in the channel $B_s^0 \to J/\psi\phi \to \mu^+\mu^-K^+K^-$

The schematic diagram of the workflow in Figure 4.6. explains the selection criteria and steps in order. The selections start from muons and tracks and follow with

B_s^0 meson candidates selections. All muons and tracks have to pass the several quality selection criteria which are defined in Section 4.4.2. and in Section 4.4.3..

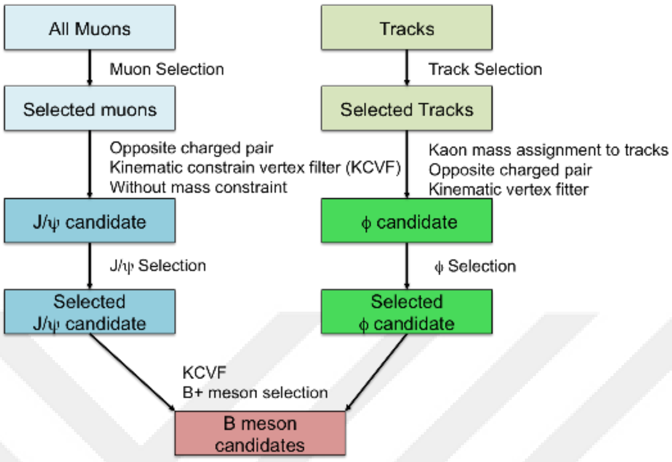

Figure 4.6. Schematic diagram of the B meson reconstruction work flow

The J/ψ candidates are reconstructed with vertexing oppositely charged muon pairs, using kinematic constrained vertex fitter. ϕ meson candidates are reconstructed using the vertexing procedure in the same way as J/ψ candidates. Lastly, a kinematic fit to the J/ψ-K^+K^- decay is applied with forcing the di-muon pair mass to be equal to the nominal J/ψ mass depend on PDG. (P. D. Group, 2014).

4.4.2. Muon and J/ψ selection

The muon candidates are selected in accordance with the hybrid-soft muon selection which is evolved for the muon analysis on 2015 with 5.02 TeV data (Heavy Ion Group, 2016). It is based on the soft-muon ID (which is developed in the BPH group) with two modifications; first, the purity selection is removed and second, the muon is required to be also global. The hybrid-soft muon selection contains the following cuts,

- it must be GlobalMuon and TrackerMuon;
- GoodMuon>0;
- transverse impact parameter $D_{xy} < 0.3$;
- longitudional impact parameter $D_z < 20$;
- nPixWMea > 0 and nTrkWMea > 5

where nPixWMea and nTrkWMea are the number of pixel layers and strips with eligible hits, crossed by single muon track. Furthermore, muons are requested to fulfill kinematic acceptance selections which are shown in Table 4.1.

Table 4.1. Muon Acceptance

P_T	Eta (η)
$p_T^\mu > 3.5$ GeV/c	$\lvert\eta^\mu\rvert < 1.2$
$p_T^\mu > (5.77 - 1.8 \times \lvert\eta^\mu\rvert)$ GeV/c	$1.2 \leq \lvert\eta^\mu\rvert < 2.1$
$p_T^\mu > 1.8$ GeV/c	$2.1 \leq \lvert\eta^\mu\rvert < 2.4$

This single muon selection is determined to assure a reasonable reconstruction above $\approx 10\%$ and trigger efficiency for the selected muons (CMS Heavy Ion Group, 2016b). In addition to that quality selections, the following criteria are performed for a muon pair candidates:

- The two muons must have opposite charges;
- Di-muon invariant mass has to be within 0.15 GeV mass window width from Particle Data Group (PDG) J/ψ mass.
- probability of the two muon tracks which is derived from the same decay vertex must greater than 1 %.

4.4.3. Track Selection

The $\phi \to KK$ decay candidates are reconstructed from pairs of oppositely charged tracks. The silicon tracker detectors require having at least four hits pattern from each track. However, CMS experiment does not have a qualified track identification system to separate pions from kaons. Therefore all measured tracks have to be considered as possible kaon candidates. The invariant mass of a track pair are required to be consistent with ϕ meson is known mass (Mϕ = 1019.455 ± 0.020 MeV/c^2, Nakamura et al. (2010)). The tracks were selected corresponding to the following criteria:

- GeneralTracks passing High Purity (HP) selection;
- $\eta < 2.4$ and $p_T > 0.5$ GeV/c for pp and $p_T > 0.8$ GeV/c for PbPb; these selected variables are used as a preselection for the further cut optimization.

HP Tracks: it is a subset of tracks derived with tight selections and low fake rate. The fake rate is the fraction of reconstructed tracks which are not associated with charged particles. The high purity tracks selection is based on the number of layers have at least one hit and the maximum number of tracker layers with no assigned hits. In addition, the track fit yielded with good $\chi^2/Ndof$ is also imposed for the HP selection. The detailed information of the high purity selection can be found in (Chartchyan and other, 2014).

4.4.4. B_s^0 Meson Selection

Very loose selection cuts are applied to the B_s^0 and ϕ meson invariant mass window before the vertex fitting. These lose selections provide to increase the processing speed of vertex fitting by extracting unnecessary candidates. The J/ψ candidate is combined with ϕ candidate to form B_s^0 meson candidate. The daughter particles, two muons and two kaons, are required to be originated from a common vertex. In order to have a precise reconstruction of the B_s^0 decay vertex, a kinematic vertex fit is used where the dimuon invariant mass constrains to the nominal J/ψ mass. The ϕ meson invariant mass width in signal MC is of order 0.01 GeV/c^2(see Fig. 4.7.). The observed B_s^0 invariant mass differences are of order 0.2 GeV/c^2 before and after the vertex fitting.

- Track pair invariant mass be within 0.015 GeV/c^2 around the ϕ meson PDG mass (1.019455),
- B_s^0 candidate invariant mass between 4.5 to 6.5 GeV/c^2.

Consequently, these selections are loose enough in order not to affect the offline analysis. After passing the all analysis selections (which is discussed in the next section), the J/ψ and ϕ meson mass spectra for MC and data in pp analysis is shown In Figure 4.7. For PbPb MC and data, J/ψ and ϕ meson mass spectra is represented in Figure 4.8.

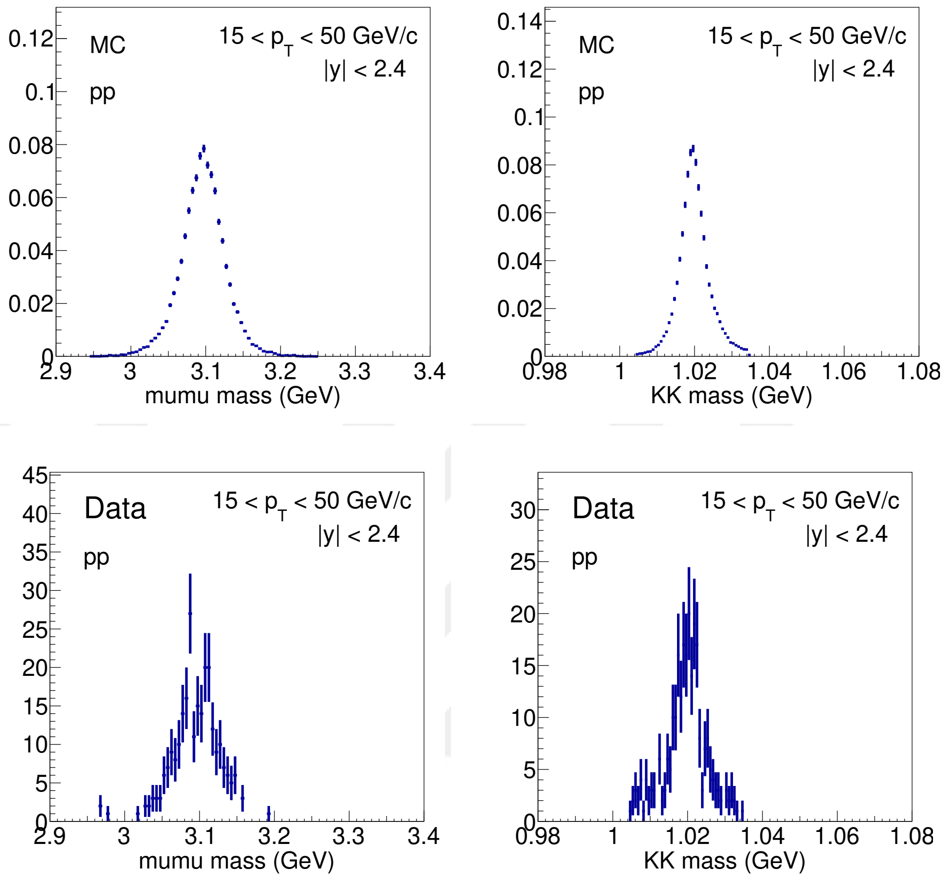

Figure 4.7. The left top refers to J/ψ mass spectra from pp MC and bottom left for pp data while right plots show the ϕ meson mass spectra from top to low pp, MC and data, after all the analysis selections.

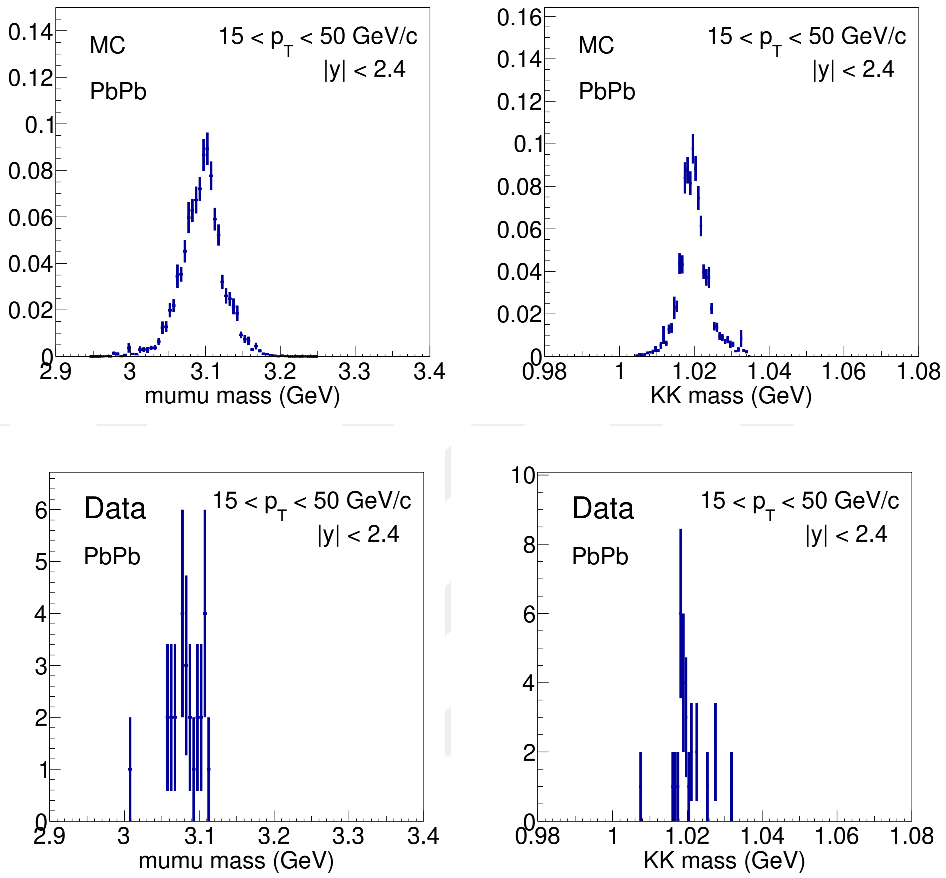

Figure 4.8. The J/ψ (left) and ϕ (right) meson mass spectra (after the all analysis selections) for MC (top) and data (low) in PbPb analysis

4.4.5. Trigger Selection

A two-stage trigger system provides the events selection in this analysis as of hardware (L1) and software (HLT) based and uses the muon, calorimeter, and tracker detectors. A hardware-based stage selects the events contains a single muon or a pair of muon candidates with high transverse momentum. The software trigger confirms the hardware trigger decision and collects the events requiring the presence of two independent muon candidates at the HLT without applying explicit momentum and pseudorapidity threshold. The muon trigger at L1 uses three muon system, DT, CSC and RPC and contains local, regional, and global trigger components. Barrel DTs provide the local trigger information with track segments in the ϕ projection and with hit patterns in the η projection. DT and CSC track finders constitute the regional muon trigger. They provide to join the segments in order to complete tracks and assign physical parameters to them. The RPCs have sufficient precision for triggering purposes and deliver their own track candidates based on regional hit patterns. The information from the DT, CSC and RPC trigger is processed by the Global Muon Trigger (GMT). Each system provides the information independently which contains muon position, momentum and quality. Therefore the GMT can achieve optimum control of efficiency and rate. The trigger efficiency is related to the transverse momentum of the B_s^0 candidates and defined as:

$$\varepsilon(p_T^{B_s^0}) = \frac{N_{trg}(p_T^{B_s^0})}{N_{gen}(p_T^{B_s^0})} \tag{4.2}$$

where N_{trg} is referred to the number of events passing the trigger in the given p_T bin, and N_{gen} is the number of events generated in the same p_T bin range. The selected triggers need to provide the highest signal efficiency and the highest possible background suppression. The best four trigger candidates then sent to HLT for further processing. HLT trigger system performs in two main steps as of level-2 (L2) and level-3 (L3).

L2 builds tracks from patterns of DT and CSC segments in the muon system, and L3 reconstruction builds a seed for the tracker reconstruction starting from the L2 information. Muon tracks at L3 are reconstructed using data from the silicon tracker. The reconstruction is performed using only pixel and strip hits. The final selection relies on the transverse momentum measurement of the muon candidates at L3. The data used in this analysis were collected with HLT_DoubleMu0 trigger path which is a double muon pass-through trigger, with at least two muons identified without any p_T requirement and the dimuon invariant mass interval between 2 and 4 GeV/c^2. The list of selected dimuon trigger paths with corresponding luminosities are presented in Table 4.2.

Table 4.2. List of datasets (both pp and PbPb) and HLT triggers with related integrated luminosities used in the $B_s^0 \to J/\psi\phi$ analysis.

Sample	Primary dataset	HLT Trigger	Luminosity
pp	/DoubleMu/Run2015E-PromptReco-v1/AOD	HLT_HIL1DoubleMu0_v1	$27.70pb^{-1}$
PbPb	HiOniaL1DoubleMu0/HIRun2015-PromptReco-v1/AOD	HLT_HIL1DoubleMu0_v1	$135.64mb^{-1}$
PbPb	HiOniaDoubleMu0B/HIRun2015-PromptReco-v1/AOD	HLT_HIL1DoubleMu0_part1_v1	$71.71mb^{-1}$
PbPb	HiOniaDoubleMu0C/HIRun2015-PromptReco-v1/AOD	HLT_HIL1DoubleMu0_part2_v1	$71.67mb^{-1}$
PbPb	HiOniaDoubleMu0D/HIRun2015-PromptReco-v1/AOD	HLT_HIL1DoubleMu0_part3_v1	$71.67mb^{-1}$
PbPb	Combined All		$350.68mb^{-1}$

During the data taking period in 2015, the pp HLT trigger paths were unprescaled, whereas PbPb HLT trigger paths were prescaled with different values in different runs. The detailed information of the complete dimuon dataset and HLT triggers is presented in (CMS Heavy Ion Group, 2016a). Due to the limited bandwidth of the trigger system only a fraction of the muon candidates are kept which is called pre-scaling.

4.5. B_s^0 meson Selection Optimization

B_s^0 resonance in the pp data is observable by applying the selection criteria explained in the previous section while the situation is dramatically different for PbPb data due to having the significant number of combinatorial background. Therefore, a multivariate analysis (MVA) was performed to separate the B_s^0 signal from background and reconstruct an observable resonance in the B_s^0 mass spectrum for PbPb collision data. Besides, even for pp analysis, it will help to decrease the statistical uncertainty associated with the fitting performance in the mass spectrum. The fitting performance is related to both signal and background determined in the mass spectrum. Thus, MVA analysis can provide to find proper selection criteria that are optimised for this purpose. Consequently, MVA analysis is conducted for both pp and PbPb collision data with applying several variables selections on related tracks and B_s^0 decay chain to decrease the combinatorial background which is caused by random combinations of tracks and muons.

4.5.1. Cut Optimization

The optimisation procedure is based on the maximising the statistical significance of signals with reasonable high signal efficiencies over the background. For the cut optimisation, we conducted the TMVA method (Toolkit for Multivariate Data Analysis with ROOT) (Hoecker et al., 2016) which provides for determining the optimum cut values for some variables to reach the highest signal efficiency by reducing the background. There is a different type of techniques in TMVA method consists of different classifiers. In this analysis, the BDT (Boosted Decision Trees) approach was chosen which shows the highest signal efficiency over background by comparing the ROC (Receiver Operating Characteristic) curve (background rejection versus signal efficiency) with the other classifiers including MLP (Multilayer Perceptron) from the

Artificial neural network (ANN). The signal is described as reconstructed candidates matched with the generated signal in MC samples. To define the background, the reconstructed candidates from outside of the signal region (in the sideband) (0.2GeV/c^2 $< |M_{B_s} - M_{B_s}^{PDG}| <$ 0.3 Ge V/c^2) of data sample are used.

In our case twelve variables are considered for BDT method:

- track p_T: the transverse momentum of the K^+ and K^- track
- |track η|: the pseudorapidity of the K^+ and K^- track
- normalized track Dxy: the normalized transverse distance between the K^+ and K^- track to primary vertex
- normalized SV (Secondary Vertex) PV (Primary Vertex) distance: the distance of primary and B_s^0 vertex normalized by its uncertainty
- α_B angle: the angle between B_s^0 meson displacement and B_s^0 meson momentum
- track pair invariant mass: the absolute difference between the invariant mass of the track pair (which form ϕ meson candidate) and PDG mass of a ϕ meson
- 2D normalised SV and PV distance: the distance between primary and B_s^0 vertex normalised by its uncertainty in the transverse direction
- cosine θ_B angle: the cosine of the angle between B_s^0 meson displacement and B_s^0 meson momentum in the transverse direction
- vertex fitting probability: the χ^2 value of the vertex fitting

The comparison of the distribution of the variables used for BDT training between data and MC for pp analysis is presented in Section 4.6.1.

The TMVA optimisation procedure is fulfilled by using two B_s^0 p$_T$ binning of 7 to 15 GeV/c and 15 to 50 GeV/c for both pp and PbPb samples, separately and individually. The reason for using different p$_T$ binning is to distribute the statistic evenly in each bin. The independent optimisation is performed for the number of B_s^0

p_T bins times 2, pp and PbPb. In Appendix A, the correlation between the variables selected for MVA training for both pp and PbPb analysis are shown in Fig. A1. and Fig. A2., respectively.

The optimum cut values definition is based on the maximizing the significance using signal MC and the background expectation.

$$Significance = \frac{S}{\sqrt{S+B}} \quad (4.3)$$

Where S the number of signal and B is the number of the background in the signal region which is defined as $|M_{B_s} - M_{B_s}^{PDG}| < 0.08$ GeV/c^2, after applying optimum cut values. The signal optimal cut efficiency is calculated with the following equation.

$$Efficiency = \frac{S'}{S} \quad (4.4)$$

where,

- S = S' $\times$ (signal optimal cut efficiency), where S' is the number of signal in signal region before optimal cuts applied.
- $B = B'$ $\times$ (background optimal cut efficiency), where B' is the number of background in signal region before optimal cuts applied.

The number of the signal in the signal region before applying optimal cuts (S'), is determined by FONLL calculation multiplied by pre-filters efficiency and acceptance using MC samples. Outside of the signal region, the number of the expected background B is evaluated by linear interpolation using the number of candidates in sideband.

In Appendix B, the distributions of the input variables used in each MVA training are represented in Figure B1. to Figure .B4.. The significance $\frac{S}{\sqrt{S+B}}$ as a function of BDT for p_T range 7 to 15 and 15-50 GeV/c is presented in the Figure B5. to Figure B8. for pp and PbPb collisions data, respectively. As a result, the final optimal selection values are summarized in Table.4.3. for both pp and PbPb collisions.

Table 4.3. Selection criteria in pp and PbPb analysis

p_T **(GeV/c)**	**7-15**	**15-50**
pp BDT	> 0.191055	0.208973
PbPb BDT	> 0.213755	0.254413

4.5.2. Check on prompt MC sample

The direct production of J/ψ mesons plays a vital role to determine the background at the trigger level. It can be formed as results of c$\bar{c}$ bind states emerging from the parton interactions and radiative decay of high energy excitation states. Because of the production and decay very close to the collision point these J/ψ mesons are known as prompt. We need to examine the determined BDT optimum cut value if it causes the artificially induced bias in the mass spectrum. Such as, it is resulting in reducing the candidates in the sideband region while increasing them in the signal region without the presence of a real signal. For this study, the prompt J/ψ MC samples are used due to fact that prompt J/ψ and random track pairs constitute most of the combinatorial background in the B_s^0 mass spectrum. The same kinematic criteria which applied to the signal and background simulations were implemented to this prompt J/ψ samples. The resulting mass spectra is checked by applying different BDT cut values. BDT values scan from the default cuts as in Table 4.3. through from minus 0.2 for 3 steps such as from 0.19,-0.01, -0.21, and -0.41,for both pp and PbPb collisions in p_T range 7-15 and 15-50 GeV$/c$. The resulting plots are represented in Appendix C from Figure C1. to Figure C4. Meanwhile, it is noted that the used

PbPb MC is merged with the various MC samples with different J/ψ p_T, but for pp, a single sample is used. The individual PbPb J/ψ p_T samples results also plotted and the results can be found in Appendix F. The base idea is to check the structure of the spectrum,and J/ψ p_T relevance is very little. However, this is checked by using the pp J/ψ which is produced the BDT discriminant value trained in PbPb data and the resulting plots are represented in Appendix C with Figure C5. and Figure C6.

As a consequences, the mass spectrum is smooth and continues as expected. There is no artificial peaking or dipping structure in the signal or side band region where the MVA only have information about candidates. In case of the MVA result had a bias or over fitting, then there will possibly be some unusual structure in the spectrum that consists of the only background. For example, a complex decision tree structure resulted in only selecting candidates with an invariant mass in the signal region and rejecting candidates in the side band region without considering whether it is a signal or not. Furthermore, if MVA has a bias, there will be a gap between the determination of the signal and side band region and should end up an unexpected structure for candidates in this gap region. Consequently, there is no obvious bias introduced by the BDT discriminant obtained from the cut optimization procedure.

4.6. MC-Data Comparison

4.6.1. Comparison of B candidate properties in between data and MC

The differences between data and MC distribution of the variables which are used for the B_s^0 signal selection can cause the biases in the detector efficiency corrections. Hence, the idea is to compare the distributions of the variables between data and MC samples. In order to derive the signal distribution, the B_s^0 yields are extracted in associated with the different selection variables by performing the standard selection criteria in the main results. For a meaningful comparison between data and the MC, the distributions are normalised to unity. The comparison distributions of various variables for pp collisions are presented in Appendix D with Figure D1., D2., and D3.. The same study could not be performed for PbPb collisions, in consequence of having very limited B_s^0 statistics. However, to compare the PbPb data and MC, the PbPb BDT value is generated by using pp MC and data samples. The resulting plot is also can be found in Appendix D with Figure D3.

In addition to the comparison between MC and data, the variables distributions are also compared between pp and PbPb MC samples which are represented in Appendix D from Figure D4. to Figure D9.

Consequently, the comparison of different B_s^0 meson variables between either MC and data or pp and PbPb MC samples indicate reasonably similar distributions with each other.

4.7. Extraction of Signal

The B_s^0 invariant mass distribution is measured in transverse momentum range between 7 and 50 GeV/c. The B_s^0 meson yields in each P_T interval are extracted by fitting procedure using the RooFit package. The extended unbinned maximum likelihood fit was considered for B_s^0 invariant mass spectrum. The fit functions used for this analysis contain the following components:

- *A double Gaussian with same mean but different widths*: In order to model the $B_s^0 \to J\psi\phi$ signal shape, a double Gaussian with same mean but different width function is used. This model was used instead of a single Gaussian or a Breit-Weigner function because it demonstrated a better signal shape in MC simulations.
- *A linear function (1st-order polynomial)*: To describe the combinatorial background a linear fit function is used. The combinatorial background is dominated by inclusive J/ψ production with tracks which are not originating from a B meson, but constitute an invariant mass in the B-meson mass range.

There is additional background based on misreconstructed b hadron decays which can generate peaking structures in the B-meson mass region in B_s^0 analysis. This study is done by using non prompt J/ψ MC samples. After applying optimal cuts , it indicates that the contribution of peaking background is negligible comparing to the B_s^0 signal. This is mainly resulting from the narrow natural width of the ϕ meson which eliminates the most of the fake track pair background with logical cut. The Non Prompt J/ψ peaking background is explained in 4.14.. The fit process for the signal and the background components can be defined as follows:

- Start with performing a double Gaussian fit function to the MC invariant mass distribution of B_s^0 signals.
- After deriving the fit function using the MC samples, the fit is applied to data mass spectra. The widths of the Gaussian signals is set to be equal to the one estimated in MC, together with the relative proportion of the two Gaussian. The free parameters of the fit to data are determined as the combinatorial back-

ground components and the mean of the signal Gaussian.

The invariant mass spectra derived from B_s^0 p_T 7 to and 15 to 50 Gevc P_T and $|y| < 2.4$ intervals in the pp and PbPb analyses are represented in Figure 4.9. and Figure 4.10. The invariant mass range determined between 5 to 6 GeV/c^2 for the fits. The error bar related to each data point is only for illustration purpose because an unbinned maximum likelihood fit for statics error is a different approach. In other words, the likelihood fit concept itself designate the statistical uncertainty. The represented errors correspond to Poisson error with Neyman construction (the frequentist confidence interval construction). This error calculation method is recommended by CMS Statistics Committee.

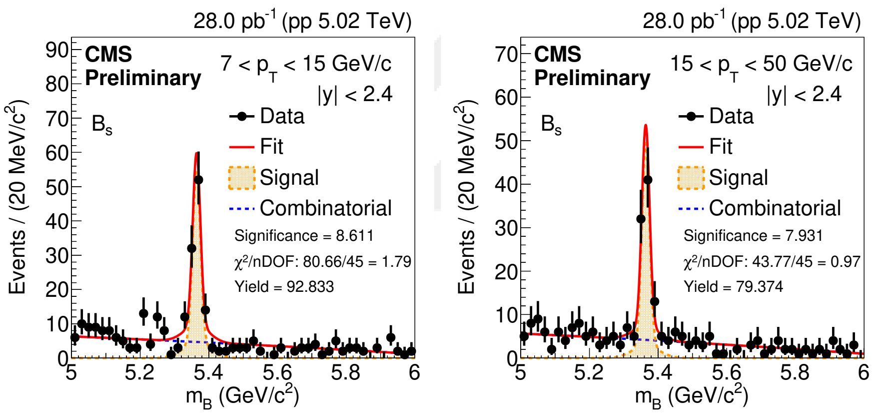

Figure 4.9. Invariant mass distribution and fit of B_s^0 candidates obtained in pp collisions in the p_T interval between 7 to 15 GeV/c and 15 to 50 GeV/c. The red line shows the complete fit function, and the orange dots indicate double Gaussian signal component and blue dash line refers the combinatorial background.

The available statistic in pp analysis can provide a finer differential p_T binning. The resulting mass spectra in the pp analysis, for 3 p_T intervals from 7 to 15, 15 to

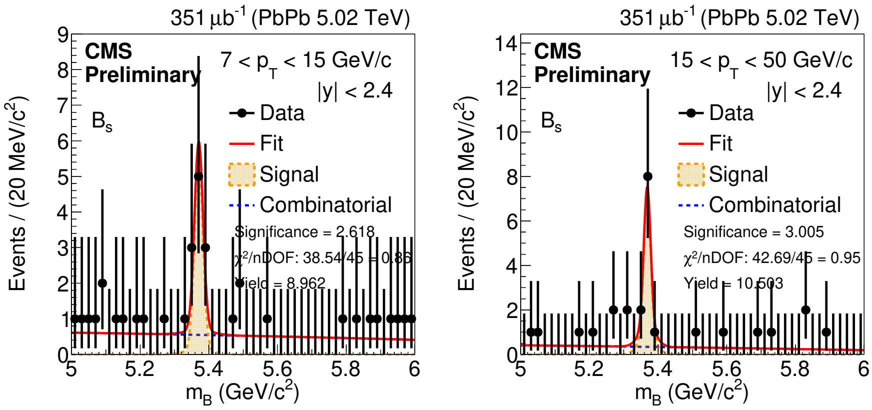

Figure 4.10. Invariant mass distribution and fit of B_s^0 candidates obtained in PbPb collisions in the p_T interval between 7 to 15 GeV/c and 15 to 50 GeV/c.

20, and 20 to 50 GeV/c are represented in Figure 4.11. The Table 4.4. summarize the resulting significance, normalized χ^2 and obtained yields for both pp and PbPb collisions and B_s^0 p_T bin intervals. The significance is determined as the $S/\sqrt{S+B}$ within a 0.05 GeV mass window around the signal mean. The χ^2 is considered as the Baker and Cousins definition (Baker and Cousins, 1984) that is the recommended method by the CMS Statistics Committee (Statistic Committee, 2018). While the fitting applied on the mass spectra was an unbinned fit, χ^2 was determined in a binned histogram. Thus the χ^2 performs as a goodness of fit test (not the FCN function that was being minimised in the fitting).

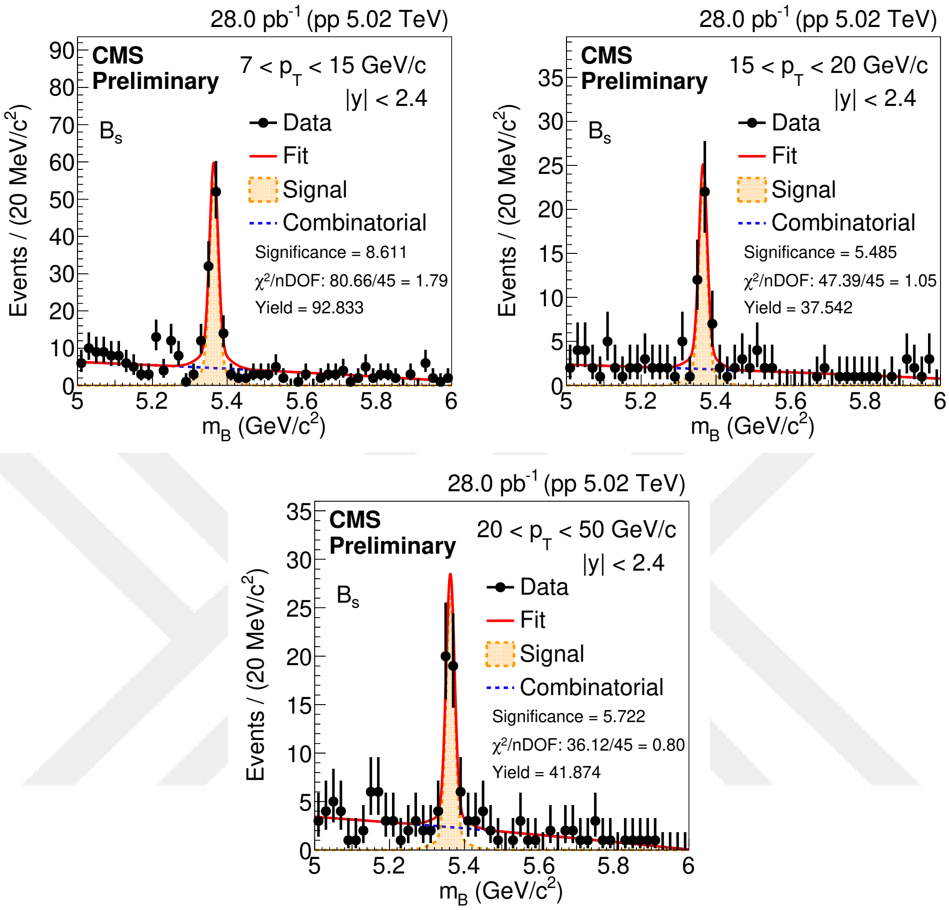

Figure 4.11. Invariant mass distribution of B_s^0 candidates obtained in 3 p_T intervals between 7 to 50 GeV/c in pp collisions .

Table 4.4. Summary table of Significance, χ^2 divided by degree of freedom after the fitting, and fitted yield for each B p_T bins for both pp and PbPb collisions.

	(7,15)	(15,50)	(15,20)	(20,50)
Significance				
pp	8.6	7.9	5.5	5.7
PbPb	2.6	3.0		
χ^2				
pp	1.8	0.97	1.1	0.80
PbPb	0.86	0.95		
Yield				
pp	93	79	38	42
PbPb	9.0	11		

4.7.1. Closure test of the fitting procedure

The raw B_s^0 yields obtained from MC are corrected for the acceptance and selection efficiencies and also compared with the generated B_s^0 yields. Hence the yield extraction procedure can be validated. The mass spectrum obtained from the signal MC are represented in Figure 4.12.. The ratio of the corrected over generated yields as a function of p_T in pp and PbPb analysis are shown in Figure 4.13. Consequently, this study shows that the results are in a good agreement with unity within uncertainties.

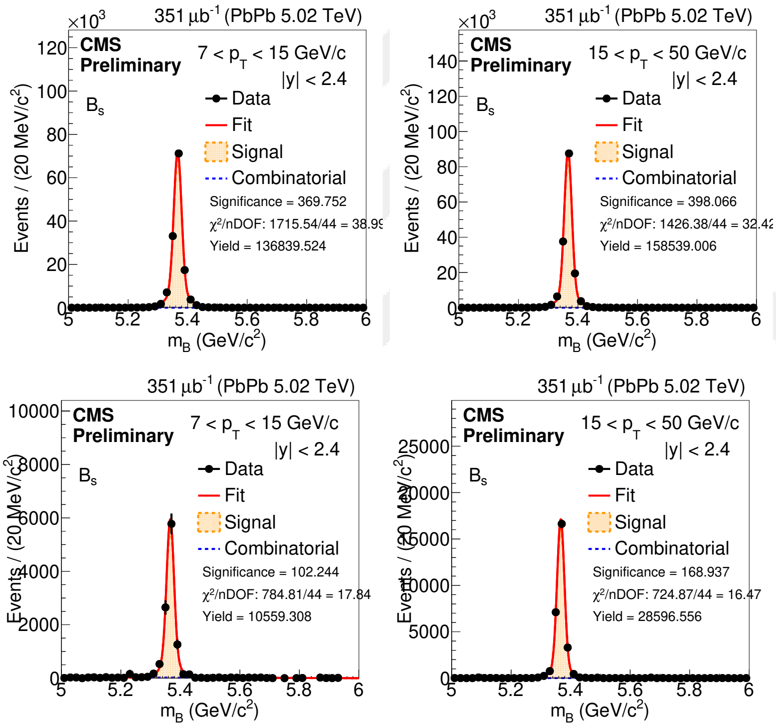

Figure 4.12. The mass spectrum obtained from the signal MC for pp (upper) and for PbPb (lower) are represented.

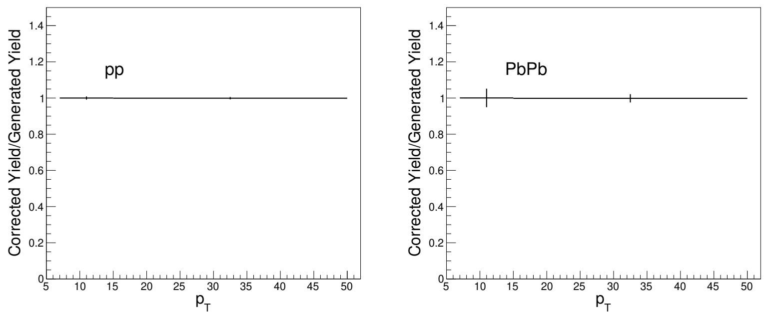

Figure 4.13. The ratio between number of signal extracted from mass fitting which is corrected for efficiency and from generated yields are shown. Closure test for MC for the pp analysis (left) and the PbPb analysis (right).

4.8. Fit Results Examinations

4.8.1. Toy Fit Study

In order to be ensure our fit results are stable, the toy study is performed. 5000 toy data were generated using the fit function from our nominal results showed in Figure 4.9. and Figure 4.10. which is mentioned in the section 4.7.. Following that the fit was applied to each toy data and then the fit parameters with its error were collected. For each parameter a pull distribution was generated by taking into account of the normalized distinction between the nominal parameter value and the fitted value for each individual toy. The RooMCStduy module in Roofit was used to perform whole procedure. As a result of toy study, for the pp and PbPb a pull distribution, the mean parameter which is the mean value of the double Gaussian and the parameter errors are represented in Figure 4.14. and Figure 4.15.. Due to lack of the data statistics the PbPbs spectrum has some fluctuation. In spite of that the width of the fitted Gaussian is very close to unity for both pp and PbPb which is expected for a standard pull distribution.

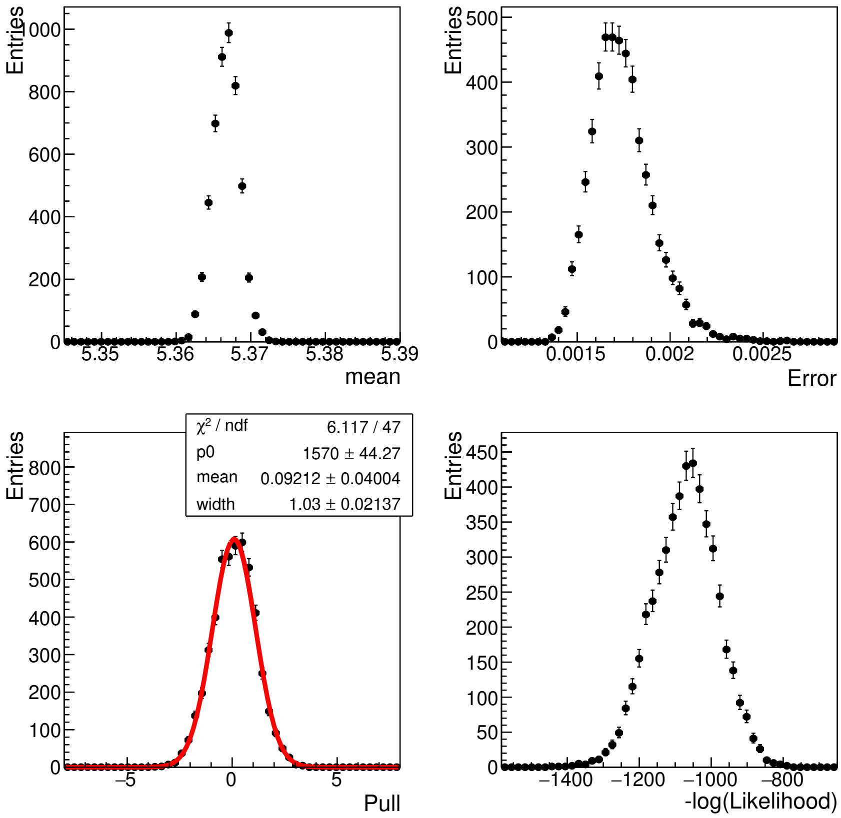

Figure 4.14. Toy study for parameter mean for pp analysis. The fitted values are shown on the top left panel while top right panel presents the parameter errors. Bottom left located for a pull distribution. A Gaussian fit is applied on this distribution. Bottom right plot shows the likelihood value of each fit.

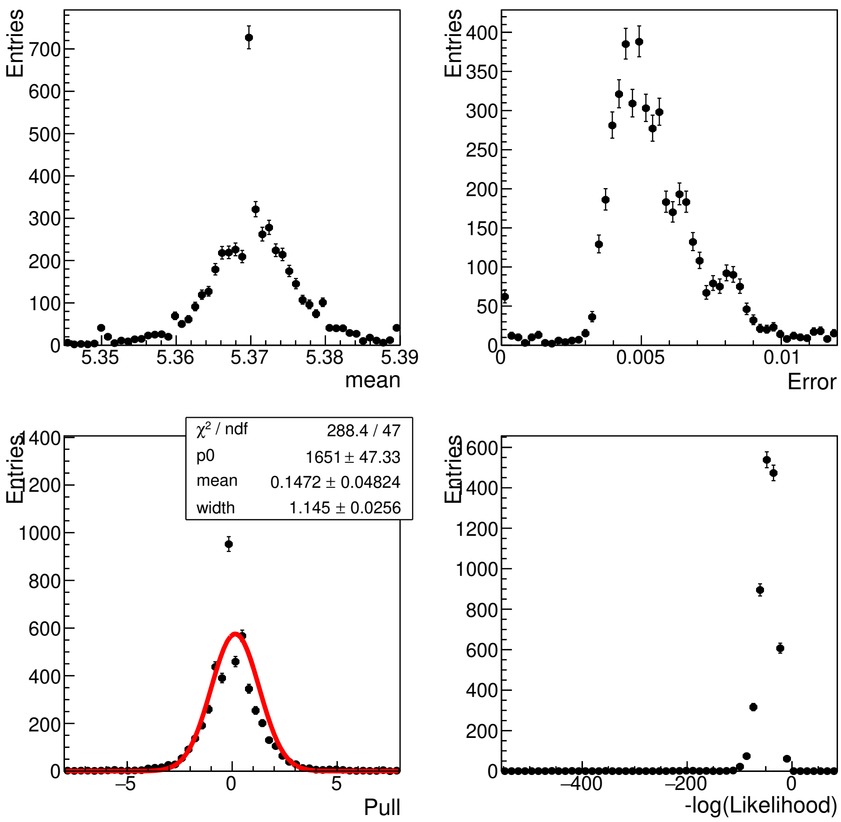

Figure 4.15. Toy study for parameter mean for PbPb analysis. The fitted values are shown on the top left panel while top right panel presents the parameter errors. Bottom left located for a pull distribution. A Gaussian fit is applied on this distribution. Bottom right plot shows the likelihood value of each fit.

4.8.2. Hypothesis testing

The hypothesis testing is performed to determine which parameter of interest is the signal yield. The null hypothesis associated with background only (zero signal yield) hypothesis. The alternative hypothesis compatible with a signal yield equals to the fitted signal yield in the nominal result which is summarized in Table 4.4.. The RooStat package was used to evaluate this procedure. The test statistic considered here is profiling likelihood ratio with frequentist calculator for handling the nuisance parameters. For each hypothesis, 50000 toys are generated. The Figure 4.16. represents the test statistics distribution and the Table 4.5. summarise the corresponding null p-value, significance, and CL quantities.

Table 4.5. Summary table of null p-value, significance, CL_b, CL_{s+b}, and CL_s

	null p-value	**significance**	CL_b	CL_{s+b}	CL_s
pp	0	inf	0	0.39412	inf
PbPb	0.00096	3.10234	0.00096	0.45772	476.792

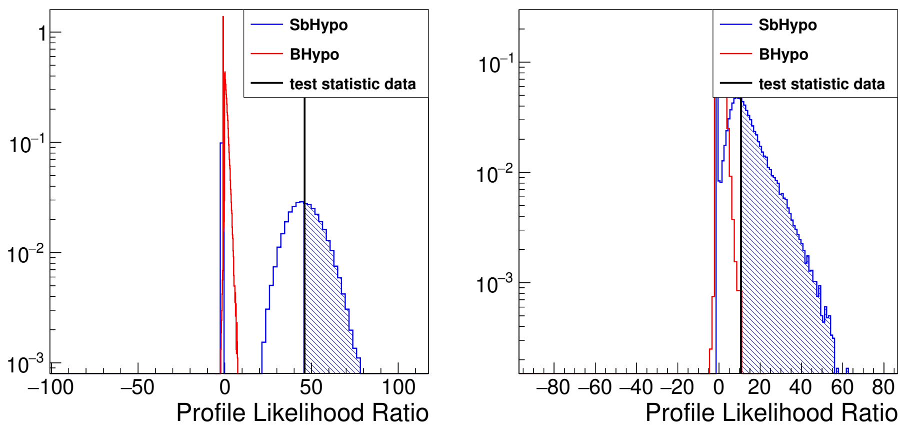

Figure 4.16. The test statistics distribution for null (red) and alternative (blue) hypothesis for pp (top) and PbPb (bottom).

4.9. Acceptance and Efficiency

In order to find the acceptance (denoted as α) and the reconstruction selection efficiency (denoted as ε) of $B_s^0 \to J/\psi + \phi$ decay, the MC simulation is used. This process aims to estimate the sensitivity for this decay in the data. By the acceptance and the efficiency, the number of recorded events in the detector is reduced. Some events cannot be recorded because they can slip through the blind spots of the detector, due to the coverage of the detector is not 100%. Hence the acceptance of detector plays a vital role in event loss. The acceptance and efficiency corrections are extracted in each p_T and $|y|$ interval using a sample of signal decay generated. The definition of efficiency is:

$$\varepsilon^{B_s} = \frac{N^{B_s}_{mc,reco}}{N^{B_s}_{mc,gen}} \tag{4.5}$$

where the denominator is the number of generator level signal events in the given p_T-$|y|$ interval that passes kinematic selections and the numerator is the number of signal events reconstructed in the same p_T-$|y|$ interval that pass all offline selection requirements. The definition of acceptance is :

$$\alpha^{B_s} = \frac{N^{B_s}_{mc,gen}(\texttt{with kinematic cuts})}{N^{B_s}_{mc,gen}} \tag{4.6}$$

where the denominator is the number of generator level signal events in the given p_T-$|y|$ interval, and the numerator is the number of generator level signal events produced in the same p_T-$|y|$ interval that pass all kinematic cuts.

The studies based on the signal-only sample for pp while the embedded signal samples for PbPb. In this section, α and ε will be represented individually for both pp and PbPb samples. Furthermore, for pp analysis, a 3-bin α and ε as a function of B_s^0 p_T will be shown which is provided to derive the pp 3 bin cross section measurement.

4.9.1. Acceptance and Efficiency from pp and PbPb MC

The acceptance is described as the fraction of B_s^0 mesons generated within $|y| < 2.4$ and p_T interval under consideration that have daughters, muons and kaons must be passed the single muon and track acceptance selections in the generated level. As for the kaons, the track p_T and η selections are also the same as the offline reco level track selections described in Section 4.4.3. In terms of the reconstruction selection efficiency, it can be defined as the fraction of the B_s^0 with daughters which are passed the acceptance requirements mentioned above. Besides that, they are reconstructed and passed the selection conditions which are expressed in Section 4.4.1. and 4.5. The acceptance factors and the total efficiencies for pp and PbPb collisions are shown in In Figure 4.17., 4.18. and the 3 p_T bin pp acceptance and total efficiencies are represented in the lower panel of the Figure 4.18.

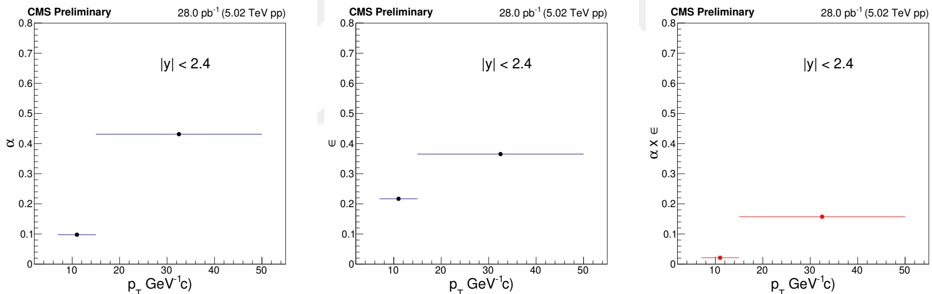

Figure 4.17. The left plot shows the B_s^0 acceptance, middle plot is efficiency, and the right plot is the efficiency $\times$ acceptance for the pp analysis.

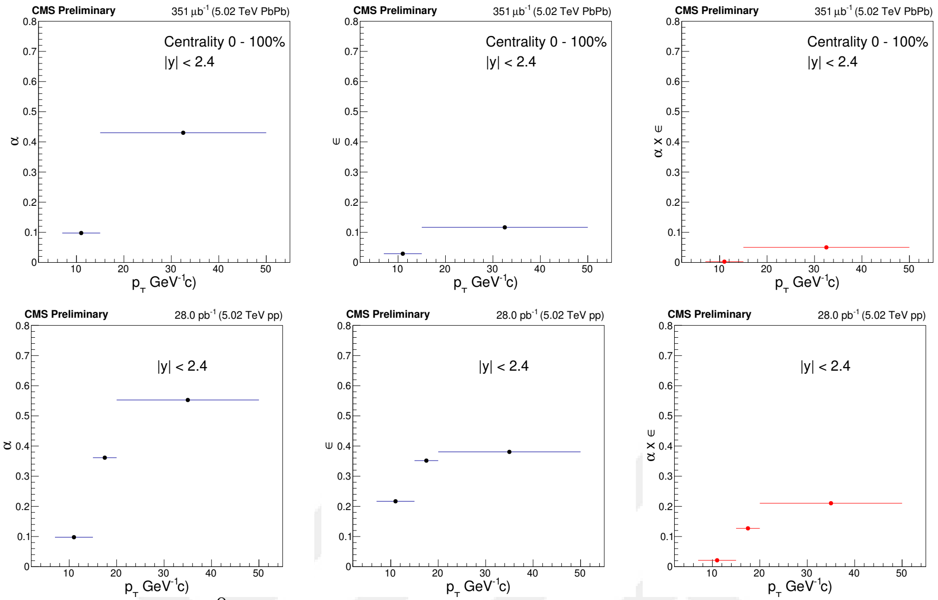

Figure 4.18. The B_s^0 acceptance is on the upper left, efficiency in the upper middle, and efficiency $\times$ acceptance is shown on the upper right for the PbPb analysis. The lover plots are related to the 3 p_T for pp analysis and the acceptance of B_s^0 is shown on the lower left, efficiency is in the lower middle, and efficiency $\times$ acceptance on the lower right for the pp analysis.

4.10. FONLL pp Reference

Fixed Order Next to Leading Logarithm (FONLL) is a model for calculating the total or single inclusive heavy quark (charm or bottom) production differential cross sections at different $\overline{pp}$ or pp collisions with various cuts on B_s^0 or rapiditiy (η). For this analysis the FONLL calculations was obtained for a generic admixture of B mesons and baryons in pp collisions with rapidity y <2.4 (CMS Collaboration, 2017a). Parton Distribution Functions (PDFs) were taken into account for this calculation. Besides, the central values were evaluated considering m_c=1.5 GeV and m_b=1.5 GeV, and the renormalization and factorization scales μ_R=μ_F=$\mu_0 = \sqrt{\mathrm{m}^2 + \mathrm{p}_\mathrm{T}^2}$. In terms of the uncertainty which was calculated varying the perturbative parameters in the range between 4.5< m_b <5 GeV/c^2 and 1.3< m_c <1.7 GeV/c^2 while renormalization and factorization parameters μ_F and μ_R independently in the range 0.5 $< \mu_F/m_T < 2$, $0.5 < \mu_R/m_T < 2$ with the constraint of $0.5 < \mu_F/\mu_R < 2$. Afterwards the FONLL calculation for generic B mesons was rebinned corresponding to the p$_T$ intervals defined for the different analysis. The B_s^0 p$_T$ differential cross sections are obtained by scaling the FONLL results with the PDG measured fraction (10.3%). The FONLL p$_T$ differential cross section of B_s^0 mesons is shown in Figure 4.19.

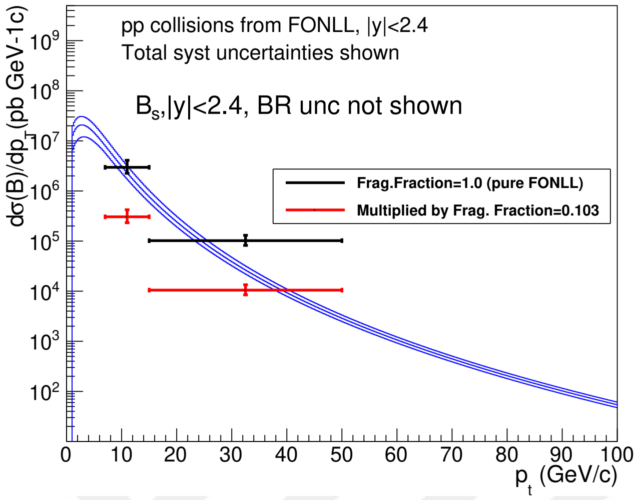

Figure 4.19. FONLL calculation for the p_T-differential cross section of B_s mesons in pp collisions at $\sqrt{s}$=5.02 TeV. The blue curves represent the unbinned FONLL result with its total uncertainty. The black points refer to the rebinned result for B_s^0 mesons and the red points indicate the binned FONLL uncertainty scaled by the Fragmentation Fraction FF=0.103

4.11. Production Cross Section Measurement

One of the main goal of this analysis is to determine the cross section for the production of B_s^0 mesons which decaying to J/ψ and ϕ channel with both pp and PbPb data recorded by CMS detector in 2015. The differential cross sections, $\frac{d\sigma}{dp_T}$ and $\frac{d\sigma}{dy}$ are defined as functions of the transverse momentum p_T and rapidity y. The p_T differential production cross sections of the B_s^0 meson production is defined for each p_T interval as follows:

$$\left.\frac{\mathrm{d}\sigma^{\mathrm{B_s^0}}}{\mathrm{d}p_T}\right|_{|y|<2.4} = \left.\frac{1}{2}\frac{1}{\mathcal{BL}}\frac{1}{\Delta p_T}\frac{N_{\mathrm{pp}}^{(\mathrm{B_s^0}+\overline{\mathrm{B_s^0}})}(p_T)}{\alpha_{\mathrm{pp}}(p_T)\varepsilon_{\mathrm{pp}}(p_T)}\right|_{|y|<2.4} \quad (4.7)$$

where :

- N^{B_s} is the raw $B_s \to J/\psi\phi$ signal yield extracted in each p_T interval. The signal number is corrected for a fraction of reconstructed and generated candidates in p_T interval of width Δp_T

- Δp_T, are the width of p_T intervals.
- $\mathcal{L}$ is the total integrated luminosity of the data sample.
- $\mathcal{B}$ is the total branching ratio of the decay chain, which is $(6.03 \pm 0.21) \times 10^{-5}$, obtained by combining the world averaged values of the branching ratios for BR ($B_s^0 \to J/\psi\phi$)= BF($J/\psi \to \mu^+\mu^-$)×BF($\phi \to K^+K^-$) from the PDG (P. D. Group, 2014).
- $(\alpha\varepsilon)_{pp}$ represents the acceptance times efficiency correction. The correction factor are obtained using PYTHIA and HIJING simulations.

Assuming that present measurement B_s^0 and $\bar{B}_s^0$ production cross sections are equal in the kinematic region. Therefore the factor 1/2 accounts for the yields are measured for particles and antiparticles added together. However, the cross section is accounted for one species (B_s^0) only. The p_T differential cross section of B_s^0 mesons in the rapidity region $|y| < 2.4$ has been calculated according to Equation 4.7 for pp collisions at $\sqrt{s}$=5.02 TeV. The results are summarized in Figure 4.20. and Figure 4.21. for both integrated 2-bin and 3-bin p_T ranges, respectively. The scaled PbPb cross section is explained in the next section 4.11.1.

The vertical bars around the data points refer to statistical (systematic) uncertainties in both Figure 4.20. and Figure 4.21.. The systematic uncertainty bars here comprise both the correlated and uncorrelated contributions added in quadrature. The global systematic uncertainty, listed in the legend and not included in the point-to-point uncertainties, includes the uncertainties in the integrated luminosity measurement and in the branching fraction B. In order to compare the results, the FONLL calculation at the same energy is superimposed on the same plot and represented by

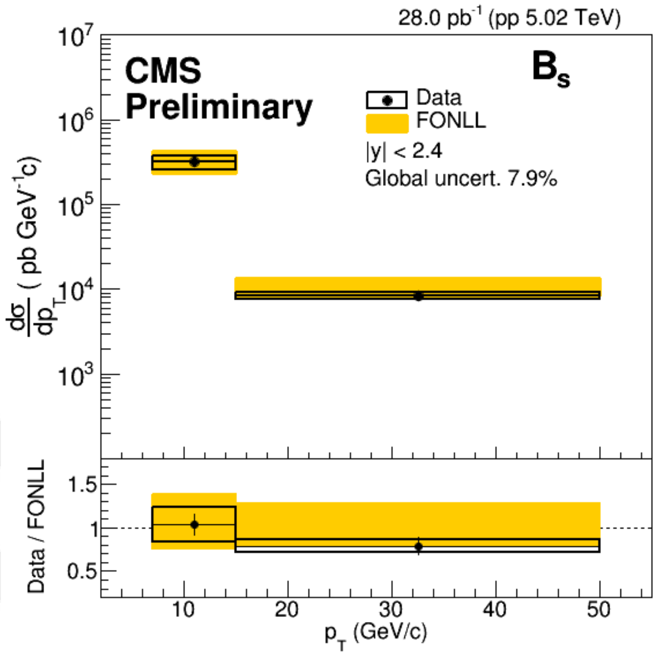

Figure 4.20. Summary of the p_T differential production cross section for pp sample in the p_T interval 15 to 50 GeV/c. The black points represents the data and the FONLL calculations at the same energy is superimposed which is represented by the colored yellow boxes. The boxes around the data points indicate the total systematic uncertainties.

the colored yellow boxes with the heights indicating the theoretical uncertainty. Additionally, the ratio of the measurement over the FONLL calculation is also shown. The pp results are compared to the predictions of fixed-order plus next-to-leading logarithm (FONLL) calculations. According to Table 4.6. and Table 4.7., the results indicate that the CMS results for B$_s^0$ meson cross section consistent with the FONLL theoretical prediction.

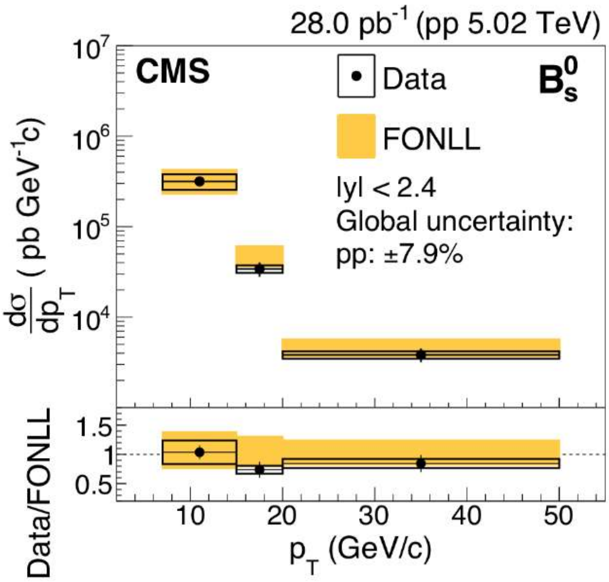

Figure 4.21. Summary of the p_T differential cross section for pp sample in the p_T interval 7 to 15, 15 to 20, +and 20 to 50 GeV/c.

Table 4.6. Summary table of pp cross section in 2-p_T region 7-15 and 15-50 GeV/c.

pp cross section (pb GeV^{-1}c)	**mean value**	**statistical uncertainty**	**systematical uncertainty**
(7,15)	3.2x10^5	12%	19%
(15,50)	8.3x10^3	13%	9.6%

Table 4.7. Summary table of pp cross section in 3-p_T region 7-15, 15-20 and 20-50 GeV/c.

pp cross section (pb GeV^{-1}c)	**mean value**	**statistical uncertainty**	**systematical uncertainty**
(7,15)	3.2x10^5	12%	19%
(15,20)	3.4x10^4	18%	9.4%
(20,50)	3.8x10^3	17%	9.3%

4.11.1. dN/dp_T and nuclear modification factor in PbPb collisions at 5.02 TeV.

The cross section (dN/dp_T) for PbPb collision is calculated according to the following equation.

$$\frac{1}{T_{AA}} \frac{dN_{PbPb}^{B_s^0}}{dp_T}\bigg|_{|y|<2.4} = \frac{1}{2} \frac{1}{\mathcal{B} N_{\mathrm{MB}} T_A A} \frac{1}{\Delta p_T} \frac{N_{PbPb}^{(B_s^0+\bar{B}_s^0)}(p_T)}{\alpha_{PbPb}(p_T)\,\varepsilon_{PbPb}(p_T)}\bigg|_{|y|<2.4} \quad (4.8)$$

where $N_P^{B_s^0} bPb$ is the raw signal yield extracted in each p$_T$ interval of width Δp_T, $N_M B$ is the number of MB (Minimum Bias) events and T_{AA} represents the nuclear overlap function for PbPb. The scaled PbPb cross section as a function of p_T is represented in the Fig 4.22. and the resulting values are shown in Table. 4.8.

Table 4.8. Summary table of PbPb cross section in 2-p_T region 7-15 and 15-50 GeV/c.

PbPb cross section (pb GeV^{-1}c)	**mean value**	**statistical uncertainty**	**systematical uncertainty**
(7,15)	4.8x10^5	38%	26%
(15,50)	7.3x10^3	32%	16%

The strongly interacting particles conducted as a deconfined QGP. This state can be created by conditions attained in high energy collisions of heavy nuclei. After a while, this state ends up, and then the system cools down and expands following with hadronisation process. The initial stage of the heavy quarks collision are generated in quark-antiquark pairs. They move towards the hot and dense medium with losing their energy caused by collisional processes and gluon radiation. This loss energy can be explained by the modification of the transverse momentum distribution in heavy nuclei collisions(PbPb or AuAu) concerning the pp scaled collision. This modification is evaluated by the nuclear modification factor $R_A A$ which is the ratio between the cross sections distributions for a given process in nucleus-nucleus (PbPb) and pp

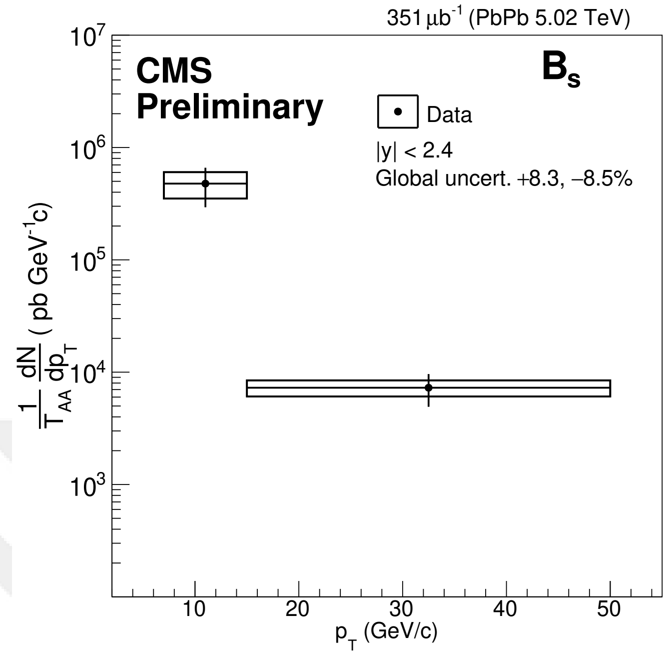

Figure 4.22. The p_T differential corrected yield of B_s^0 scaled by T_{AA} in PbPb collisions at 5.02 TeV in two p_T intervals from 7 to 50 GeV/c.

collisions divided by the T_{AA} nuclear average overlap function (Dogra et al., 2017). The experimental R_{AA} is calculating with the following formula.

$$R_{AA}(p_T) = \frac{1}{T_{AA}} \frac{\mathrm{d}N_{PbPb}^{\mathrm{B_s^0}}}{\mathrm{d}p_T} / \frac{\mathrm{d}\sigma_{pp}^{\mathrm{B}}}{\mathrm{d}p_T} \tag{4.9}$$

The nuclear modification factor in the centrality range from 0 to 100% is shown in Figure 4.23. If there are no nuclear effects, the ratio is expected to be equal to 1. However, the mean value of R_{AA} is found to be 1.5 for p_T range 7 to 15 GeV/c and 0.87 for p_T range 15 to 50 GeV/c with statistical uncertainty of 40% and 35%, and systematic uncertainty of 33% and 19%, respectively. With these values, the mean value is found to be 0.81 and -0.26 sigma above unity. The obtained ratio is smaller than one because the strong suppression of the yield products can be observed in nuclear collisions. The summary table of the R_{AA} and N_{coll}, T_{AA} and N_{part} values for the different centrality bins used in the charged particle R_{AA} analysis can be found in Table 4.9. and Table 4.10., respectively.

Table 4.9. Summary table of R_{AA}

R_{AA}	**mean value**	**statistical uncertainty**	**systematical uncertainty**
(7,15)	1.5	40%	33%
(15,50)	0.87	35%	19%

Table 4.10. Summary of the N_{coll}, T_{AA} and N_{part} values for the centrality bins used in the charged particle R_{AA} analysis.

Centrality	$< N_{coll} >$	$< T_{AA} >$	$< N_{part} >$
0 - 10%	1626±112(6.9%)	23.22±0.392(1.7%)	358.8±1.93(0.54%)
10 - 30%	805.4±53.9(6.7%)	11.51±0.274(2.4%)	226.7±3.65(1.6%)
30 - 50%	267.3±19.7(7.4%)	3.819±0.188(4.9%)	109.2±3.6(3.3%)
50 - 100%	30.76±4.62(15%)	0.4395±0.0642(15%)	21.87±2.44(11%)
0 - 100%	392.5±43.2(11%)	5.607±0.501(8.9%)	114±7.55(6.6%)

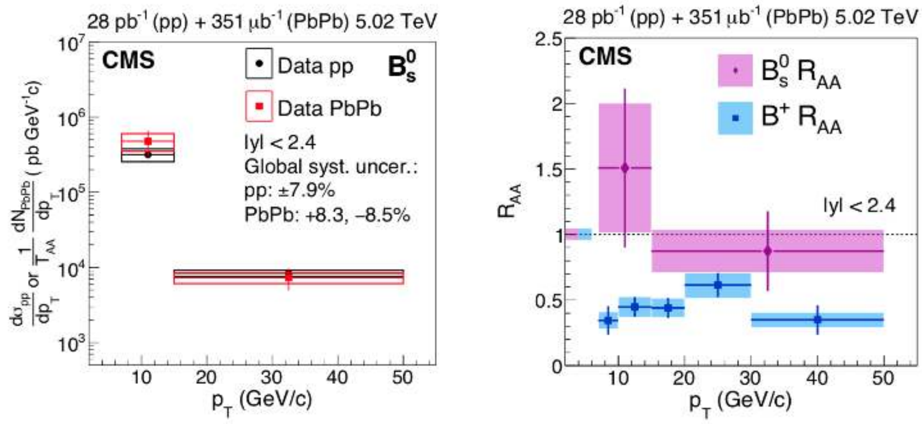

Figure 4.23. The B_s^0 RAA results. The left plot shows the p_T differential production cross section of B_s^0 in pp collisions and the p_T differential corrected yield of B_s^0 scaled by T_{AA} in PbPb collisions at $\sqrt{s}$=5.02 TeV in two p_T intervals from 7 to 50 GeV/c. The vertical bars indicate statistical (systematic) uncertainties. The systematic uncertainty boxes contain both the correlated and uncorrelated contributions added in quadrature. The global systematic uncertainty includes the uncertainties in T_{AA}, N_{MB}, and B_s^0. The right plot describes the nuclear modification factor R_{AA} of B_s^0 measured in PbPb collisions at $\sqrt{s}$=5.02 TeV from 7 to 50 GeV/c. The vertical boxes correspond to statistical (systematic) uncertainties. The global systematic uncertainty, shown as a grey box at R_{AA} = 1, contains the uncertainties in the integrated luminosity measurement and T_{AA} value.

4.11.2. Nuclear modification factor ratio

The ratio of the nuclear modification factor between B_s^0 R_{AA} (calculated in section 4.11.1.) and B^+ R_{AA} (calculated in analysis (**PhysRevLett.119.152301**) is also calculated and represented in Figure 4.24.. The global uncertainty includes luminosity, T_{AA}, etc. and the statistical uncertainty contains tag and probe, acceptance and tracking efficiency is canceled for both analysis. The rest of the systematic uncertainties are quadratic sum of the B_s^0 and B^+ R_{AA} analysis.

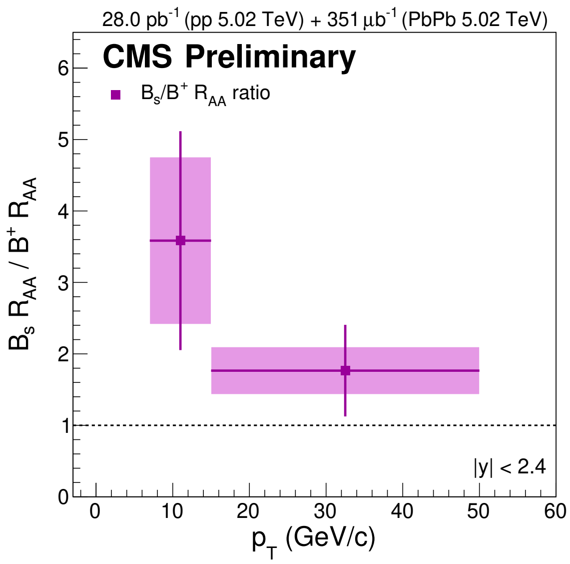

Figure 4.24. The ratio of the nuclear modification factor R_{AA} between B_s^0 and B^+ measured in PbPb collisions at $\sqrt{s}$=5.02 TeV from 15 to 50 GeV/c.

Table 4.11. The ratio of R_{AA} between B_s^0 and B^+ measured in PbPb collisions

B_s^0/B^+ R_{AA}	**mean value**	**statistical uncertainty**	**systematical uncertainty**
(7,15)	3.6	43%	33%
(15,50)	1.8	36%	19%

The mean value of the ratio is evaluated as 3.6 with ±43% statistical and ±33% systematic uncertainties for 7-15 GeV/c, and 1.8 with ±36% statistical and ±19% systematic uncertainties for 15-50 GeV/c, respectively. The results are shown in Table 4.11.. An indication of an enhancement of the B_s^0/B^+ ratio in PbPb with respect to pp collisions is observed as expected in the case of a strong contribution of beauty recombination in heavy ion collisions. However, given the substantial uncertainties, the enhancement is not significant enough to reach a conclusive answer. This analysis demonstrates the capability of performing fully reconstructed B_s^0 measurement in PbPb collisions with the CMS detector.

4.12. Systematic Uncertainties

There are several contributions on systematic uncertainties for differential cross section measurements. The cross sections are affected by several sources of systematic uncertainties arising from the signal extraction, corrections, branching ratio, luminosity or T_{AA} determination as well as hadron tracking, muon and selection efficiency.

4.12.1. Branching Ratio

The systematic uncertainty on the BR for the J/ψ and φ decays are calculated by adding in quadrature the uncertainties on each sub-channel with $J/\psi \to \mu^+\mu^-$ and $\phi \to K^+K^-$. As a result the uncertainty for the full $B_s^0 \to J/\psi\ \phi$ decay chain is 7.57% (P. D. Group, 2014).

4.12.2. Luminosity

The luminosity uncertainty based on a preliminary look at the Van der Meer (VdM) scan data is estimated to be 2% in pp collisions. VdM scans performs with a dedicated LHC machine set-up, in this case CMS. It provides to measure the luminosity per colliding bunch pair. In terms of PbPb collisions, the luminosity uncertainty related with the counting of the number of minimum bias events which is used to normalize the corrected $dN/d\sigma p_T$ events and it is estimated as 2%. The calculation made with considering the uncertainty on the minimum bias event selection efficiency (Dogra et al., 2017).

4.12.3. Hadron Tracking Efficiency

The uncertainty of the tracking efficiency of a charged hadron track is evaluated bin-by-bin using a data driven technique and is obtained 4% per track in the pp case. The relative efficiency of reconstructing hadron tracks in data is evaluated by measuring the ratio of neutral charm meson decays to final states of D meson analysis (CMS Collaboration, 2016a). The study was performed to reconstruct the D^* meson for 3 and 5 prong decay channels and corrected by branching ratio (BR) differences using 5 TeV pp data in 2015. However, this study was not feasible for PbPb case due to having larger combinatorial background. Therefore, a more conservative tracking uncertainty was determined as 6% per track.

4.12.4. Muon efficiency: Tag and Probe

The Tag and Probe (TnP) method is a powerful data-driven approach which is used to have reliable single muon tracking, identification and trigger efficiency measurements. This method utilises a well-known dimuon mass resonances such as J/ψ mesons to select tag and probe muon tracks. The ”tag” is an object that passes a set of tight selection requirements for isolating the required particle type like muons. The ”probe” refers to an object which selected with potentially very loose selection criteria to avoid the biasing the efficiency. Tag muon needs to pass the high p_T muon ID, match with the generated muon and also with one of the muons passing the trigger while Probe muon is just a track muon with a very loose cut on p_T. Besides, Tag and

Probe muons should be with opposite charge.

For this analysis, the TnP method (C. H. I. Group, 2016) for both pp and PbPb collisions is performed bin by bin using a data driven technique. We take into account the efficiency differences as systematic uncertainty preferably to apply a muon efficiency correction. In addition to the muon scaling factor used for MC samples, uncertainties on these scaling factors are considered in this analysis. Consequently, the muon efficiency for the p_T 7 to 15GeV/c inclusive results 4.4% for pp and 3.1% for PbPb and for the p_T range 15 to 50GeV/c, 3.2% for pp and 3.8% for PbPb collisions. Furthermore, the results for pp 3 bin p_T range 7 to 15, 15 to 20, and 20 to 50GeV/c were observed 4.2, 3.4, 3.0, 2.8% , respectively.

4.12.5. Selection Efficiency

The systematic uncertainty due to the selection of the B_s^0 meson candidates is evaluated by comparing the result with using a cut-based algorithm in the multivariate analysis and by comparing the result between the BDT discriminant in pp and PbPb. The discrimination of the correct yields between BDT and cut-based methods is considered as a systematic uncertainty for pp analysis. According to this calculation, the uncertainty is estimated to be 15% and 2.6% for p_T 7 to 15 and 15 to 50GeV/c bins. The Figure 4.25. represents the resulting pp mass spectrum and cross section. The same procedure could not be applied to the PbPb data. Because, when the cut base method used for PbPb samples, no signal obtained due to not having enough statistic. Therefore, The BDT discriminant trained using PbPb data and MC was applied on pp data and MC samples. According to observations presented in Appendix D with Figure D4. and Figure D5., given the fact that the distributions of the various variables for signal B_s^0 between pp MC and PbPb MC show similarity, the PbPb discriminant BDT value for B_s^0 signal generated by using pp samples should be close

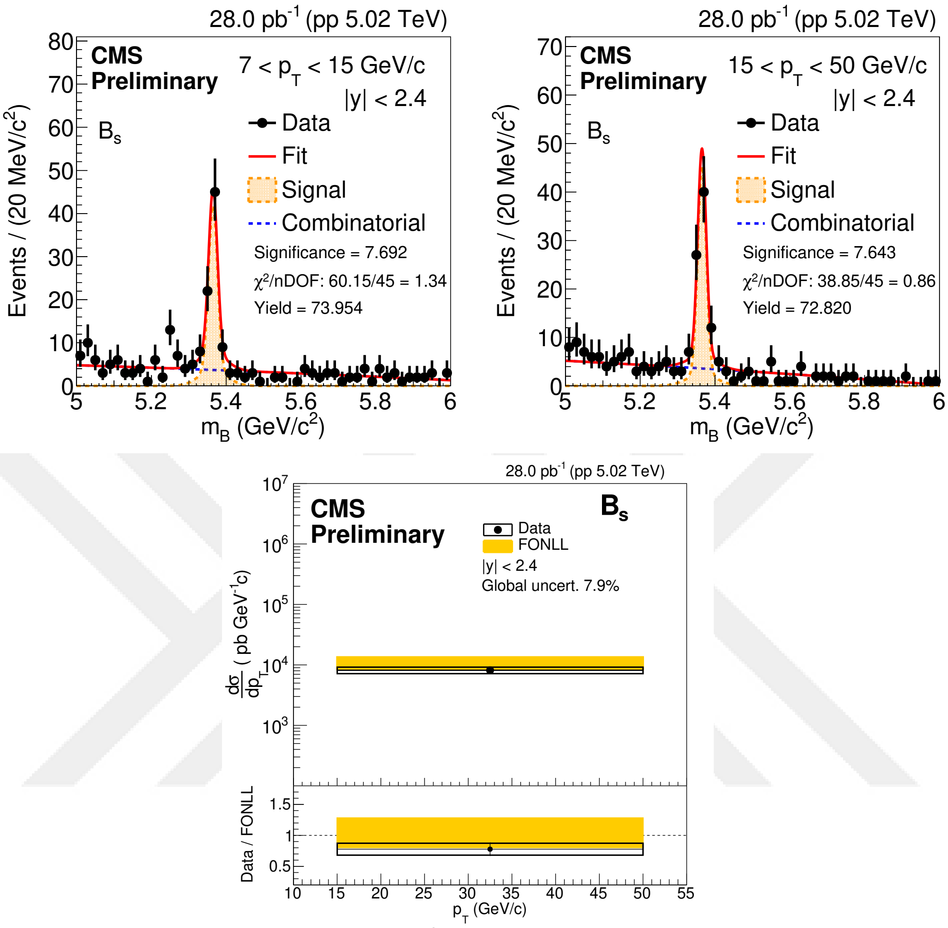

Figure 4.25. The top left plot shows B_s^0 invariant mass spectrum for p_T range 7 to 15GeV/c and the top right plot correspond to B_s^0 invariant mass spectrum for p_T range 15 to 50GeV/c. The bottom one refers to the corresponding cross section using a cut-base MVA method for p_T interval 7 to 50 GeV/c in pp data.

to the signal produced with PbPb samples. Thus, the systematic uncertainty for the PbPb analysis evaluated as the difference in the correct yields between pp BDT and PbPb BDT. It is estimated to be 19% for p_T range 7 to 15GeV/c and 8.6% for 15 to 50GeV/c. The resulting B_s^0 invariant mass spectrum and cross section using the PbPb BDT discriminant in pp data for p_T interval 7 to 50GeV/c is shown in Figure 4.26..

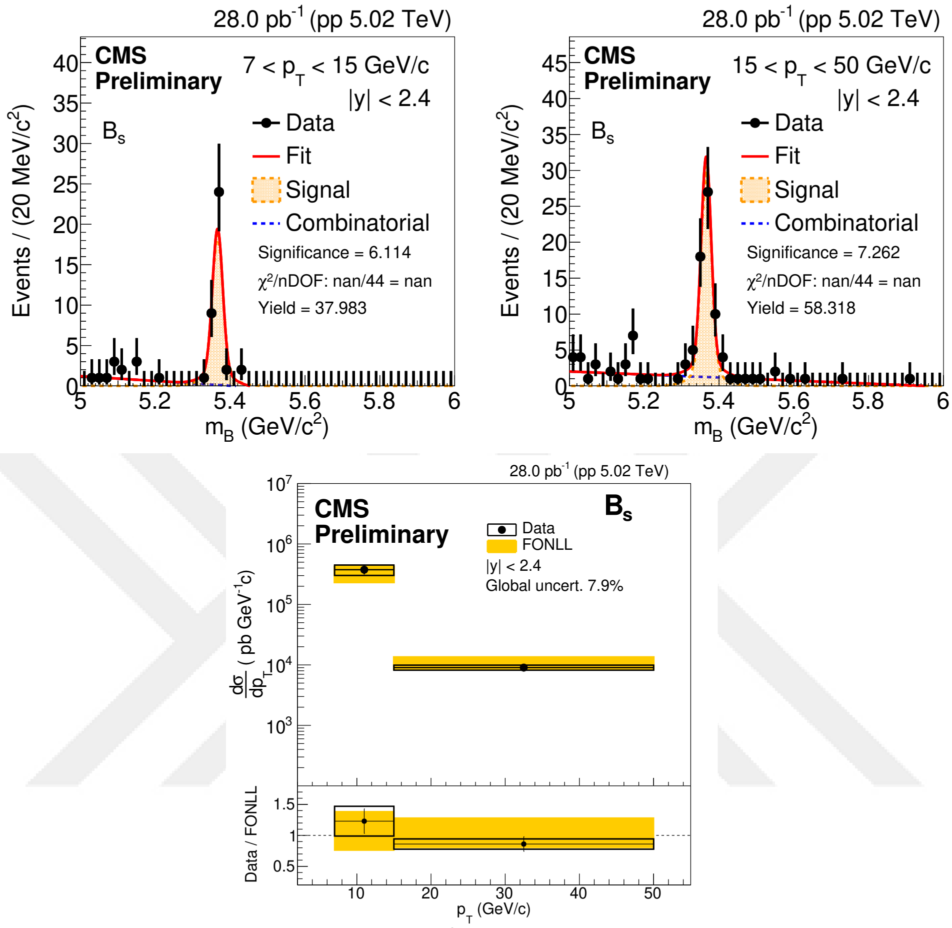

Figure 4.26. The top panels show the B_s^0 invariant mass spectrums for p_T interval 7 to 15GeV/c (left) and for 15 to 50 GeV/c (right). The bottom panel refers to the corresponding cross section using the PbPb trained BDT discriminant for p_T interval 7 to 50 GeV/c in pp data.

4.12.6. Systematics Associated with Signal Extraction Fit

The default background PDF is defined by 1st. order polynomial function as discussed in Section 4.7. In this section, the various PDF conditions are used to check its effects on B_s^0 yield extraction. The uncertainty of the modeling of the background shapes is evaluated by varying the probability distribution functions used to describe the background to high order polynomial and exponential. The background PDF is changed to 2nd order polynomial, 3rd order polynomial and exponential functions. Afterwards, B_s^0 raw yields from these fits are compared with the yield from the default fit (linear) function. The maximum yield difference of all background PDF variations propagated as the systematic uncertainty associated with background PDF. The values of different background PDF variations for pp and PbPb collisions are available in Table 4.12. and Table 4.13. In Appendix E, the B_s^0 invariant mass fit results for both pp and PbPb with applying linear (default), 2nd order polynomial function, 3rd order polynomial, and exponential functions as background PDF are represented in Figure E1. and Figure E4.

Table 4.12. Summary table of signal extraction uncertainty associated with background PDF in 5.02 TeV pp collisions.

p_T(GeV/c)	**2nd Poly**	**3rd Poly**	**Exp**	**Max Percentage(%)**
7−15	3.3	3.4	1.3	3.4
15−50	1.5	1.6	1.6	1.6

Table 4.13. Summary table of signal extraction uncertainty on background PDF in 5.02 TeV PbPb collisions.

p_T(GeVc)	**2nd Poly**	**3rd Poly**	**Exp**	Max **Percentage(%)**
7−15	8.7	8.5	0.31	8.7
15−50	0.15	0.68	0.021	0.68

The uncertainty of the modeling signal shape is evaluated by considering four fit variations:

- *Increase/decrease the width parameters determined from MC*: To examine the signal shape directly from data and possible difference between data and MC, the fits result variation is evaluated by increasing and decreasing the width of signal by the error ($\sigma(1+\alpha) \to \sigma(1+\alpha \pm Error_\alpha)$)
- *Use a single and triple Gaussian function*: The effect is checked by changing the signal PDF function form default setting which is modeled by a double Gaussian to a single Gaussian and a triple Gaussian.
- *Use a sum of three Gaussian functions with a common mean*:In the fitting procedure, the same mean value of the signal PDF is used for the three Gaussian functions.
- *Fix the mean of the Gaussian to the value determined by MC*: while in the default setting the mean value of the double Gaussian is a floating parameter, we also checked the effect of fixing the mean to the value obtained by fitting on signal MC .

In Appendix E, the differences between the models on signal PDF is represented in Figure E5. E8. for both pp and PbPb collisions. The systematic uncertainty associated with signal PDF is based on the maximum yield difference (by comparing the default setting) among all different types of signal PDF variations. The uncertainties of signal PDF variations are presented in Table 4.12. to 4.13. for both pp and PbPb collisions. The final systematic uncertainty is propagated as the maximum of the signal variations is added in quadrature to the maximum of all the background variations. The systematic uncertainty due to the selection of the B_s^0 meson candidates is estimated by comparing the result with using a cut based algorithm in the multivariate analysis and by comparing the results between the BDT discriminant in pp and PbPb. The results are documented in Table 4.16.

Table 4.14. Summary table of signal extraction uncertainty on signal width for pp p_T bin 7 to 15 and 15 to 50 GeV/c bin in 5.02 TeV

p_T(GeV/c)	**1 Gauss**	**3 Gauss**	**Decrease width**	**Increase width**	**Fixed mean**	**Max Percentage (%)**
7−15	2.5	0.85	0.049	0.049	0.50	2.5
15−50	0.69	0.21	0.051	0.051	0.14	0.69

Table 4.15. Summary table of signal extraction uncertainty on signal width in 5.02 TeV PbPb collisions for p_T bin 7 to 15 and 15 to 50GeV/c.

p_T(GeV/c)	**1 Gauss**	**3 Gauss**	**Decrease width**	**Increase width**	**Fixed mean**	**Max Percentage (%)**
7−15	4.2	0.36	0.17	0.17	0.50	4.2
15−50	3.5	0.59	0.057	0.055	0.19	3.5

Table 4.16. Summary table of signal extraction uncertainty for pp and PbPb collisions.

p_T(GeV/c)	**Background variation**	**Signal variation**	**Total**
pp 7−15	3.4%	2.5%	4.2%
pp 15−50	1.6%	0.69%	1.7%
PbPb 7−15	8.7%	4.2%	9.7%
PbPb 15−50	0.68%	3.5%	3.6%

4.12.7. Systematics on p_T Shape

The systematic uncertainty on MC p_T shape was considered by the comparison of reconstruction and selection efficiency which is calculated with an unweighted MC sample and a MC sample in which B_s^0 p_T distribution is weighted with regard to the FONLL p_T shape. The systematic uncertainty is evaluated as the difference in efficiency. The inclusive result of systematic uncertainty on MC p_T shape for both pp and PbPb in p_T 7 to 15 and 15 to 50GeV/c and also for 3 p_T bin range for pp is documented in Table 4.17. According to these results, the lower p_T bin has the larger uncertainty because of the rather larger discrepancy on definition of B_s^0 p_T spectrum between PYTHIA and FONLL which can be observed in Figure 4.1. and Figure 4.2.

Table 4.17. Summary table of signal extraction uncertainty for pp and PbPb collisions.

pp	**systematical uncertainty on $p_T$shape**
pp 7−15	6.5%
pp 15−50	2.3%
pp in 3 bin	**systematical uncertainty on $p_T$shape**
pp 7−15	6.5%
pp 15−20	0.46%
pp 20−50	0.90%
PbPb	**systematical uncertainty on $p_T$shape**
PbPb 7−15	7.9%
PbPb 15−50	3.8%

4.12.8. Systematic on Acceptance Correction

Systematical uncertainties on acceptance play an important role due to distinction between real data samples and MC simulation. MC samples are generated by PYTHIA6 and decayed by EvtGen. Additionally, PHOTOS is used for the initial and final state radiation. However, generating MC samples with all these processes can not make guarantee to reproduce real detector condition. The potential discrepancy between real data and MC can affect the acceptance. In this case, the potential sources of discrepancy can be possible due to initial and final state effects and different generator tuning. The assumption of this study is mixing all the effects from various sources and reflecting as the determined discrepancy. The following steps are performed to determine the bin by bin systematic uncertainties associated with acceptance correction.

- Between data and MC, the normalized and uncorrected yield ratio as a function of p_T and η is determined and represented in Figure 4.27. and Figure **??** for pp collision.
- For PbPb analysis, the ratio derived for pp collision is used due to limited size of statistic available in PbPb samples.
- 10k toy ratios is generated by using Gaussian distribution. Mean value and sigma of the Gaussian is considered as the ratio and ratio error, respectively. According to the running time 5k or 10k samples are generated randomly.
- The linear and 2nd order polynomial fit functions are applied to the generated toy ratios. These fitted parameters are recorded for the next step. The fitting results are represented in Figure 4.27.
- According to the determined fitted functions, the MC acceptance weighted for each toy ratio.
- The minimum, maximum and mean values are calculated from each distribution.

In brief, the bin-by-bin systematic uncertainties correspond to the acceptance correction are evaluated by varying the shape of the generated B_s^0 meson p_T and η spectra within limits determined by the differences (including their statistical uncertainties) between data and MC calculations. With these shape variations, “toy” MC simulations are used to recalculate the acceptance in each kinematic bin. As a result, the systematic uncertainty is evaluated with the variations between the nominal acceptance and the toys. The resulting acceptance distribution is represented in Figures 4.28. where upper panel shows pp p_T binning result and lower panel represents the pp rapidity binning results and values are documented in Table 4.18. and Table 4.20.

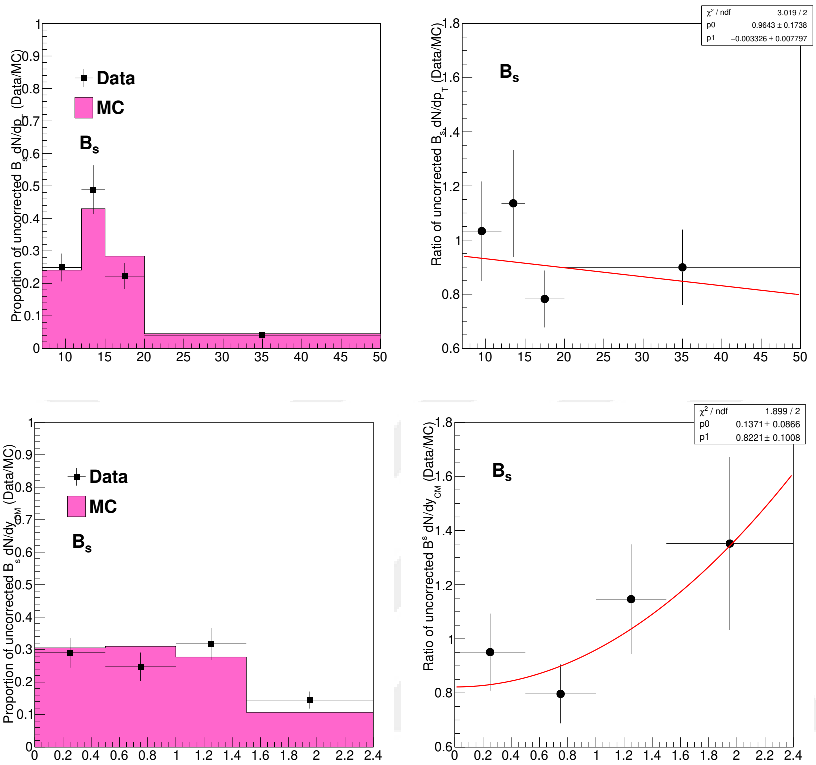

Figure 4.27. Normalized and uncorrected yield of data and MC which is shown on the upper and lower left and ratios are represented on the upper and lower right with p_T binning and rapidity binning for collisions, respectively. A Linear function is used for fitting for p_T binning while 2nd order polynomial function is used for rapidity binning.

Table 4.18. Summary of variated acceptance and final systematic uncertainties from p_T and rapidity variation for pp analysis

Variation	7,15 GeV/c	15,50 GeV/c
Default	0.098	0.43
p_T var Mean	0.097	0.43
p_T var RMS	0.0012	0.0053
rapidity var Mean	0.098	0.43
rapidity var RMS	0.00037	0.0026
Uncertainties(%)	1.7	1.8

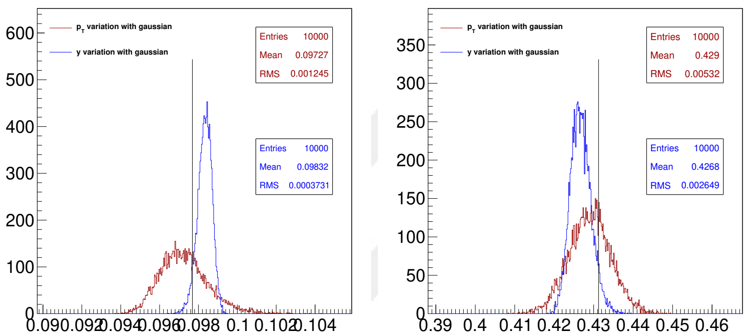

Figure 4.28. Variated acceptance distribution from toy pp MC determined by p_T and rapidity distribution fitting. The red color refers to p_T distribution while blue one is rapidity. The plot on the left corresponds the B_s^0 p_T from 7 to 15 GeV/c and the right one is from 15 to 50 GeV/c. The black line in the middle shows the nominal acceptance value in the analysis.

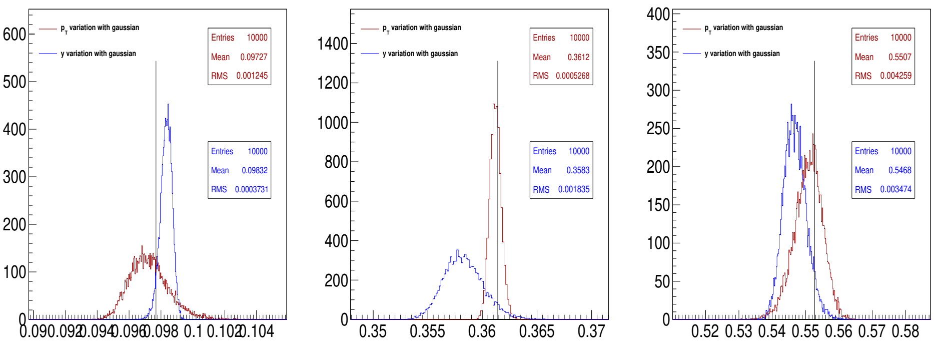

Figure 4.29. Variated acceptance distribution from toy pp MC obtained by p_T (red) and rapidity (blue) distribution fitting. B_s^0 p_T from 7 to 15 GeV/c (left), from 15 to 20GeV/c (middle), and from 20 to 50 GeV/c (right). The black line in the middle is the nominal acceptance value in the analysis.

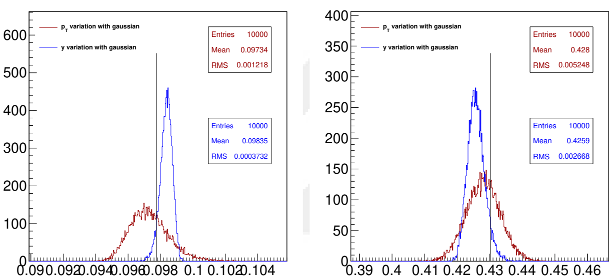

Figure 4.30. Variated acceptance distribution from toy pp MC determined by p_T and rapidity distribution fitting. The red color refers to p_T distribution while blue one is rapidity. The left plot corresponds the B_s^0 p_T 7 to 15 GeV/c and the right one is for 15 to 50 GeV/c. The black line in the middle shows the nominal acceptance value in the analysis.

Table 4.19. Summary of variated acceptance and final systematic uncertainties from p_T and rapidity variation for pp 3 bins analysis

Variation	7,15 GeV/c	15,20 GeV/c	20,50 GeV/c
Default	0.098	0.36	0.55
p_T var Mean	0.097	0.36	0.55
p_T var RMS	0.0012	0.00052	0.0043
rapidity var Mean	0.098	0.36	0.55
rapidity var RMS	0.00037	0.0018	0.0035
Uncertainties(%)	1.7	1.4	1.7

Table 4.20. Summary of variated acceptance and final systematic uncertainties from p_T and rapidity variation for PbPb analysis

Variation	7,15 GeV/c	15,50 GeV/c
Default	0.098	0.43
p_T var Mean	0.097	0.43
p_T var RMS	0.0012	0.0052
rapidity var Mean	0.098	0.43
rapidity var RMS	0.00037	0.0027
Uncertainties(%)	1.7	1.7

4.12.9. Summary Tables

The summary tables and plots of various systematic uncertainties for pp and PbPb collisions are documented in Table 4.21. and represented in Fig 4.31.

Table 4.21. Summary of systematic uncertainties from each factor in pp analysis. All the value is shown in percentage.

Factors	(7,15)	(15,50)
Hadron tracking efficiency	8%	8%
B selection efficiency	15%	2.6%
p_T shape	6.5%	2.3%
TnP systematic	4.4%	3.1%
Acceptance systematic	1.7%	1.8%
PDF variation background	3.4%	1.6%
PDF variation signal	2.5%	0.69%
MC stat.	0.78%	0.47%
Total	19%	9.6%
Luminosity	2.3%	2.3%
Branching fractions	7.6%	7.6%

Table 4.22. Summary of systematic uncertainties from each factor in pp 3-bins analysis. All the value is shown in percentage.

Factors	(7,15)	(15,20)	(20,50)
Hadron tracking efficiency	8%	8%	8%
B selection efficiency	15%	2.6%	2.6%
p_T shape	6.5%	0.46%	0.90%
TnP systematic	4.4%	3.3%	3.0%
Acceptance systematic	1.7%	1.4%	1.7%
PDF variation background	3.4%	1.6%	1.6%
PDF variation signal	2.5%	0.69%	0.69%
MC stat.	0.78%	0.76%	0.53%
Total	19%	9.4%	9.3%
Luminosity	2.3%	2.3%	2.3%
Branching fractions	7.6%	7.6%	7.6%

Table 4.23. Summary of systematic uncertainties from each factor in PbPb analysis. All the value is shown in percentage.

Factors	(7,15)	(15,50)
Hadron tracking efficiency	12%	12%
B selection efficiency	19%	8.6%
p_T shape	7.9%	3.8%
TnP systematic	5.1%	3.8%
Acceptance systematic	1.7%	1.7%
PDF variation background	8.7%	0.68%
PDF variation signal	4.2%	3.5%
MC stat.	4.9%	2.1%
Total	26%	16%
N_{MB}events	2%	2%
T_{AA}	+2.8 -3.4%	+2.8 -3.4%
Branching fractions	7.6%	7.6%

Table 4.24. Summary of systematic uncertainties from each factor in R_{AA}. All the value is shown in percentage.

Factors	(7,15)	(15,50)
Hadron tracking efficiency	14%	14%
B selection efficiency	24%	9.0%
p_T shape	10%	4.4%
TnP systematic	6.7%	4.9%
Acceptance systematic	2.4%	2.5%
PDF variation background	9.3%	1.7%
PDF variation signal	4.9%	3.6%
MC stat.	5.0%	2.2%
Total	33%	19%
Luminosity	2.3%	2.3%
N_{MB}events	2%	2%
T_{AA}	+2.8 -3.4%	+2.8 -3.4%

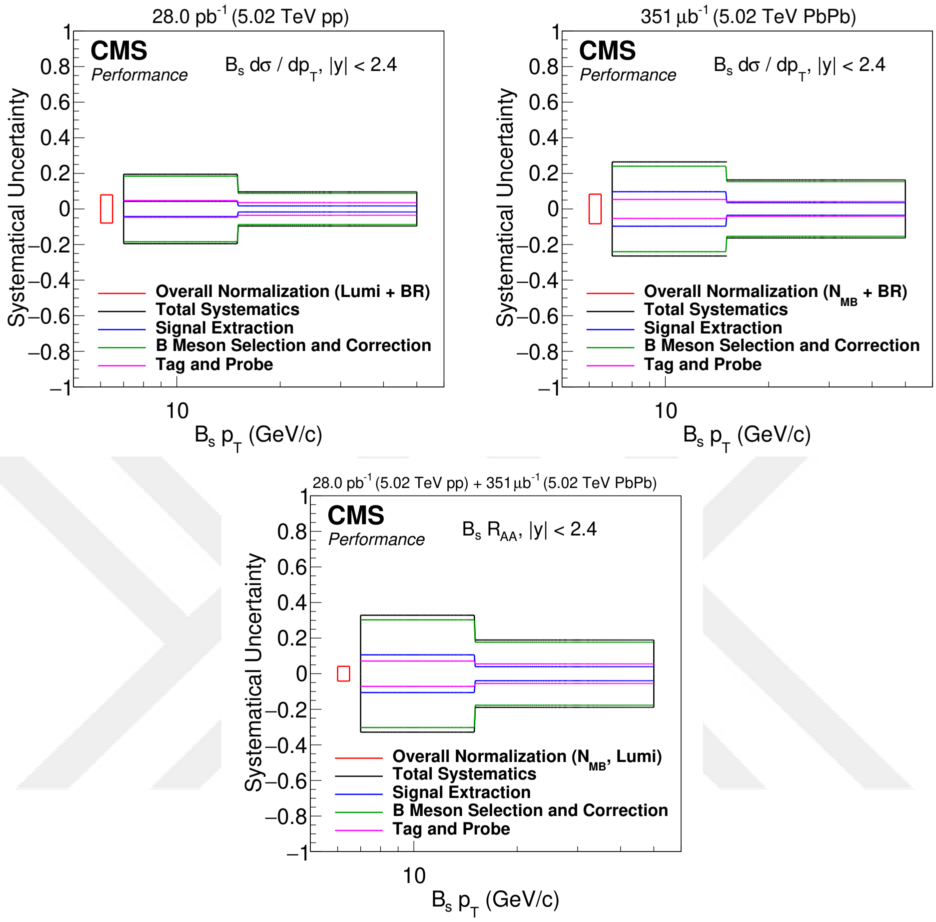

Figure 4.31. Summary plots of the systematic uncertainties for pp collisions represented on the left, PbPb collisions on the right and R_{AA} on the bottom. The red color refers to overall normalization from Lumi+Branching ratio, black line shows the total systematic, blue is signal extraction, green is B meson selection and correction and pink refers the Tag and Probe uncertainties.

4.13. ϕ meson mass window pre-selection

The selection criteria of BDT discriminant cut value was conducted by determining the working point which provides the highest signal significance as well as unaffected by non prompt peaking background. In order to remove the peaking background a tighter ϕ meson (track pair) window must be applied with considering the advantage of the narrow ϕ meson natural width. Despite the fact that ϕ mass window is one of the variables for BDT training, the non prompt background may not be properly removed from the optimal working point. To analyze this effect, the BDT training study for pp was redone with different ϕ mass window pre-selections with 0.005, 0.01, 0.015, 0.025, 0.05, 0.1 GeV/c, and no pre-selection. Afterwards the ϕ mass and B_s^0 mass distributions is compared between gen-matched B_s^0 and non-prompt background using pp non-prompt J/ψ MC samples. The resulting mass spectrum are represented in Fig. 4.32. and Fig. 4.33. According to these figures, the non-prompt peaking background contribution under B_s^0 signal region in the B_s^0 mass spectra is fairly suppressed with a pre-selection below 0.015 GeV/c.

Following this, we compared how the real pp data spectra looks like after these different pre-seleciton in BDT training. The comparison results can be found in Fig. 4.34. and Fig. 4.35. Consequently, the better final signal significance is observed with the broader mass window pre-selection. However, the non-prompt background contribution is properly suppressed by applying the intermediate value of 0.015 GeV for this analysis.

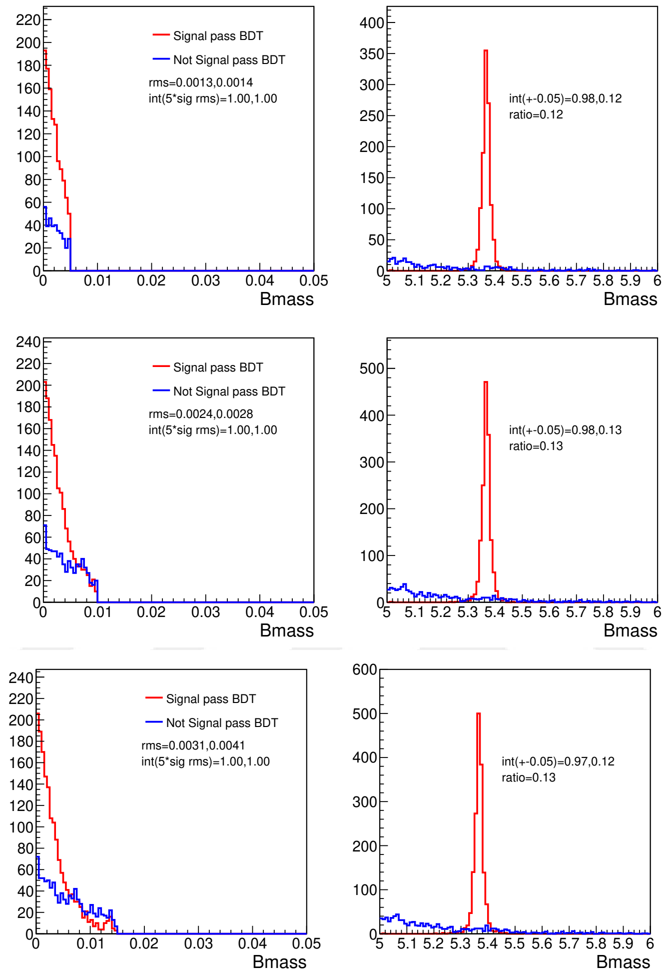

Figure 4.32. Red line refers to gen-match B_s^0 signal while blue line for non-prompt background. The absolute difference between track pair mass and PDG ϕ meson mass is shown on the left panel. The reconstructed B_s^0 mass is located on the right histogram. From top to bottom corresponding to 0.005, 0.01, and 0.015 GeV ϕ mass window pre-selection.

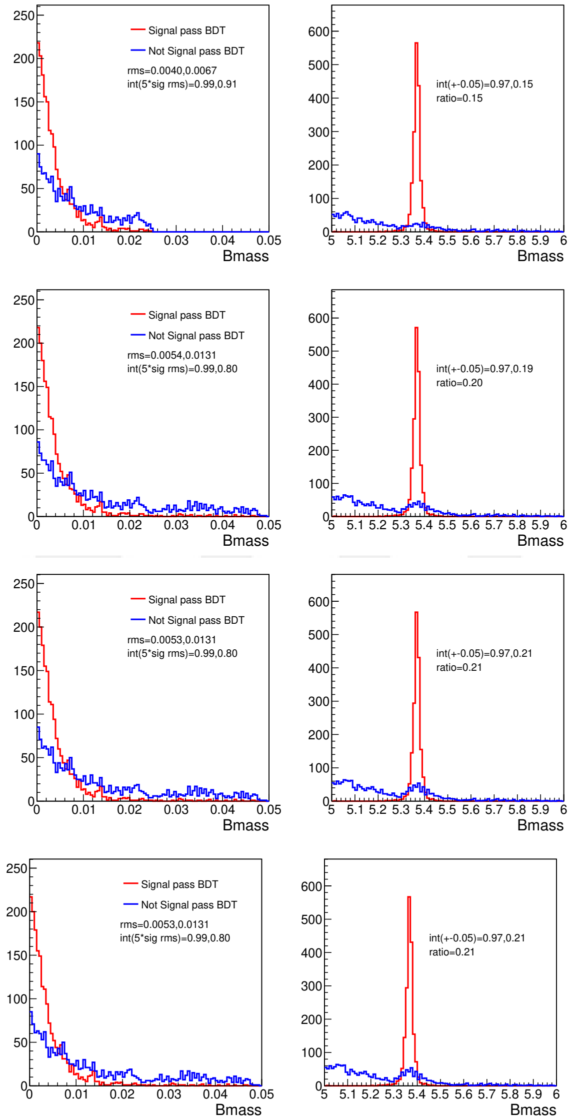

Figure 4.33. The red line represents the gen-match B_s^0 signal and blue line is for non-prompt background. On the left panel the absolute difference between track pair mass and PDG ϕ meson mass is shown whereas Right panel is related to the reconstructed B_s^0 mass. From top to bottom corresponding to 0.025, 0.05, 0.1 GeV, and no (i.e., infinite) ϕ mass window pre-selection.

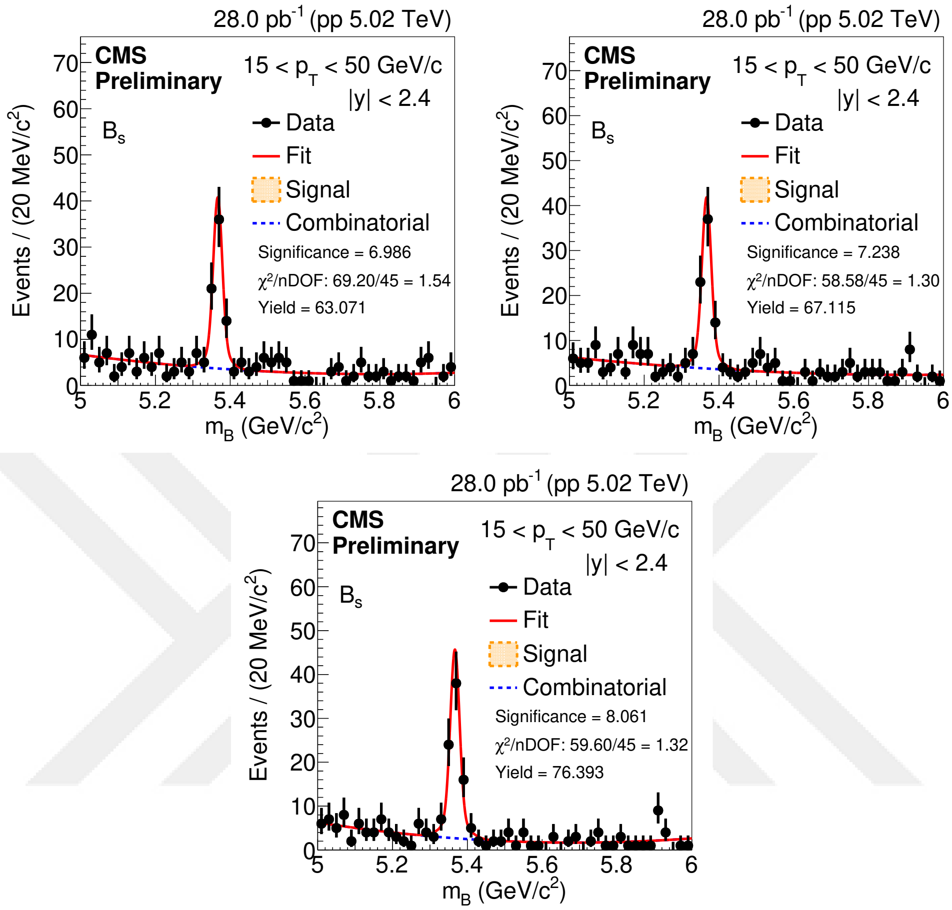

Figure 4.34. The reconstructed B_s^0 mass spectra in pp data with different ϕ mass window pre-selection. Top left shows the result with 0.005 GeV, top right with 0.01 GeV and bottom is with 0.0 15 GeV pre-selection.

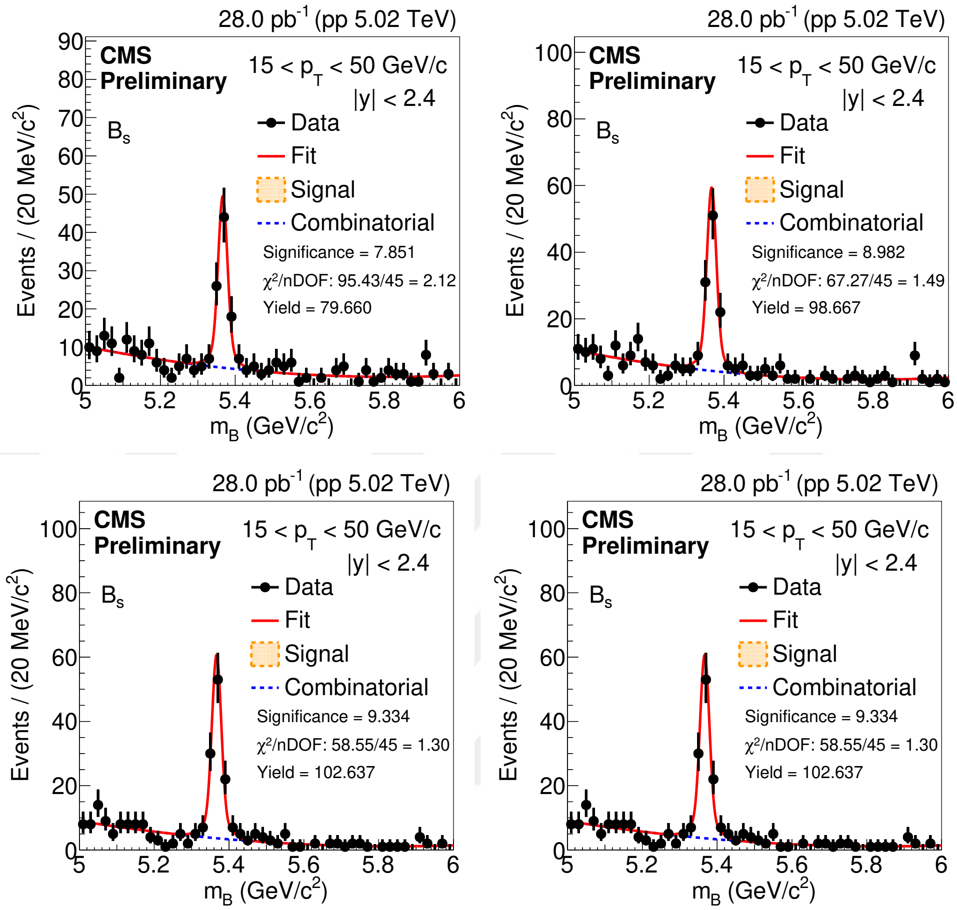

Figure 4.35. The reconstructed B_s^0 mass spectra in pp data with different ϕ mass window pre-selection. Top left is plotted with 0.025 GeV, top right is with 0.05 GeV, bottom left is with 0.1 GeV pre-selections and bottom right is plotted with no pre-selection

4.14. Non-prompt (NP) J/ψ Background

The production of J/ψ mesons occurs in three ways. The prompt J/ψ produced directly in the pp collision or indirectly via the decay of heavier charmonium states, and non-prompt J/ψ from the decay of a b hadron. Non-prompt J/ψ lead to a measurement of the b-hadron cross section. There are potential background feed-down sources coming from other B meson decays in the B_s^0 invariant mass spectrum. These sources form a peaking structure in the region of interests. In order to prevent the potential bias of the yield extraction procedure, the peaking background structures need to be properly studied. To determine these components, we processed the inclusive B meson (i.e., non-prompt J/ψ) MC samples with the nominal B_s^0 channel work flow. We then classify each reconstructed B_s^0 candidate by their gen-level particle, e.g. whether it is coming from a B^0, B^+ or other decays that falls into the B_s^0 reconstruction work flow, in order to measure their individual contribution to the peaking structure. Only a relatively small contribution from other B meson is observed. After applying optimal cuts, only negligible non-prompt contribution is left. This is due to the narrow ϕ meson natural width allowing us to impose a tight track-pair mass window and thus remove a large fraction of non-prompt contribution which does not have an intermediate ϕ resonance.These contributions are presented below.

4.14.1. Individual channel contributions of NP Background

There are many small contributions that gives the form to the peaking background structure. We can not identified each of them individually but most of the contributed ones are determined. Below is a list of example processes that compose of the majority of the peaking background:

- 1 st case $X \to J/\psi\pi^- K^+$, here pion is mis-identified as kaon

- 2 nd case $B_s^0 \rightarrow J/\psi K^+K^-$, in which both Kaons are not coming from the decay of an intermediate ϕ meson resonance.
- 3 rd case $B^+ \rightarrow J/\psi K^+$, (added extra K^-)
- 4 th case $X \rightarrow J/\psi\pi^+\pi^-$, pions mis-identified as Kaons.
- 5 th case $B_s^0 \rightarrow J/\psi K^+K^-X$
- 6 th case $B_s^0 \rightarrow J/\psi\phi\pi\pi$
- 7 th case $B^0 \rightarrow J/\psi K^{*0}$
- 8 th case $\chi_{1c} \rightarrow J/\psi\gamma$
- 9 th case $\psi_{2s} \rightarrow J/\psi X$

The following plots show the contribution of the determined channels with respect to the total background for both pp and PbPb. The peak at the B_s^0 signal region was investigated and found out that mostly contributed channels are $B^0 \rightarrow J/\psi K^{*0}$ in blue color and $B_s^0 \rightarrow J/\psi K^+K^-$ in red color.

The distribution of the non prompt background components with respect to the total background represented in Figure 4.36. while the distribution of the NP background components with respect to the B_s^0 signal and also the rest of the small contributions shown in Figure 4.37. and Figure 4.39., both for pp and PbPb respectively. The plots produced in different p_T interval of 7 to 15 and 15 to 50 GeV/c for both for pp and PbPb samples. Left plot corresponds to the individual channels colored separately and the right plot indicates the difference of sum of the channel from total background (red lines) with respect to signal (blue line).

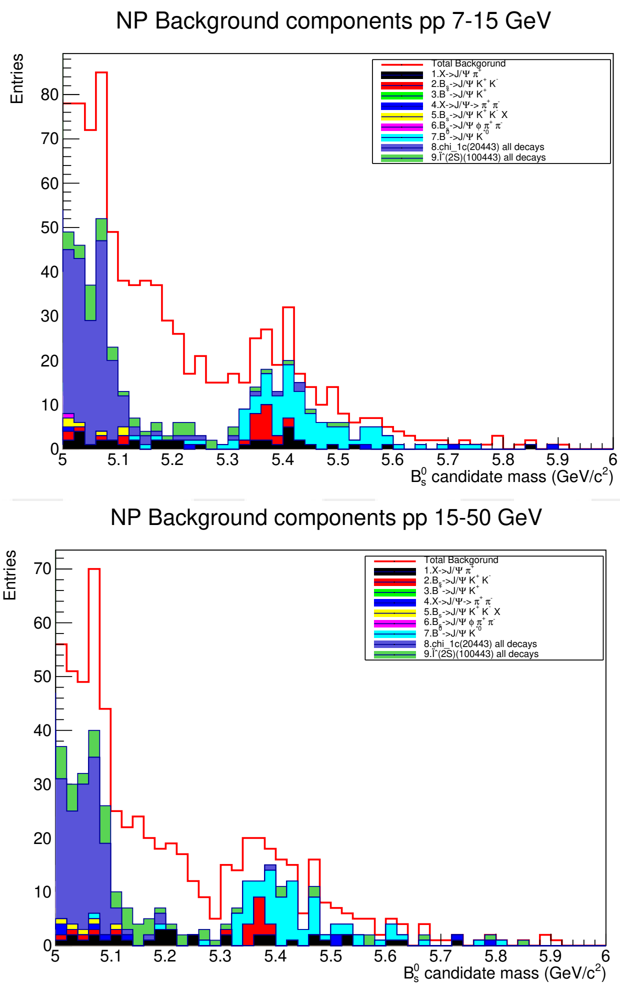

Figure 4.36. Individual Non Prompt background contributions with respect to the total background components for 7 to 15 GeV/c (top) and 15 to 50 GeV/c (bottom) for pp sample.

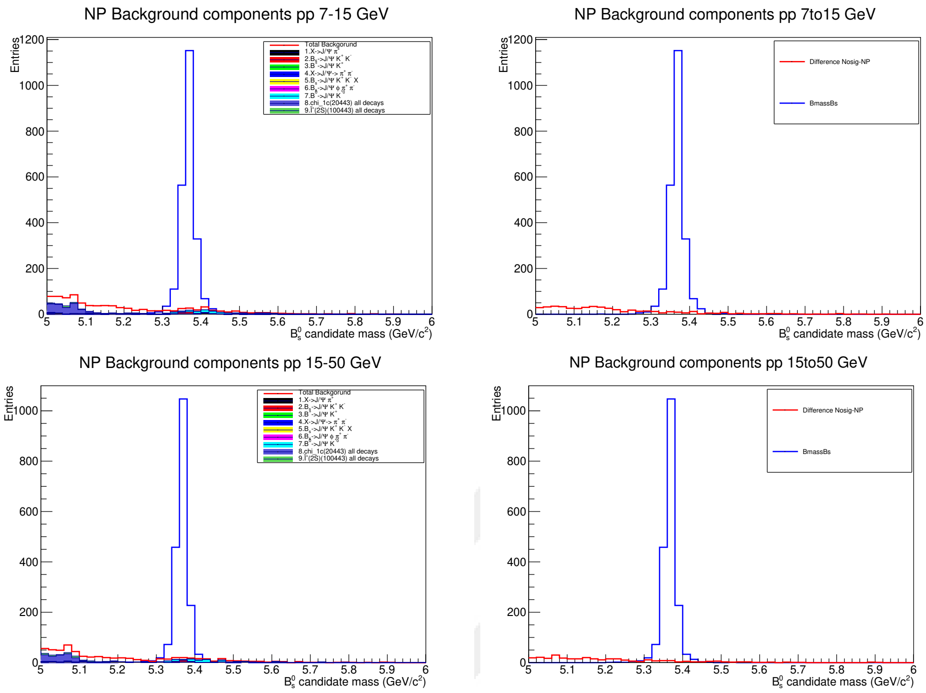

Figure 4.37. Contribution of the Individual Non Prompt Background components produced in different p_T range from 7 to 15 and 15 to 50 GeV/c for pp after optimal cuts. The blue line refers to the B_s^0 signal peak while others are the same as the above plots(top and bottom left plots). The difference of sum of the channel from total background referred with red line with respect to signal (top and bottom right plots).

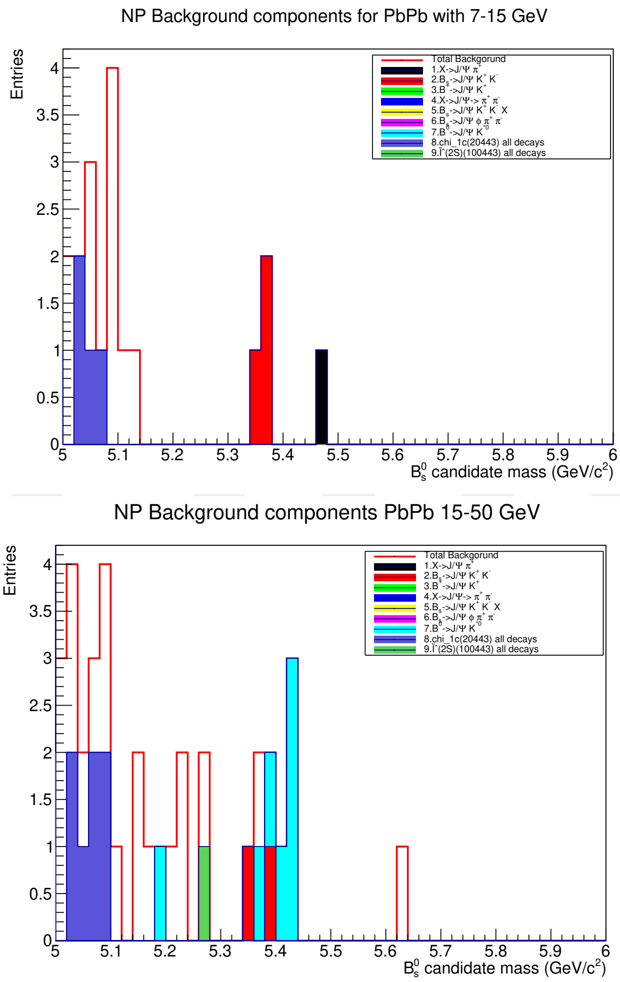

Figure 4.38. Individual Non Prompt background contributions with respect to the total background components in 7 to 15 GeV/c p_T bin (top) and 15 to 50 GeV/c p_T bin (bottom) for PbPb sample.

We also produced the NP peaking backgrounds for pp samples applied with the BDT discriminant trained in PbPb data for p_T interval 7 to 15 GeV/c and 15 to 50 GeV/c. The Figure 4.40. and 4.41. show the individual NP Backgrounds and the comparison of the determined channels with Bs signal.

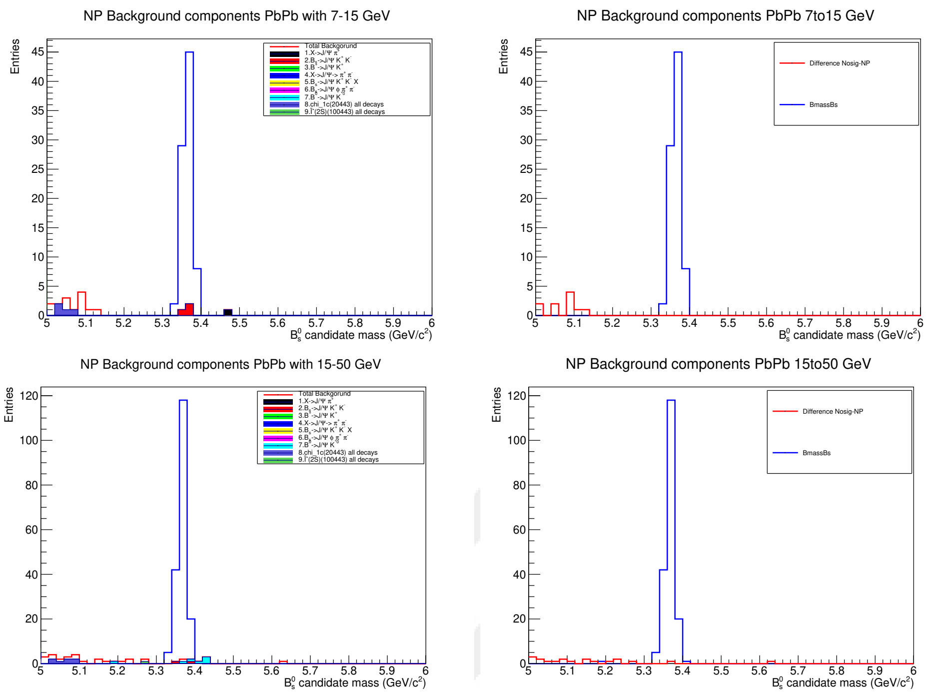

Figure 4.39. Contribution of the Individual Non Prompt Background components produced in different p_T range 7 to 15 GeV/c and 15 to 50 GeV/c for PbPb and comparison of differences of sum of determined channels from total background with B_s^0 signal after optimal cuts.

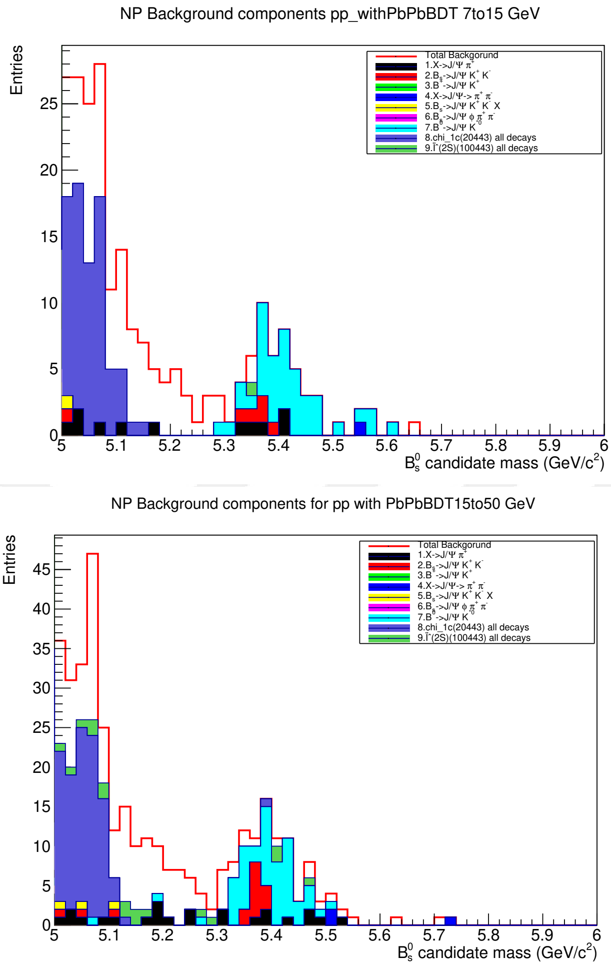

Figure 4.40. Individual Non Prompt background contributions with respect to the total background components applying PbPb BDT cuts which is produced using with pp MC samples for 7 to 15 GeV/c (top) and 15 to 50 GeV/c (bottom).

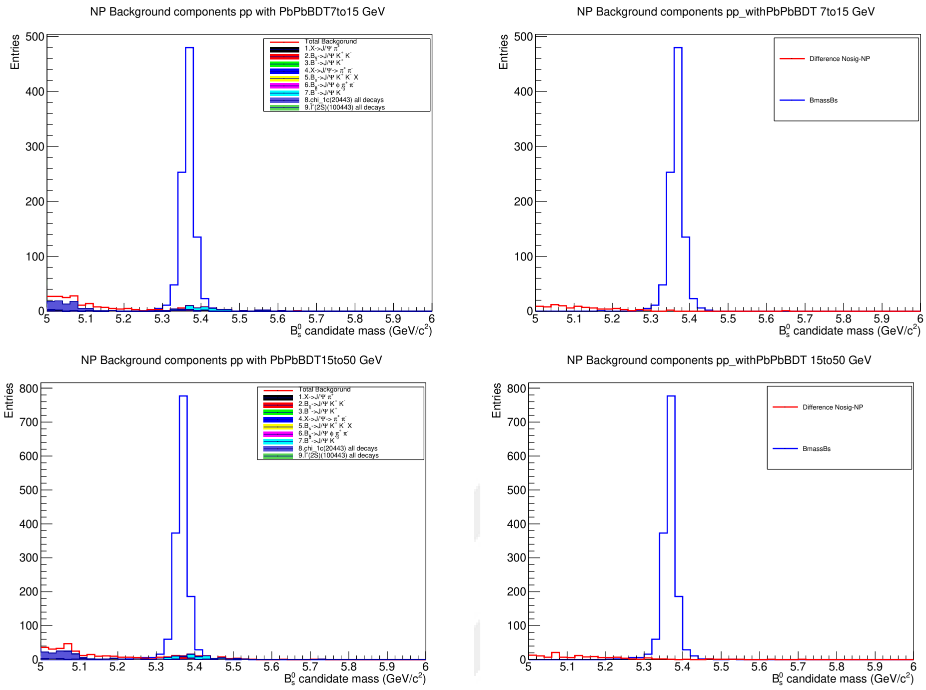

Figure 4.41. Contribution of the Individual Non Prompt Background components for pp with PbPb BDT 7 to 15 Gev/c (upper plots) and PbPb BDT 15 to 50 GeV/c (lower plots) after optimal cuts. The blue line refers to the B_s^0 signal peak while others are the same as the above plots(top and bottom left plots). The difference of sum of the channel from total background referred with red line with respect to signal (top and bottom right plots).

4.14.2. B meson contribution of NP Background

According to the figure 4.36., the red (total background) region is doubly higher than the stack (determined individual NP background) regions in the histogram. We expect that the all NP contribution add up should be equal to red area. The main goal is to model the total background (red) like in figure 4.44. due to fact that this contributes to total fit function as a background component. At first thought this red histogram is basically composed of just a few different components which is defined in section 4.14.1.. However, this study shows there are many small contributions. Those small components together summed up constructing a large background and we can not identify all of them individually. Under this circumstances, another definition of individual component defined. The new definition of the NP background components are listed below;

- 1 st case : $B^+ \to J/\psi X$, all contribution from B^+
- 2 nd case : $B_s^0 \to J/\psi X$, all contribution from B_s^0
- 3 rd case : $B^0 \to J/\psi X$, all contribution from B^0
- 4 th case : Other contributions

In Figure 4.42. the signal region is dominated by the B^0, B^+, and B_s^0 decays while the other channels are contributed on the left side of the mass spectrum. For both pp and PbPb data, the B_s^0 to J/ψ + X (orange region) makes a big contribution.

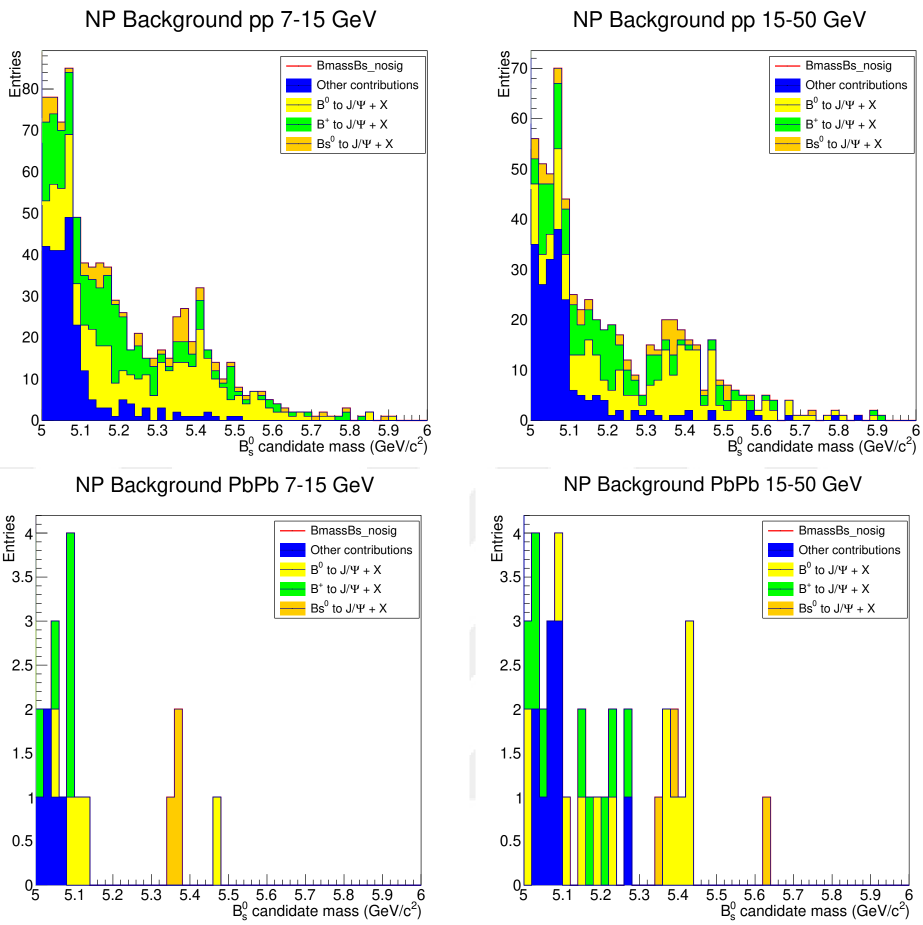

Figure 4.42. B^+, B_s^0, B^0 channels make nearly equal contribution in the signal region for 7 to 15 GeV/c and 15 to 50 GeV/c with pp (upper plots) after applying optimal cuts. In terms of PbPb samples, for 7 to 15 GeV/c p_T range B_s^0 to J/ψ + X (orange region) is the most contributed channel in the signal region but in 15 to 50 GeV/c p_T range, both B_s^0 and B^0 make big contribution.

The Figure 4.43. shows the most contributed channels of the left sideband of the invariant mass spectrum. According to the plot, this area dominated by ψ_{2s} and $\chi_1 c(20443)$ channels.

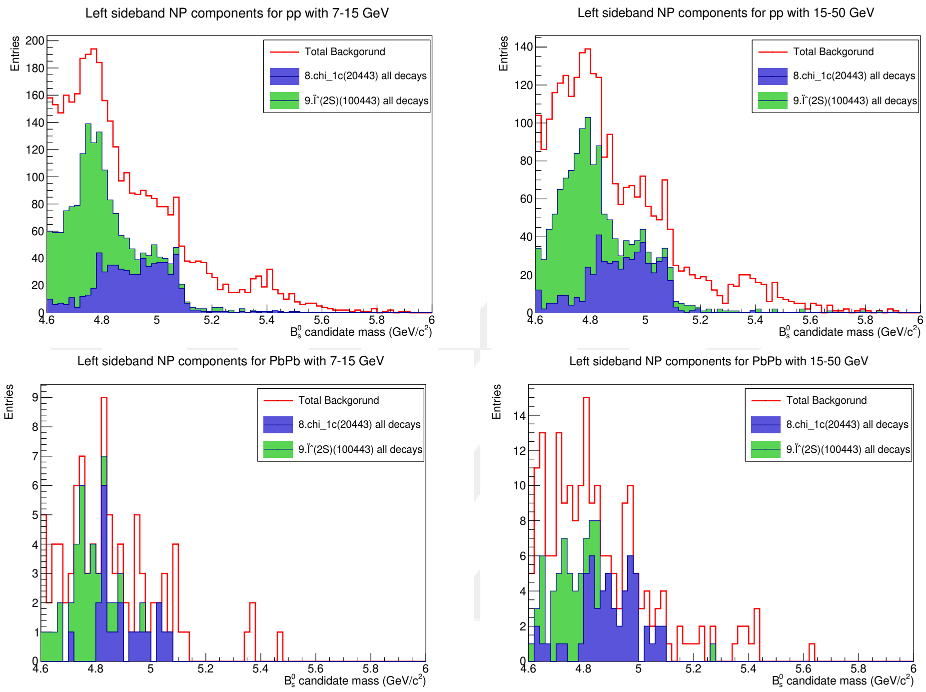

Figure 4.43. $\psi_{2s}(10043)$ and $\chi_1 c(20443)$ channels contributions on the left side mass region for both pp (upper plots) and PbPb (lower plots) in different p_T 7 to 15 and 15 to 50 GeV/c. Green color refers to the contribution of $\chi_1 c(20443)$ and dark blue shows $\psi_{2s}(100443)$ particle channels contributions.

As a result the background model defined and fitted in different p_T range 7 to 15 and 15 to 50 GeV/c for pp and PbPb. Gaussian + error function + double Gaussian fit function were used for pp samples. Here double Gaussian defines the shape at the signal region , while error function and Gaussian defines the shape at the left sideband. Unfortunately, we could not apply fit on PbPb samples due to lack of statistics.

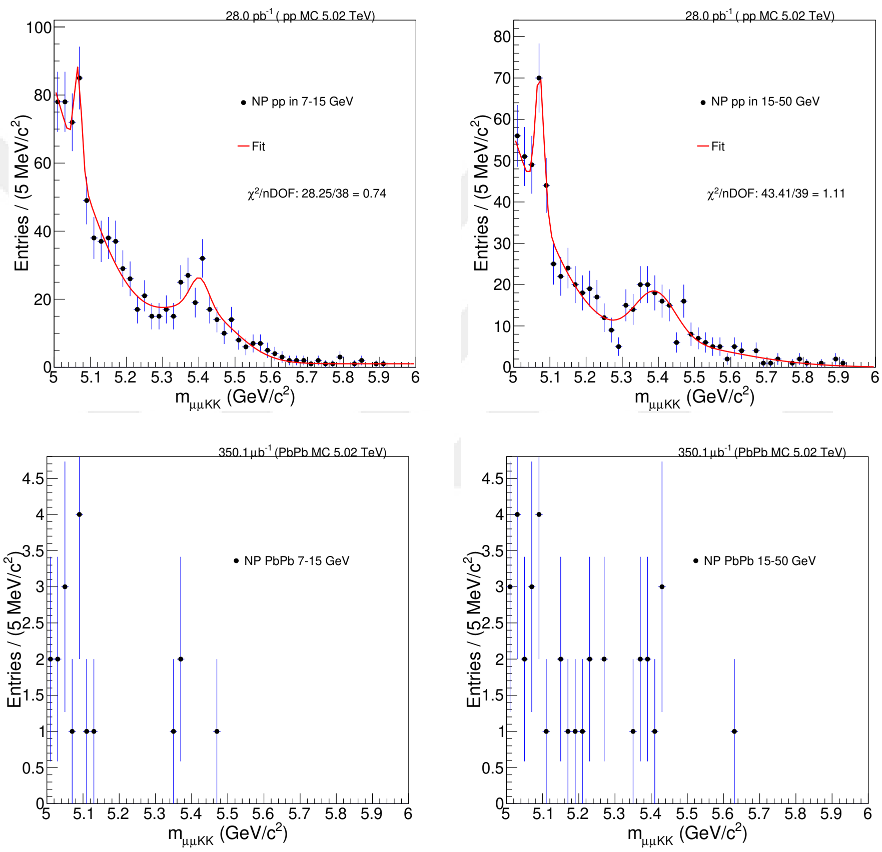

Figure 4.44. Fitting on NP background on pp and PbPb. Upper plots shows the fit results for 7 to 15 GeV/c (right) and 15 to 50 GeV/c (left) for pp samples. Lower plots for PbPb samples without fitting.

4.15. Track p_T Preselection Study

In this section, we investigate the different choice of the track p_T preselection performance. Recall that before the BDT training we applied the preselection cuts on track p_T which is 0.5 GeV for pp and 0.8 GeV for PbPb analysis. The results between applying different track p_T preselections are compared and BDT training performed again. The mass spectra corrected yields are obtained same as this analysis framework. The resulting mass spectra for pp data with applying various track p_T preselection of 0.5 which is nominal value, 0.6 , 0.7, 0.8, 0.9, 1.0 and 1.1 GeV are shown in Figure 4.45. and Figure 4.46.. In terms of PbPb data, the resulting mass spectra with track p_T preselection of 0.8 which is nominal value, 0.9,1.0, 1.1, 1.2, 1.3 and 1.4 GeV are represented in Figure 4.47. and Figure 4.48..

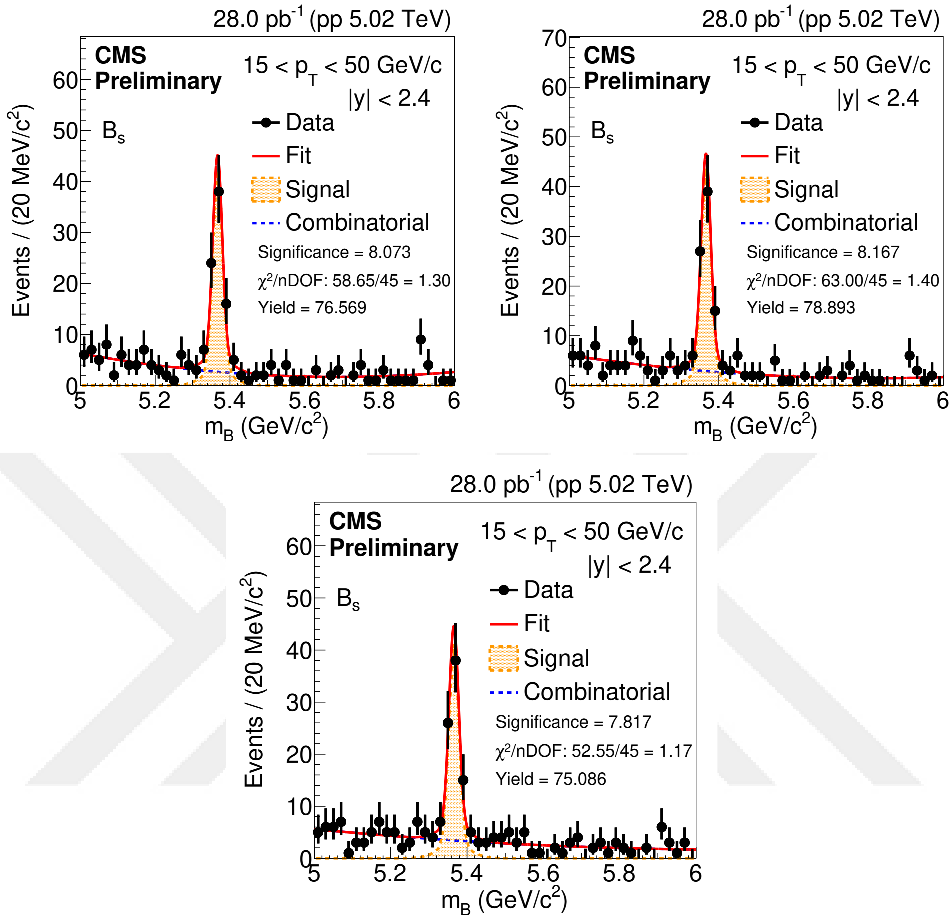

Figure 4.45. The resulting mass spectra with applying different track p_T preselection 0.5, 0.6, and 0.7 GeV/c in pp data.

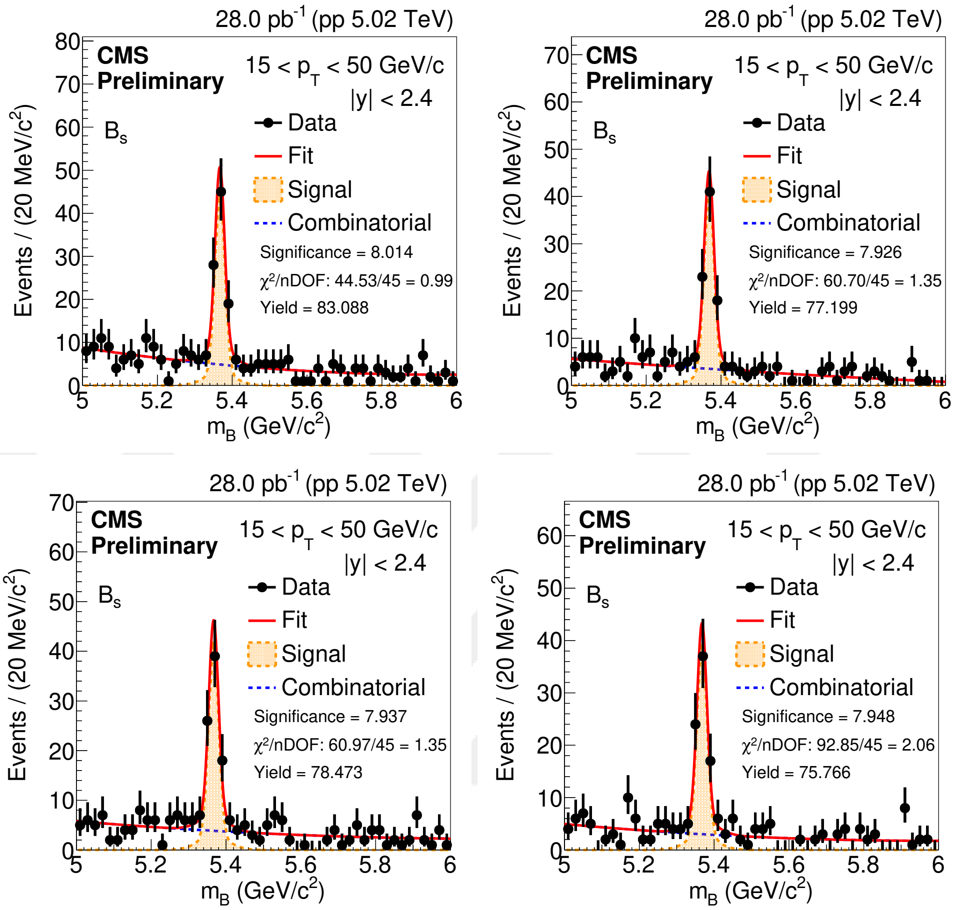

Figure 4.46. The resulting mass spectra with applying different track p_T preselection 0.8, 0.9, 1.0, and 1.1 GeV/c in pp data

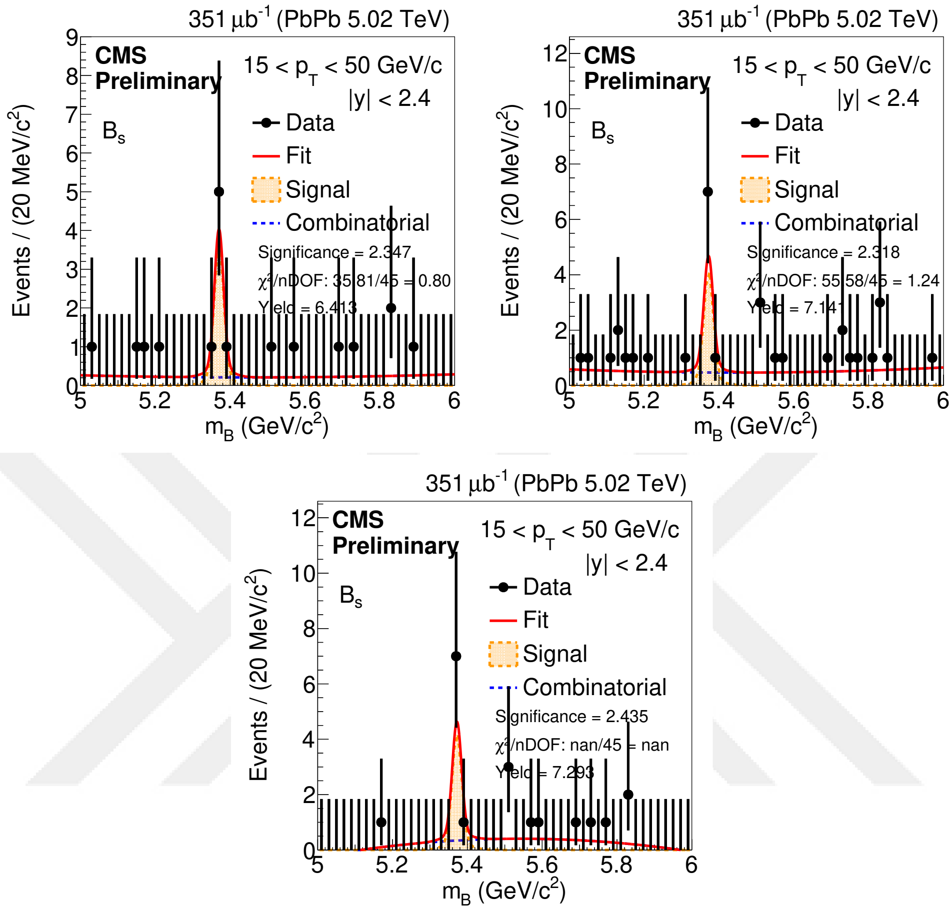

Figure 4.47. The resulting mass spectra with applying different track p_T preselection 0.8, 0.9, and 1.0 GeV/c in PbPb data

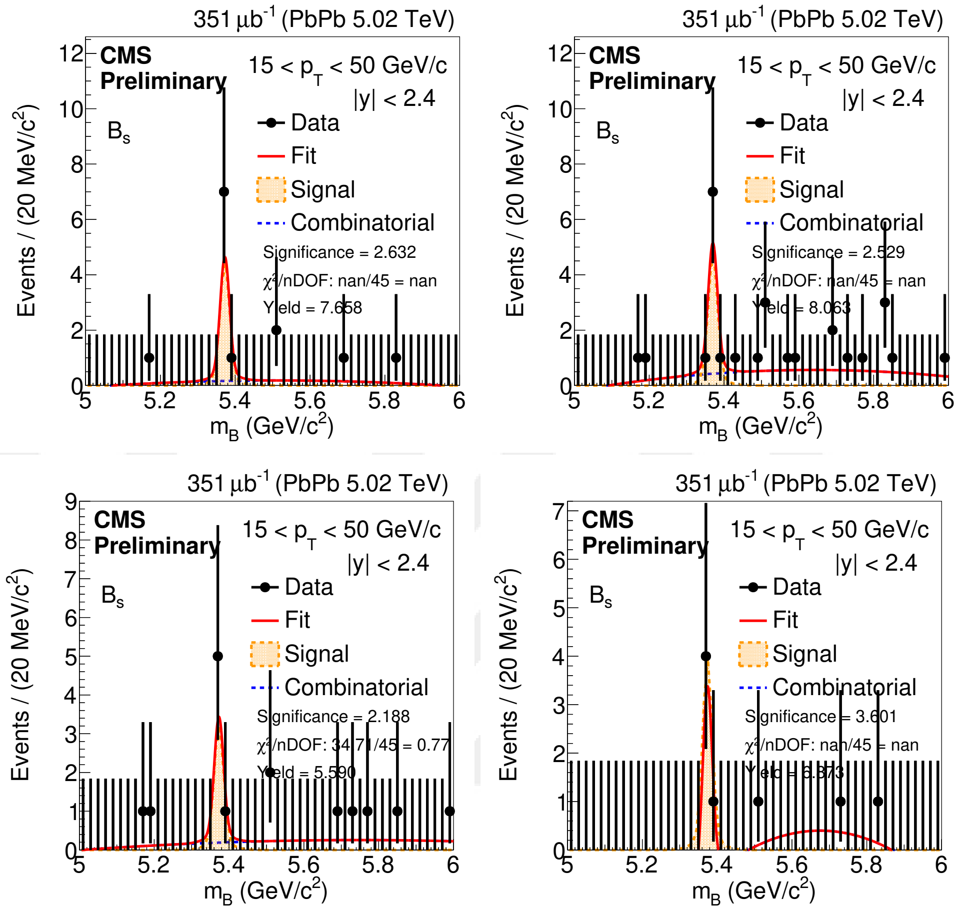

Figure 4.48. The resulting mass spectra with applying different track p_T preselection 1.1, 1.2, 1.3, and 1.4 GeV/c in PbPb data

Following that the corrected extracted yield between the track p_T preselection variation and analysis nominal values are compared by calculating the differences in percentage. Figure 4.49. shows the comparison results for both pp and PbPb.

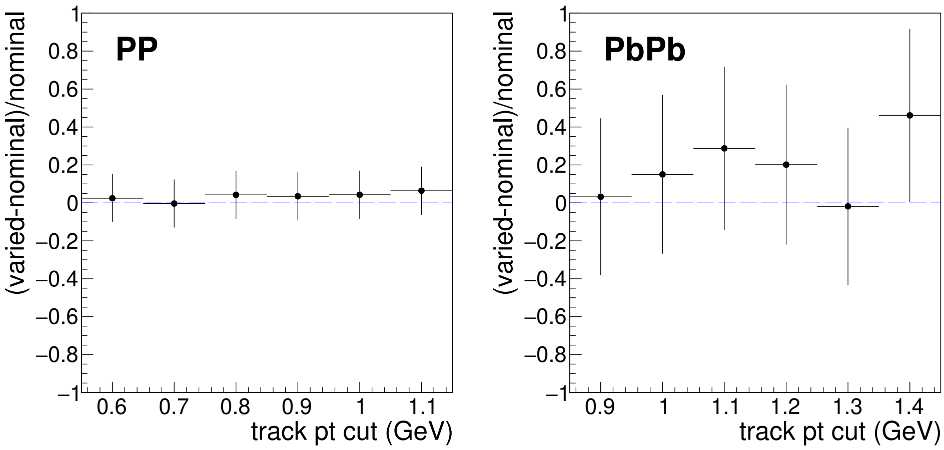

Figure 4.49. The comparison of the corrected extracted yield between and various the track p_T pre-selections variation and analysis nominal values for pp (left) and PbPb (right) are shown.

The error bar shown in the figures related with only statistical error of nominal fit. The statistical error corresponding to the nominal spectrum and varied spectrum are totally correlated. Note that the extracted yields results are with the statistical error and not represented with a specific trend of deviation from the zero for pp and PbPb analysis.

4.16. Prompt J/ψ Background

The prompt $Jpsi$ mesons produced directly in the proton-proton collision or indirectly via the decay of heavier charmonium states. These propmpt $Jpsi$ mesons also are potential background feed-down in the B_s^0 invariant mass spectrum. In order to define these background the B_s^0 mass spectra are performed with using prompt J/ψ MC samples with different BDT cut value for PbPb B_s^0 p_T interval 7 to 15 and 15 to 50 GeV/c. The figures in Appendix F represents the resulting B_s^0 mass spectra using prompt J/ψ PbPb MC samples with different BDT cut value for various $J\psi$ p_T interval, 0 to 3, 3 to 6, 6 to 9, 9 to 12, 12 to 15 , 15 to 30 and 30 to infinite.

4.17. Selection efficiency: cut value variation

In this section, the previous method for evaluating the systematic uncertainty related with cut selection is documented. The cut variable distributions of B_s^0 signal in data are not in a good agreement with MC simulation. This causes a bias in the efficiency estimation and therefore in the cross section measurement. In order to evaluate the systematic uncertainty associated with this, the following double ratio formula is used.

$$Ratio(Data/MC)(i) = \frac{\varepsilon_i^{Data}}{\varepsilon_i^{MC}} = \frac{\frac{Yield^i_{Data}(cut\ default)}{Yield^i_{Data}(cut\ varied)}}{\frac{Yield^i_{MC}(cut\ default)}{Yield^i_{MC}(cut\ varied)}} \tag{4.10}$$

where, ε_i^{Data} and ε_i^{MC} is the selection efficiency for data and MC samples, respectively. The ”default” denotes the yields derived from the nominal cut value of a given cut variable ”i” whereas ”varied” refers to the yields extracted with a varied cut value. As is the case with the main analysis workflow, the yields obtained by fitting procedure. The evaluation of the associated selection efficiency ε for each cut variable ”i” for data and MC samples is estimated by taking into consideration the ratio of the yields derived from a varied cut value with respect to the default value. In case of obtaining no distinction between the data and MC efficiencies, the ratio is expect to be equal to one. Hence, the systematic uncertainty associated to each selection is considered as the difference of the $Ratio(Data/MC)(i)$ with respect to unity. The systematic uncertainty is propagated as the maximum difference between unity among the examined cut values. The various BDT cut values from 0.18 to 0.22 and o.28 to 0.32 for pp and PbPb and additionally the nominal cut values 0.21 for pp and 0.30 for PbPb are studied. In Appendix G, the resulting double ratio of the cut variation with respect to the BDT discriminant for pp and PbPb data and MC are represented in Figure G1. and Figure G2.. Due to determination of the double ratio includes to mass spectrum fitting, the obtained value is affected by the statistic available in data. The extracted yields in MC drop by 3.2% and 5.7% when the BDT cut value altered from 0.304 to 0.316 and 0.32. However, the extracted yields in data decrease from 9 to 7 and 6 which are 22% and 33%. The resulting B_s^0 mass spectrum derived from different BDT cut values for PbPb MC and data are represented in Figure 4.50..

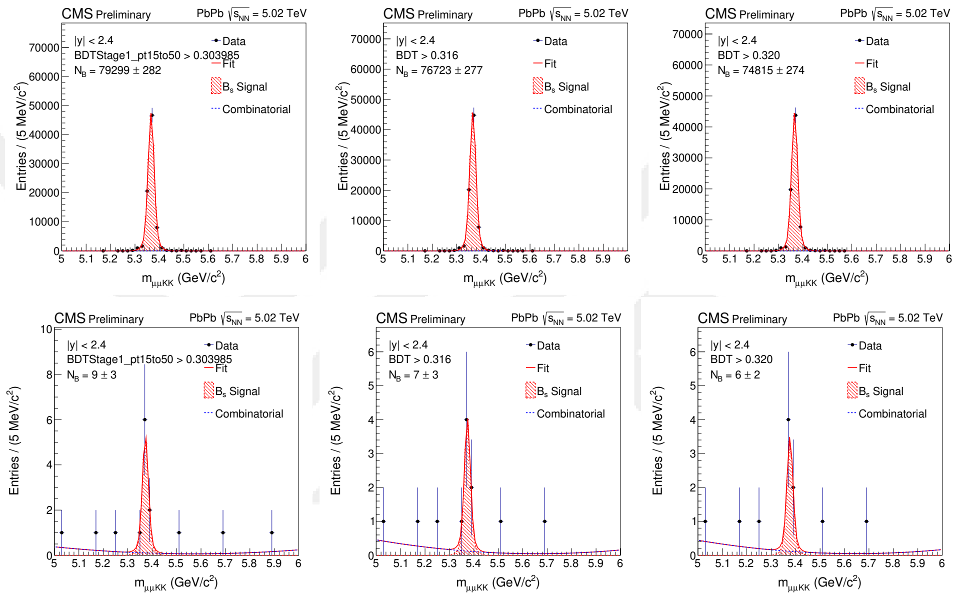

Figure 4.50. Scanning of BDT cut value and the resulting mass spectrum fitting for PbPb MC and data. Different BDT cut varied from 0.304, 0.316 and 0.32 are used for MC (top row) and data (bottom row).

Consequently, the results are strongly correlated with the statistic available in data. The B_s^0 mass spectrum with the other BDT cut value variation is represented in the Section 4.18.. The systematic uncertainty associated with this variable is estimated as the maximum difference across the the points in the double ratio plot. The resulting number of systematic uncertainty is derived 5.5% for pp and 30.4% for PbPb and the values are documented in Table 4.25..

Table 4.25. Systematic uncertainties associated with BDT cut variation.

Cut/Max diff.	BDT cut variation
pp	5.5%
PbPb	30.4%

4.18. Mass fitting spectrum for BDT cut variations

In this section we studied all the resulting B_s^0 mass spectra extracted from different BDT cut variation study which is the previous method we used for evaluate the systematic uncertainty associated with cut selection. The following plots represents the mass spectrum fitting with different BDT cut values for both pp and PbPb data. For pp MC (G3.) and PbPb MC (G4.) results are shown in Appendix G.

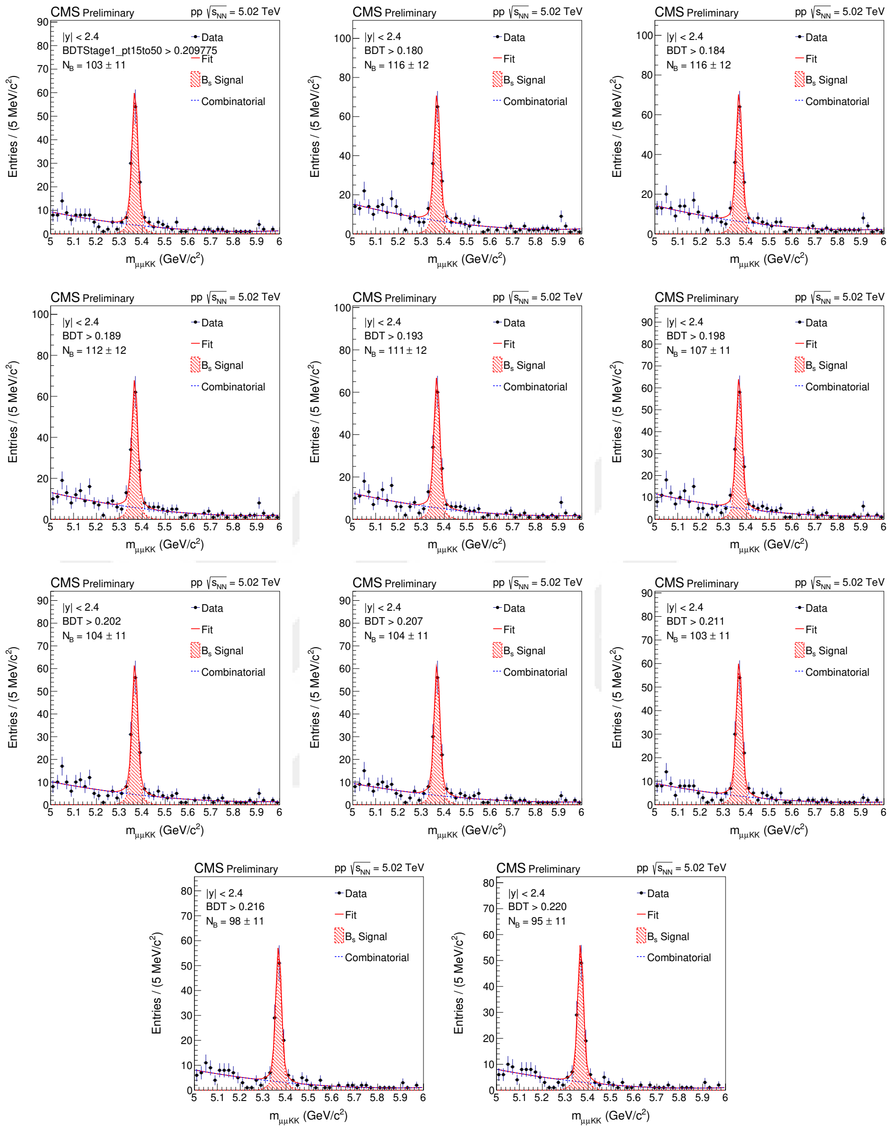

Figure 4.51. Scanning of BDT cut value and the summary plots of mass spectrum with fitting for pp data.The 1st spectrum on the top left is obtained at nominal analysis value BDT = 0.21. The following spectras have the BDT cut value varied from 0.18 increasingly to 0.22.

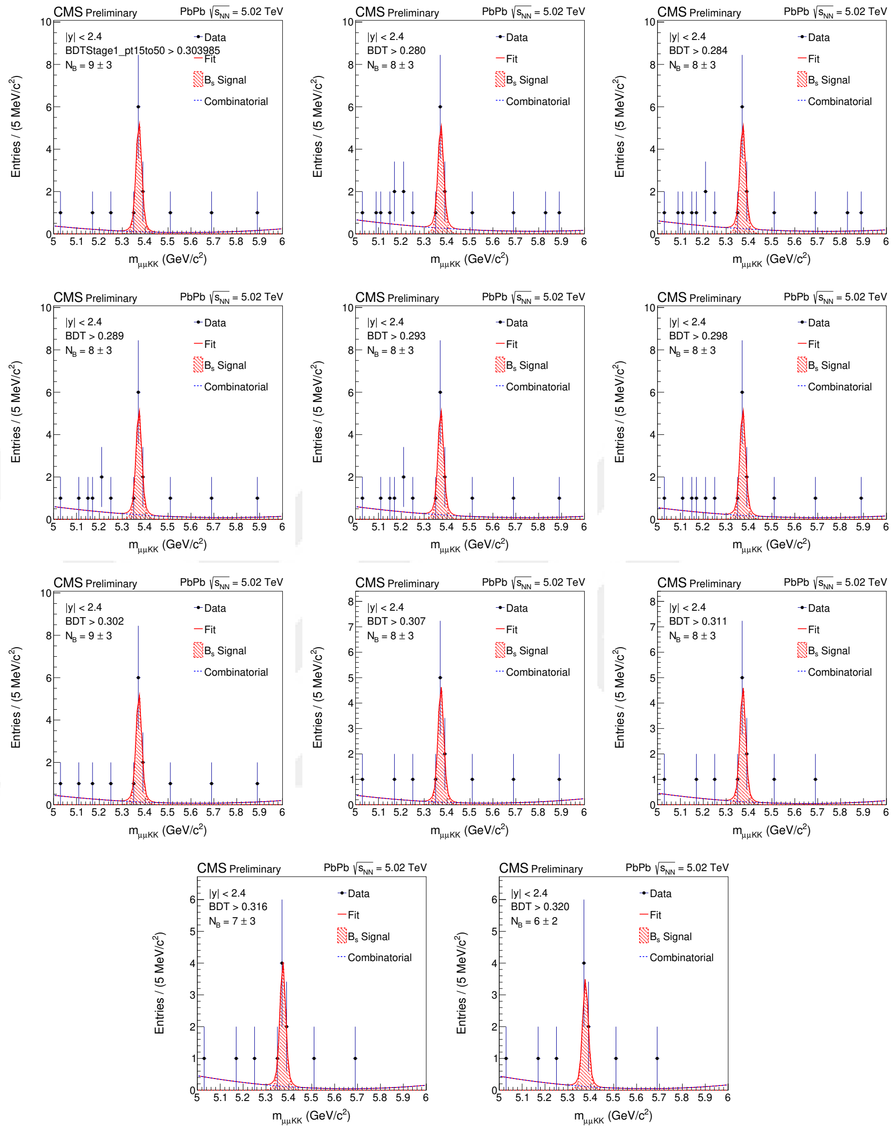

Figure 4.52. Scanning of BDT cut value and the summary plots of resulting mass spectrum fitting for PbPb data. The 1st spectrum on the top left is obtained with using nominal analysis value BDT = 0.30. The following spectra have the BDT cut value varied from 0.28 increasly to 0.32.

5. CONCLUSION

The first measurement of the differential production cross section of B_s^0 mesons has been done in pp and PbPb collisions at the center of mass energy $\sqrt{s_{NN}}$ = 5.02 TeV with the CMS detector at the LHC.

The B_s^0 differential cross sections $d\sigma/dp_T^B$ in the exclusive hadronic decay channel $B_s^0 \to J/\psi\,\phi \to mu^+mu^-\;K^+K^-$ is calculated in the kinematic range $|y| < 2.4$ and transverse momentum p_T range between 7 to 50 GeV/c for pp and PbPb collisions events. The results are summarized in Fig. 4.20. and Fig. 4.21. for both integrated 2-bin and 3-bin p_T ranges, respectively. The scaled PbPb cross section is calculated according to equation 4.8.

Furthermore, the results are compared to the predictions of fixed-order plus next-to-leading logarithm (FONLL) calculations and indicate that the CMS results for B_s^0 meson cross section consistent with the FONLL theoretical prediction. The nuclear modification factors evaluated using FONLL calculations as pp reference, are found to be consistent with unity within the quoted statistical and systematical uncertainties. The ratio of the nuclear modification factor between B_s^0 R_{AA} which is calculated in section 4.11.1. and B^+ R_{AA} is also calculated and represented in analysis (CMS Collaboration, 2017b). An indication of an enhancement of the B_s^0/B^+ ratio in PbPb with respect to the pp collisions is observed as expected in the case of a strong contribution of beauty recombination in heavy ion collisions. This analysis demonstrates the capability of performing fully reconstructed B_s^0 measurement in PbPb collisions with the CMS detector.

REFERENCES

Aad, Georges et al. (2012). “Observation of a new particle in the search for the Standard Model Higgs boson with the ATLAS detector at the LHC”. In: *Phys.Lett.B* (B716). doi: `doi:10.1016/j.physletb.2012.08.020`.

— (2015). “Combined Measurement of the Higgs Boson Mass in pp Collisions at $\sqrt{s}$ = 7 and 8 TeV with the ATLAS and CMS Experiments”. In: *Phys.Rev.Lett* (114). doi: `doi:10.1103/PhysRevLett.114.191803`.

Alice Collaboration (2008). “The ALICE experiment at the CERN LHC”. In:

Antcheva (2009). “ROOT – A C++ framework for petabyte data storage, statistical analysis and visualization”. In: *Comput. Phys. Commun.* (180:2499).

Atlas Collaboration (2008). “The ATLAS Experiment at the CERN Large Hadron Collider”. In:

— (2016). “Search for Minimal Supersymmetric Standard Model Higgs bosons H/A and for a Z' boson in the $\tau\tau$ final state produced in pp collisions at $\sqrt{s}$ =13 TeV with the ATLAS Detector”. url: `https://arxiv.org/abs/1608.00890`.

Baker and Cousins (1984). “Clarification of the use of chi-square and likelihood functions in fits to histograms”. In: url: `http://dx.doi.org/https://doi.org/10.1016/0167-5087(84)90016-4`.

Barberio, van Eijk and Was (1991). “PHOTOS: A Universal Monte Carlo for QED radiative corrections in decays”. In: doi: `doi:10.1016/0010-4655(91)90012-A`.

Bruning (2004). “LHC Design Report”. In:

Cacciari Greco, Nason (1998). “The p_T spectrum in heavy-flavour hadroproduction”. In: url: `http://arxiv.org/abs/hep-ph/9803400`.

Cerizza, G. (2012). “Measurements of Production and Decay Properties of Bs Mesons Decaying into J/Psi Phi with the CMS Detector at the LHC”. In: *CMS-TS-2012-018*.

Chanel, Michel (2002). “LEIR: The Low Energy Ion Ring At Cern”. In: url: `http://accelconf.web.cern.ch/accelconf/e02/papers/thple074.pdf`.

Chartchyan (2010). “Alignment of the CMS Silicon Tracker during Commissioning with Cosmic Rays”. In: *JINST*. doi: `doi:10.1088/1748-0221/5/03/T03009`.

Chartchyan et al. (2012). “Observation of a new boson at a mass of 125 GeV with the CMS experiment at the LHC”. In: *Phys.Rev.Lett* (B716). doi: `doi:10.1016/j.physletb.2012.08.021`.

Chartchyan and other (2014). “Description and performance of track and primary-vertex reconstruction with the CMS tracker”. In:

CMS Collaboration (1997). “The CMS Magnet Project Technical Design Report”. url: `https://cds.cern.ch/record/331056/files/Magnet%5C_TDR%5C_complete.pdf`.

— (1998). “The CMS Tracker Technical Design Report”. In: url: `http://weblib.cern.ch/abstract?%20CERN-LHCC-98-6`.

— (2010). “CMS Luminosity Public Results”. url: `http://ippog.web.cern.ch/sites/ippog.web.cern.ch/files/import/cms3d%5C_black%5C_detector%5C_colouredlabels%5C_jul10.pdf`.

— (2013). “CMS reconstruction improvement for the muon tracking by the RPC chambers”. In: *JINST*. doi: `doi:10.1088/1748-0221/8/03/T03001`.

— (2016a). “D0 meson nuclear modification factor in PbPb collisions at 5.02 TeV”. In: url: `http://cds.cern.ch/record/2157844`.

CMS Collaboration (2016b). “Measurement of the charged particle nuclear modification factor in PbPb collisions at $\sqrt{s}$= 5.02 TeV”. In: *Technical Report CMS-PAS-HIN-15-015*.

— (2016c). “Searches for invisible decays of the Higgs boson in pp collisions at $\sqrt{s}$ = 7, 8, and 13 TeV”. url: `https://arxiv.org/abs/1610.09218`.

— (2017a). “Clarification of the use of chi-square and likelihood functions in fits to histograms”. In: url: `http://www.lpthe.jussieu.fr/~cacciari/fonll/fonllform.html`.

— (2017b). “Measurement of the B± Meson Nuclear Modification Factor in Pb-Pb Collisions at √sNN = 5.02 TeV”. In: doi: `doi:10.1103/PhysRevLett.119.152301.`.

CMS Collabration (2008). “The CMS experiment at the CERN LHC”. In:

CMS Heavy Ion Group (2016a). “Charmonia in 5.02 tev data”. In: url: `http://cms.cern.ch/iCMS/jsp/db_notes/noteInfo.jsp?cmsnoteid=CMS%20AN-2016/067`.

— (2016b). “Dimuon performance studies in 2015 5.02tev pp and pbpb data”. In: url: `http://cms.cern.ch/iCMS/jsp/db_notes/noteInfo.jsp?cmsnoteid=CMS`.

Dogra, Sunil et al. (2017). “Centrality and event plane reconstruction for pbpb collisions at 5 tev in 2015”. In: url: `http://cms.cern.ch/iCMS/user/noteinfo?cmsnoteid=CMS`.

Dokshitzer, Y. L. and D. E. Kharzeev (2001). “Heavy quark colorimetry of QCD matter”. In: *Phys.Rev.Lett* (B519). doi: `doi:10.1016/S0370-2693(01)01130-3`.

Evans, Lyndon and Philip Bryant (2008). “LHC Machine”. In:

Field (2010). “Early LHC Underlying Event Data Findings and Surprises”. In: url: http://inspirehep.net/record/873443/files/arXiv:1010.3558.pdf.

Florian, Sheck (2012). “”Electroweak and Strong Interactions. Phenomenology, Concepts, Models””. url: ftp://nozdr.ru/biblio/kolxo3/P/PG/Scheck/Scheck%20F.%20Electroweak%20and%20strong%20interactions..%20phenomenology,%20concepts,%20models%20(3ed.,%20Springer,%202011)(ISBN%209783642202407)(O)(442s)_PG_.pdf.

Group, CMS Heavy Ion (2016). “Dimuon performance studies in 2015 5.02tev pp and pbpb data”. In: url: https://cds.cern.ch/collection/CMS%20Analysis%20Notes.

Group, Particle Data (2014). “Review of particle physics”. In: doi: doi:10.1088/1674-1137/38/9/090001.

Haffner, Julie (2013). “The CERN accelerator complex. Complexe des accelerateurs du CERN”. url: https://cds.cern.ch/record/2197559?ln=en.

Heavy Ion Group (2016). “Dimuon performance studies in 2015 5.02TeV pp and PbPb Data”. In:

Hoecker, Adrian et al. (2016). “TMVA: Toolkit for Multivariate Data Analysis”. In: url: http://www.arXiv.org/abs/physics/0703039.

Karimaki (1997). “The CMS tracker system project: Technical Design Report”. In:

LHC (1995). “The Large Hadron Collider Conceptual Design.” In:

LHCb Collaboration (2008). “The LHCb Detector at the LHC”. In:

Lokhtin and Snigirev (2006). “A model of jet quenching in ultrarelativistic heavy ion collisions and high-pT hadron spectra at RHIC”. In: doi: doi:10.1140/epjc/s2005-02426-3.

Lujan, Paul (2018). “CMS Luminosity Public Results”. url: https://twiki.cern.ch/twiki/bin/view/CMSPublic/LumiPublicResults.

Statistic Committee (2018). “CMS Statistics Committee Recommendations”. url: https://twiki.cern.ch/twiki/bin/viewauth/CMS/StatComGOF.

Tronc (2002). “LINAC ACCELERATING STRUCTURES”. In: url: http://accelconf.web.cern.ch/AccelConf/e94/PDF/EPAC1994_2164.PDF.

Turner, M. (1998). “Cosmology solved? Quite possibly!” In: doi: doi:10.1086/316325.

Wiki (2018). “Standard Model of Elementary Particles”. url: https://commons.wikimedia.org/wiki/File:Standard%5C_Model%5C_of%5C_Elementary%5C_Particles.svg.

Wikimedia (2018). “B mesons”. url: https://en.wikipedia.org/wiki/B_meson.

Xabier Cid Vidal, Ramon Cid Manzano (2018). “Momentum”. url: https://www.lhc-closer.es/taking_a_closer_look_at_lhc/0.momentum.

CURRICULUM VITAE

She completed her bachelor and Master degree in Physics at Kahraman Maraş Sütcü Imam University, Kahraman Maras, Turrkey. After graduation from Msc. she started PhD degree at Çukurova University, Adana, Turkey. The kind of PhD project she chose offered her the possibility to work in the lab and test one of the parts to be installed on the CMS detector. Since the beginning of her PhD studies at CERN, she was heavily involved in operations, the Phase-I Upgrade of the HCAL, and also installation, testing and commissioning of the HF and HB calorimeters. Besides, she was selected one of the supporting scientists for Beam Line for Schools at CERN. Her responsibilities were to work on preparing the experimental environment for the students and implementing the experiments that were proposed by the teams. Additionally to her experience with the HCAL and BL4S, she was heavily involved in the analysis of the B_s^0 and B^+ mesons differential production cross sections in pp and PbPb collisions at $\sqrt{s}$=5.02 TeV in CMS.

APPENDIX

A Correlation variables for MVA

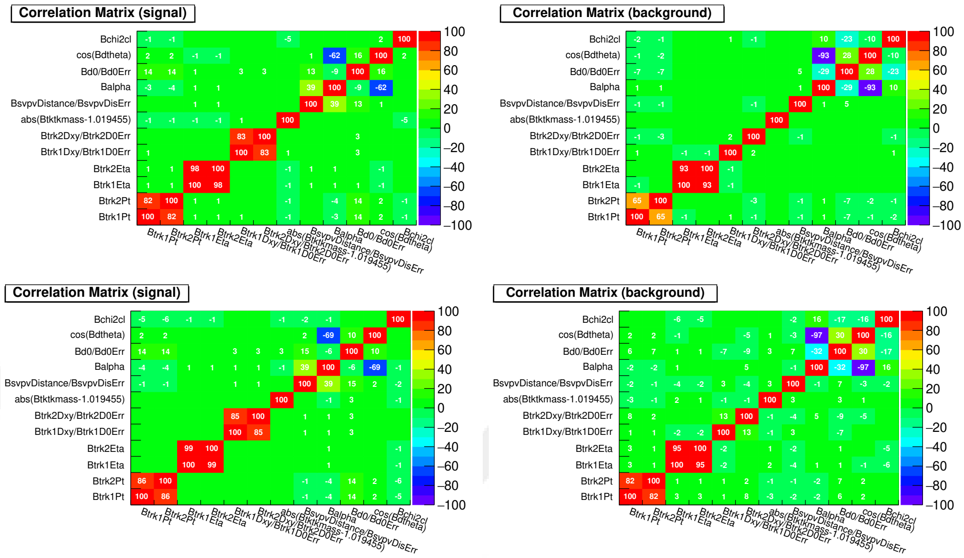

Figure A1. Correlation matrix between the variables used in MVA training for signal and background in pp analysis. First two panel is related to B_s^0 p_T 7 to 15 GeV/c and last two is for B_s^0 p_T 15 to 50 GeV/c.

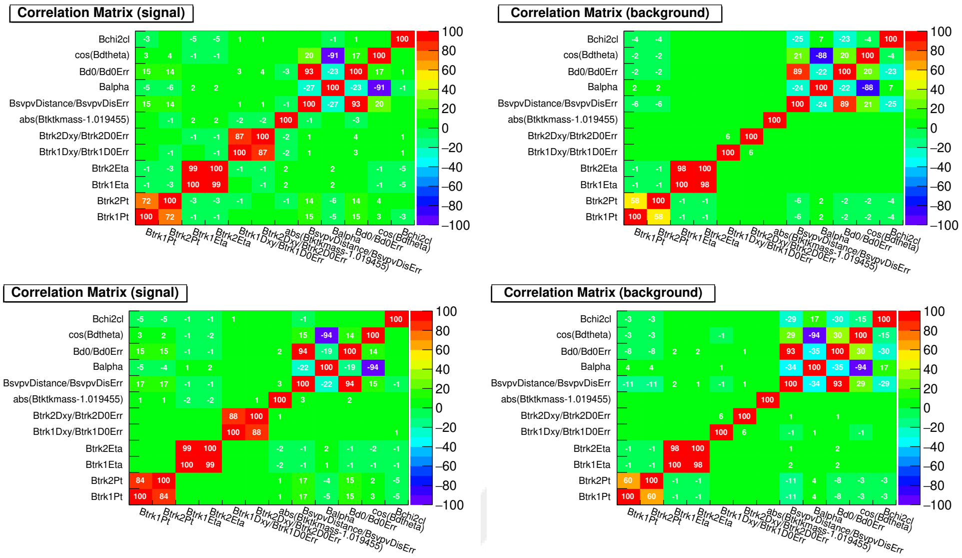

Figure A2. Correlation matrix between the variables used in MVA training for signal and background in PbPb analysis. First two panel is related to B_s^0 p_T 7 to 15 GeV/c and last two is for B_s^0 p_T 15 to 50 GeV/c.

B Distribution of the input variables for MVA

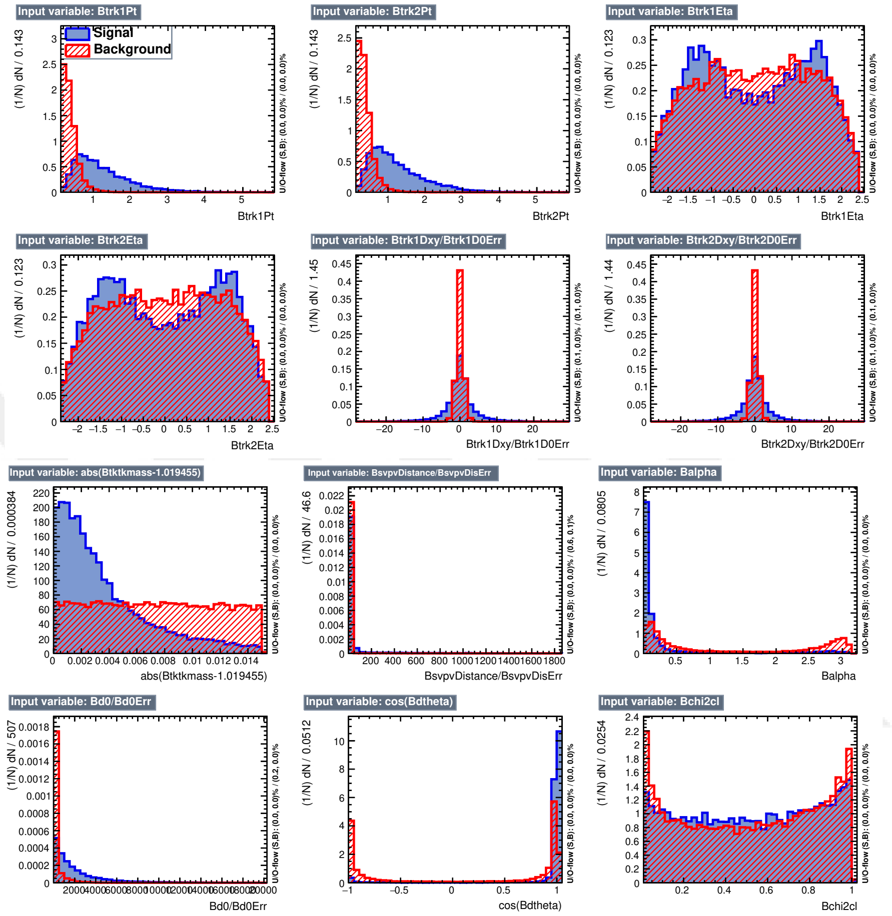

Figure B1. Input variables distributions for training used in pp for B_s^0 p_T 7 to 15 GeV/c.

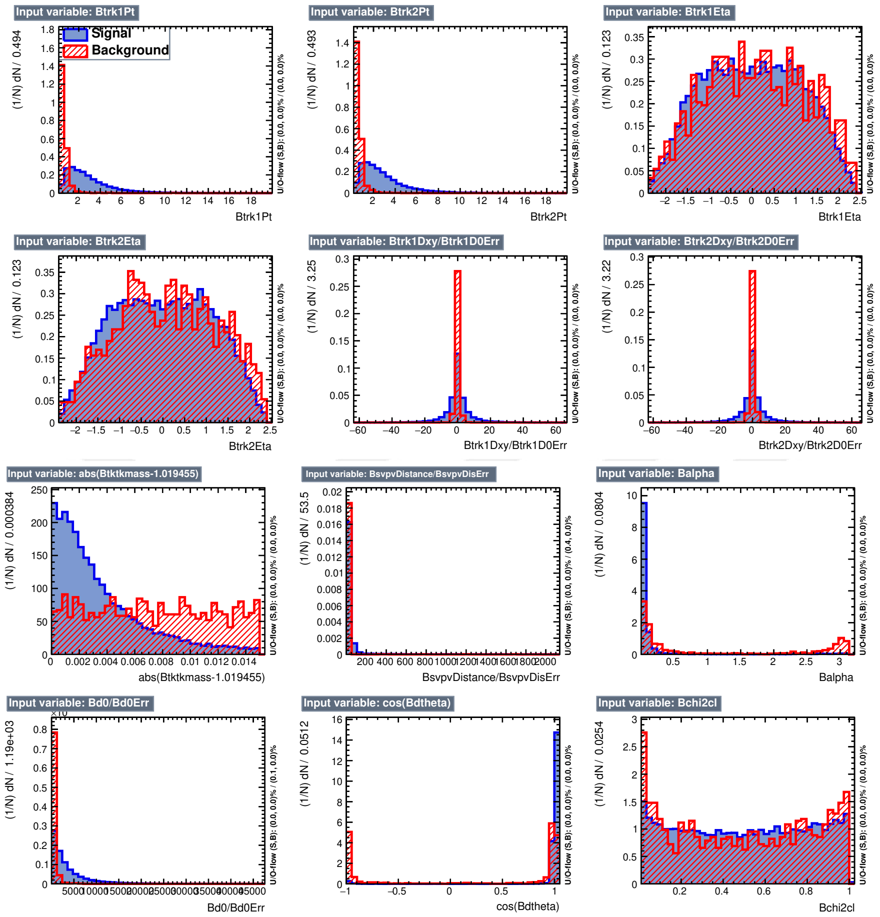

Figure B2. Input variables distributions for training used in pp for B_s^0 p_T 15-50 GeV/c.

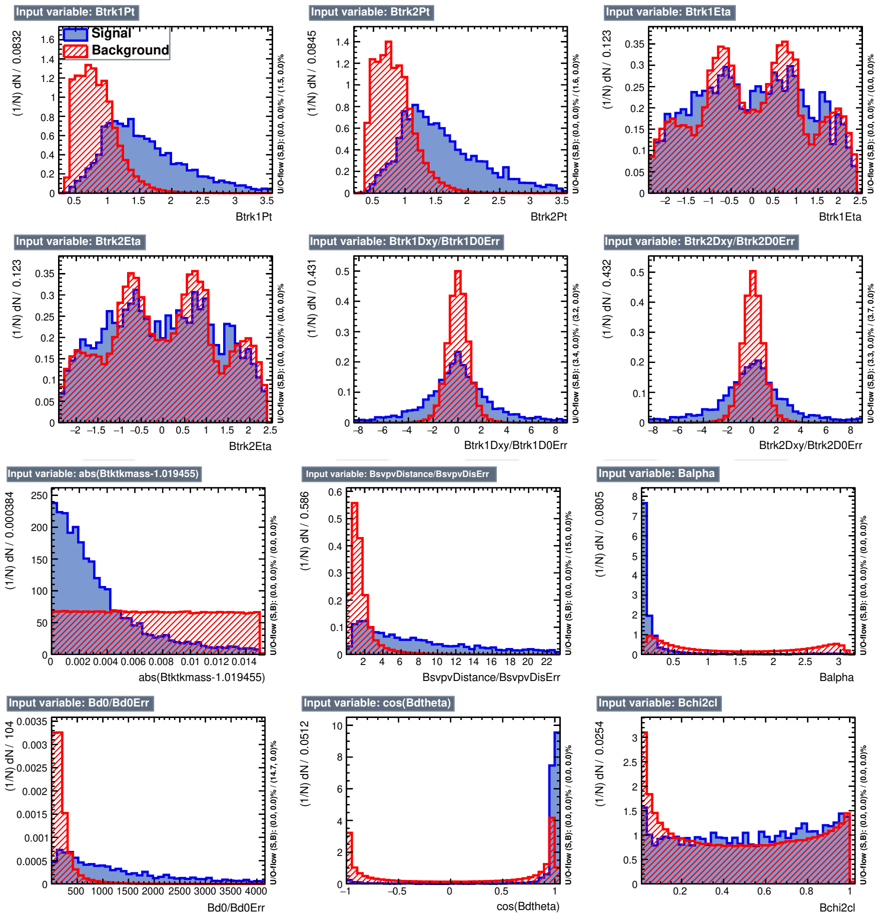

Figure B3. Input variables distributions for training used in PbPb for B_s^0 p_T 7 to 15 GeV/c.

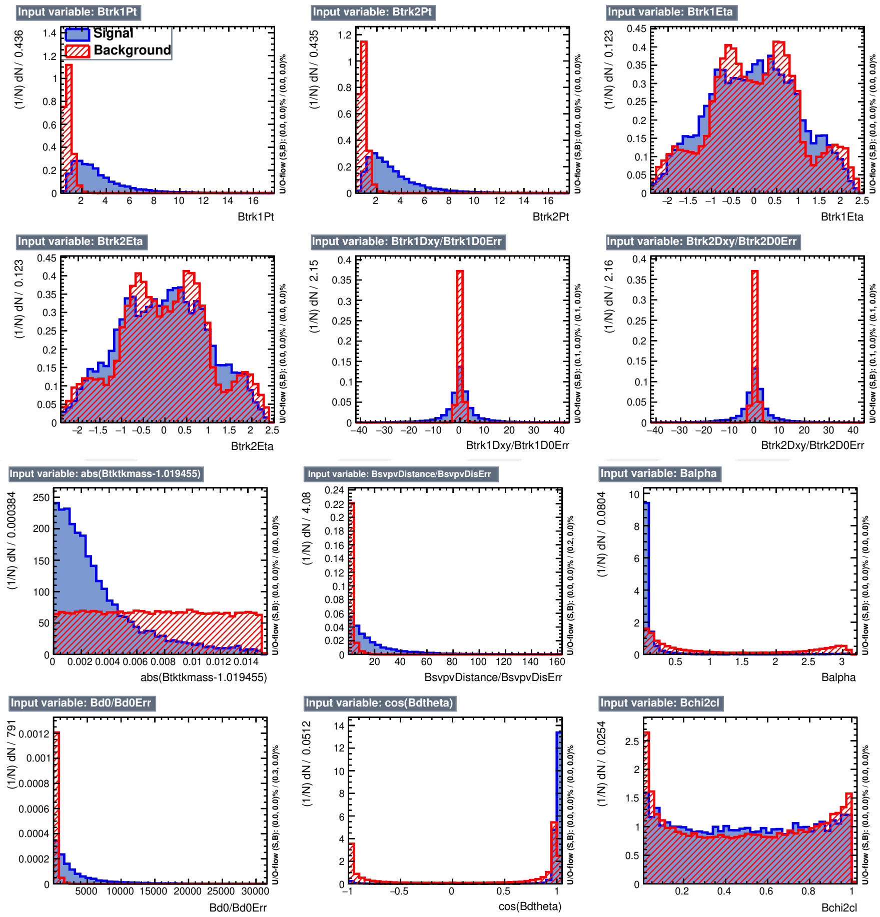

Figure B4. Input variables distributions for training used in PbPb for B_s^0 p_T 15-50 GeV/c.

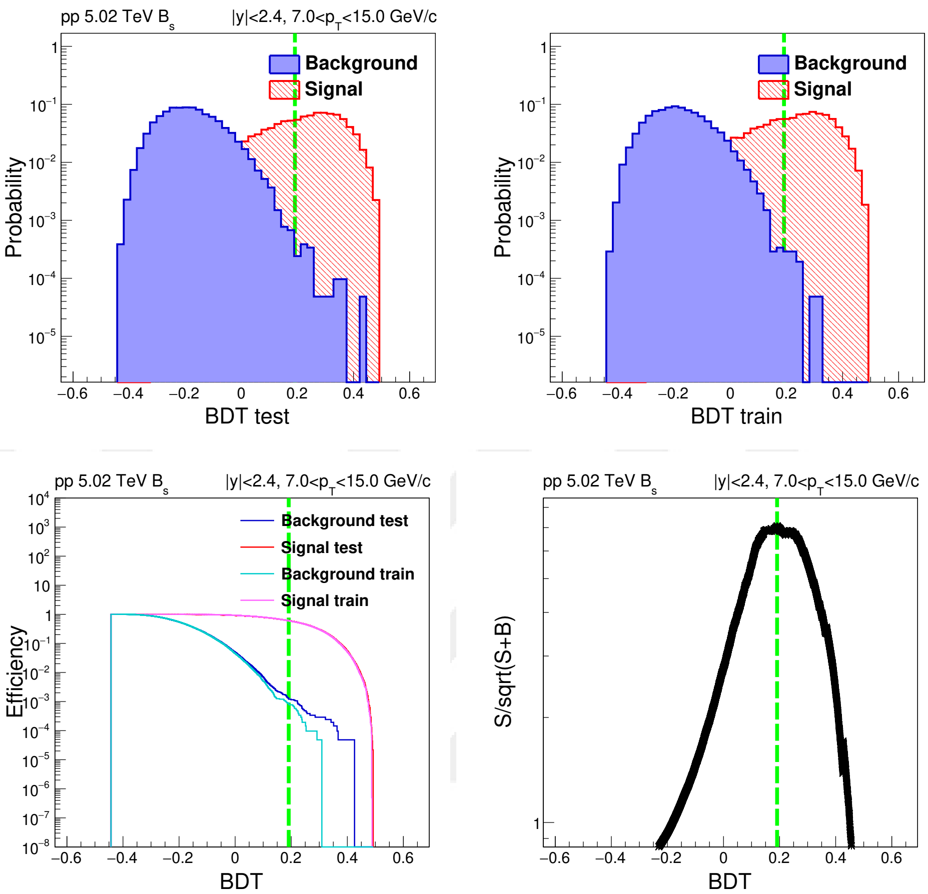

Figure B5. The upper plots show the BDT distribution of signal and background from testing and training samples. The lower left represents the efficiency as a function of BDT for training and testing samples. The lower right shows the significance $S/\sqrt{S+B}$ as a function of BDT for 7-15 GeV/c in pp collision data. The optimal BDT cut value used in the analysis is indicated with green dash line.

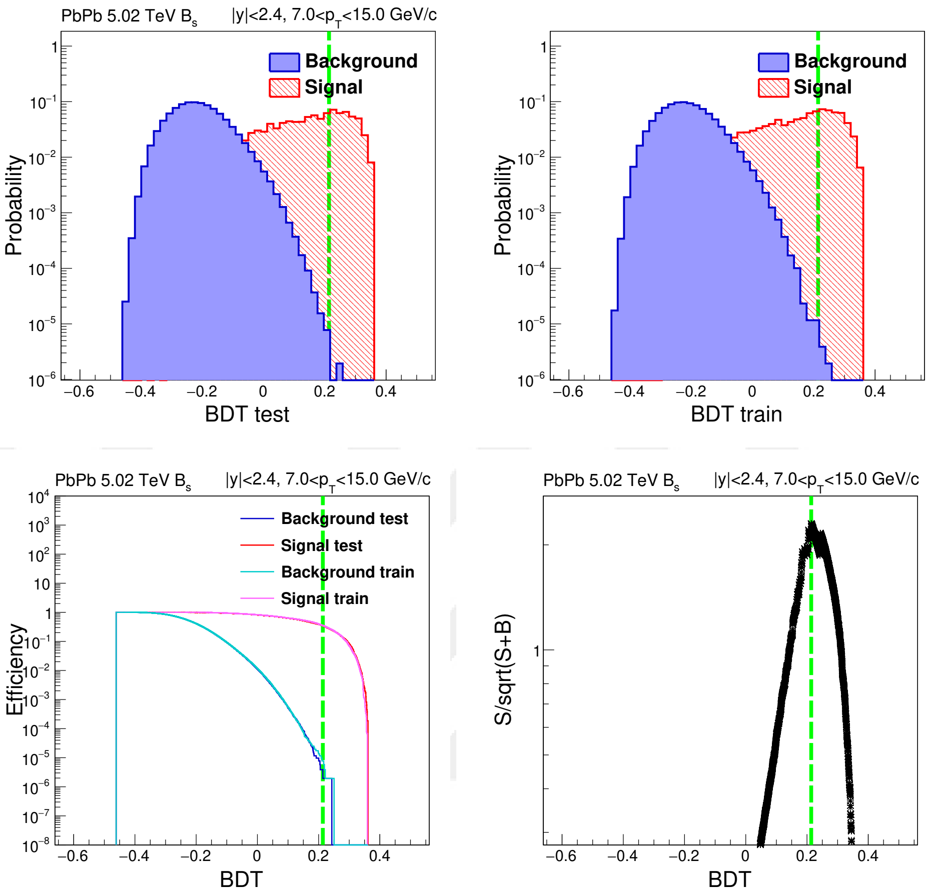

Figure B6. The upper plots show the BDT distribution of signal and background from testing and training samples. The lower left represents the efficiency as a function of BDT for training and testing samples. The lower right shows the significance $S/\sqrt{S+B}$ as a function of BDT for 7-15 GeV/c in PbPb collision data. The optimal BDT cut value used in the analysis is indicated with green dash line.

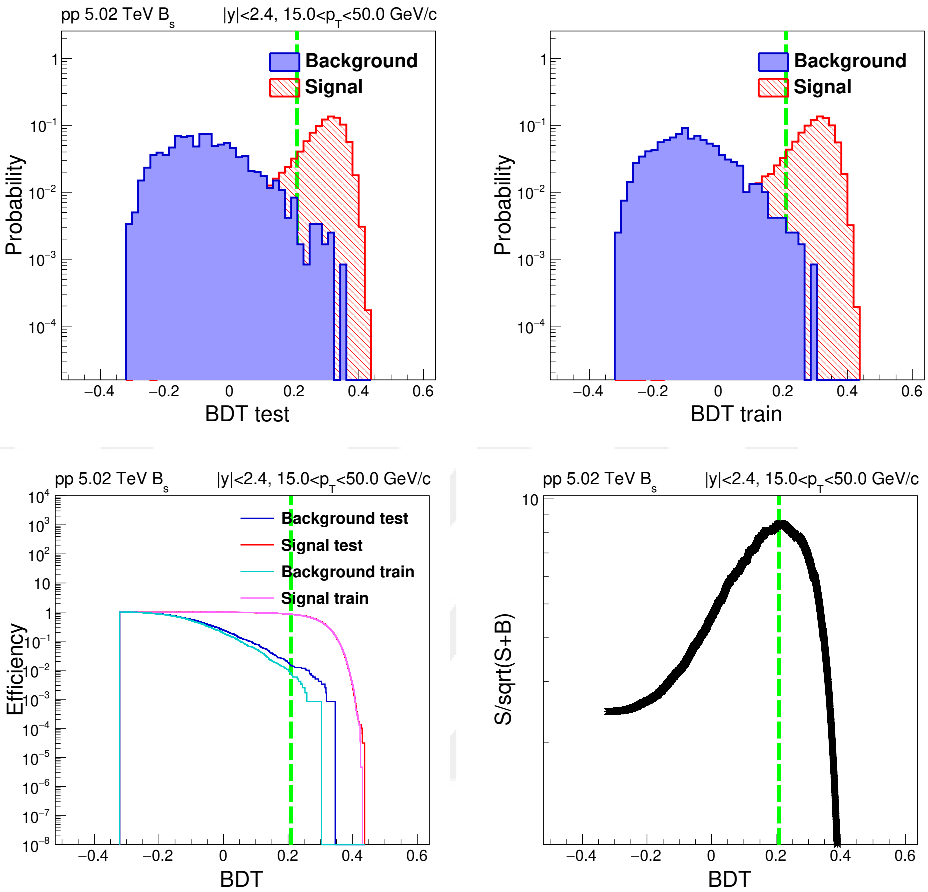

Figure B7. The upper plots show the BDT distribution of signal and background from testing and training samples. The lower left represents the efficiency as a function of BDT for training and testing samples. The lower right shows the significance $S/\sqrt{S+B}$ as a function of BDT for 15-50 GeV/c in pp collisions. The optimal BDT cut value used in the analysis is indicated with green dash line.

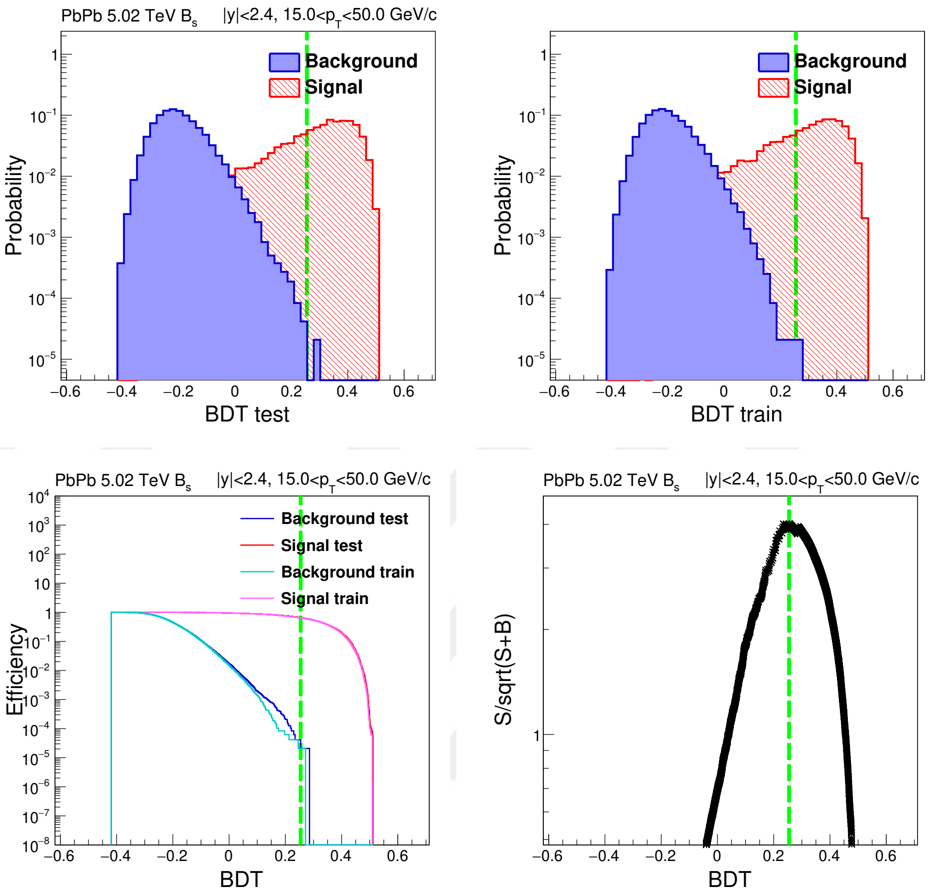

Figure B8. The upper left and right plots represent the BDT distribution of signal and background from testing and training samples. Efficiency as a function of BDT for training and testing samples distribution is presented in the lower left. While significance $S/\sqrt{S+B}$ as a function of BDT for 15-50 GeV/c in PbPb collisions is shown in the lower right. The green dash line indicates the optimal BDT cut value used in the analysis

C MC sample Mass spectrum with BDT

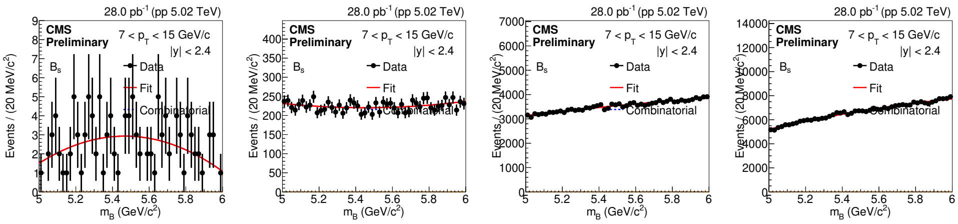

Figure C1. B_s^0 mass spectra using prompt J/ψ MC samples with various BDT cut value scan in pp B_s^0 p_T 7-15 GeV/c.

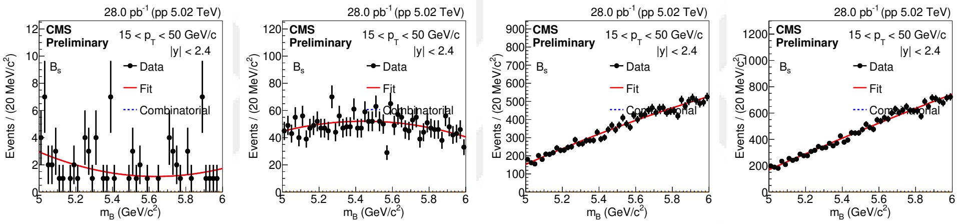

Figure C2. B_s^0 mass spectra using prompt J/ψ MC samples with various BDT cut value scan in pp B_s^0 p_T 15-50.

C1. PbPb samples

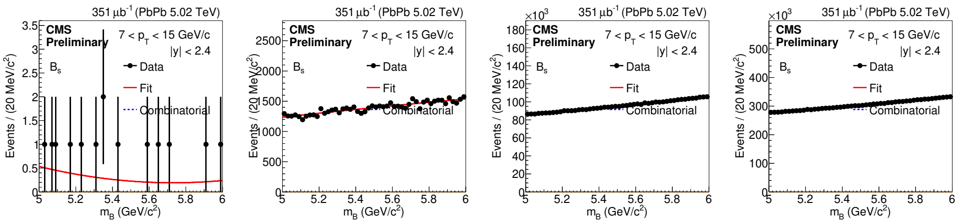

Figure C3. B_s^0 mass spectra by using prompt J/ψ MC samples with various BDT cut value scanned in PbPb B_s^0 p_T 7-15 GeV/c.

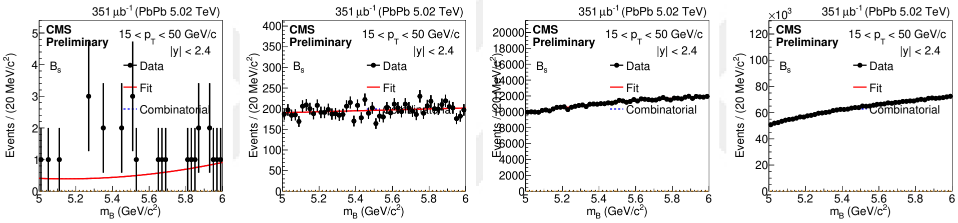

Figure C4. B_s^0 mass spectra by using prompt J/ψ MC samples with various BDT cut value scanned in PbPb B_s^0 p_T 15-50 GeV/c.

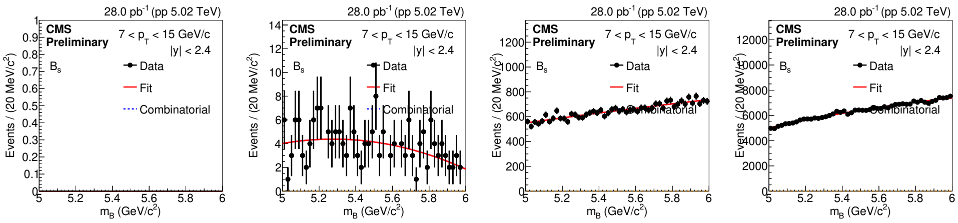

Figure C5. B_s^0 mass spectra by using prompt J/ψ MC samples with various BDT cut value scanned in pp B_s^0 p_T 7 to 15 GeV/c. The BDT discriminant used here is trained in PbPb

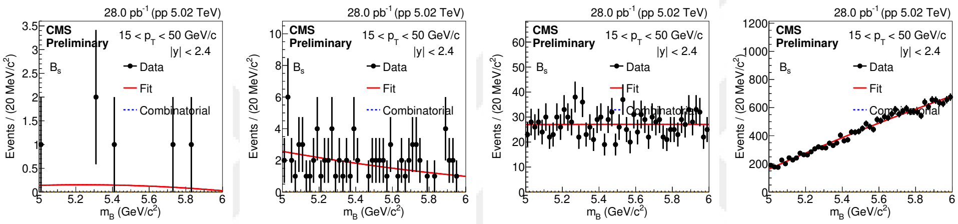

Figure C6. B_s^0 mass spectra by using prompt J/ψ MC samples with various BDT cut value scanned in pp B_s^0 p_T 15 to 50 GeV/c, The BDT discriminant used here is trained in PbPb

D MC and DATA comparison

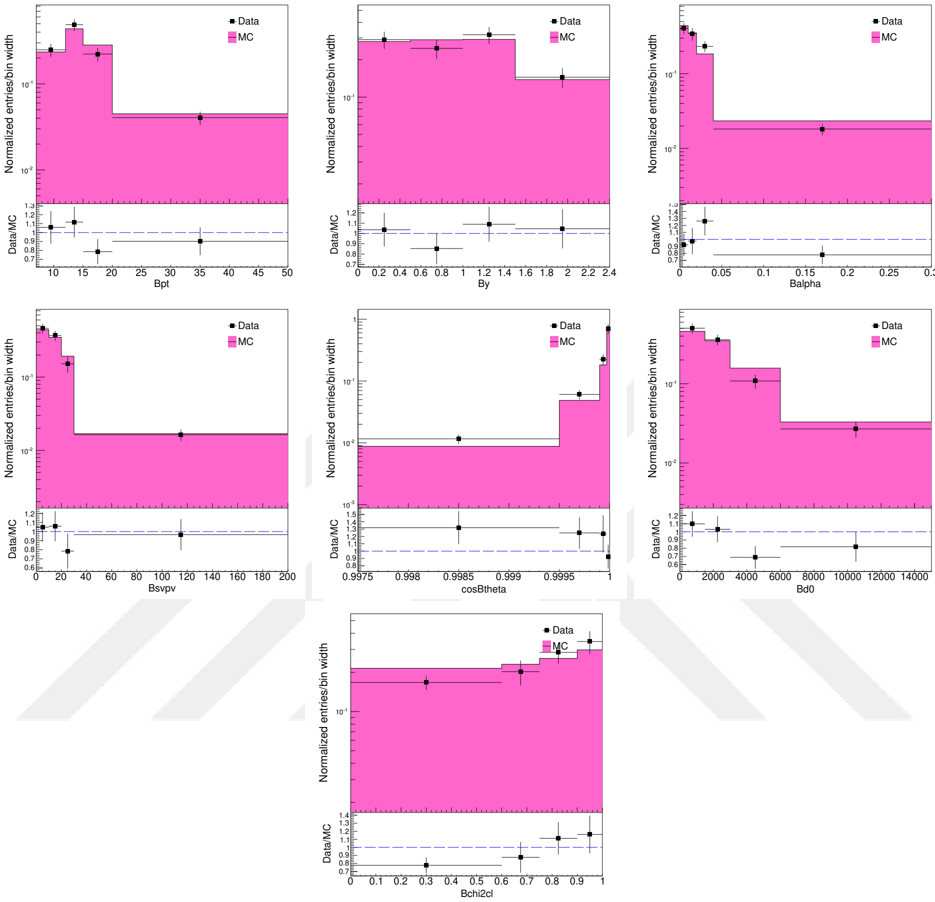

Figure D1. Comparison of various B_s^0 meson variables between data and MC in pp analysis. From left to right then top to bottom. B_s^0 p_T, B_s^0 rapidity, α angel, B_s^0 normalized decay length, θ angel, 2D B_s^0 normalized decay length, vertex fit χ^2

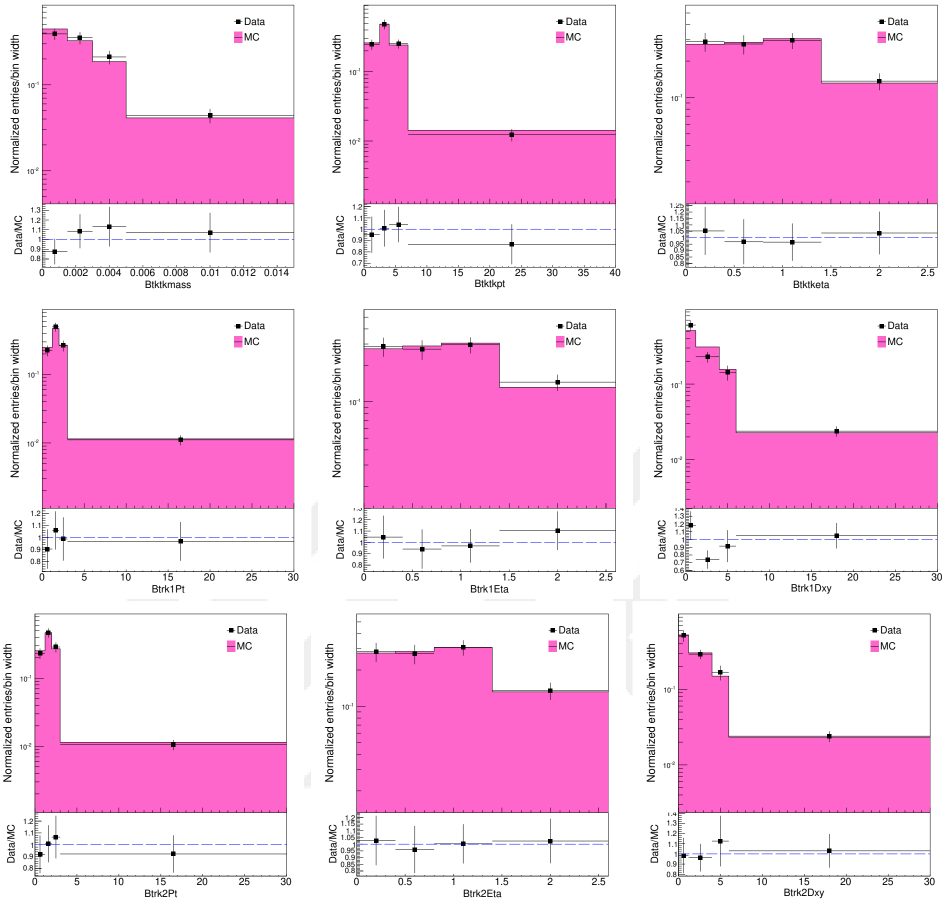

Figure D2. Comparison of various B_s^0 meson variables between data and MC in pp analysis. From left to right then top to bottom. difference between reconstructed ϕ meson mass and PDG mass, ϕ p_T, ϕ pseudo-rapidity, K^+ track p_T, K^+ track pseudo-rapidity, K^+ track normalized d0, K^- track p_T, K^- track pseudo-rapidity, K^- track normalized d0,

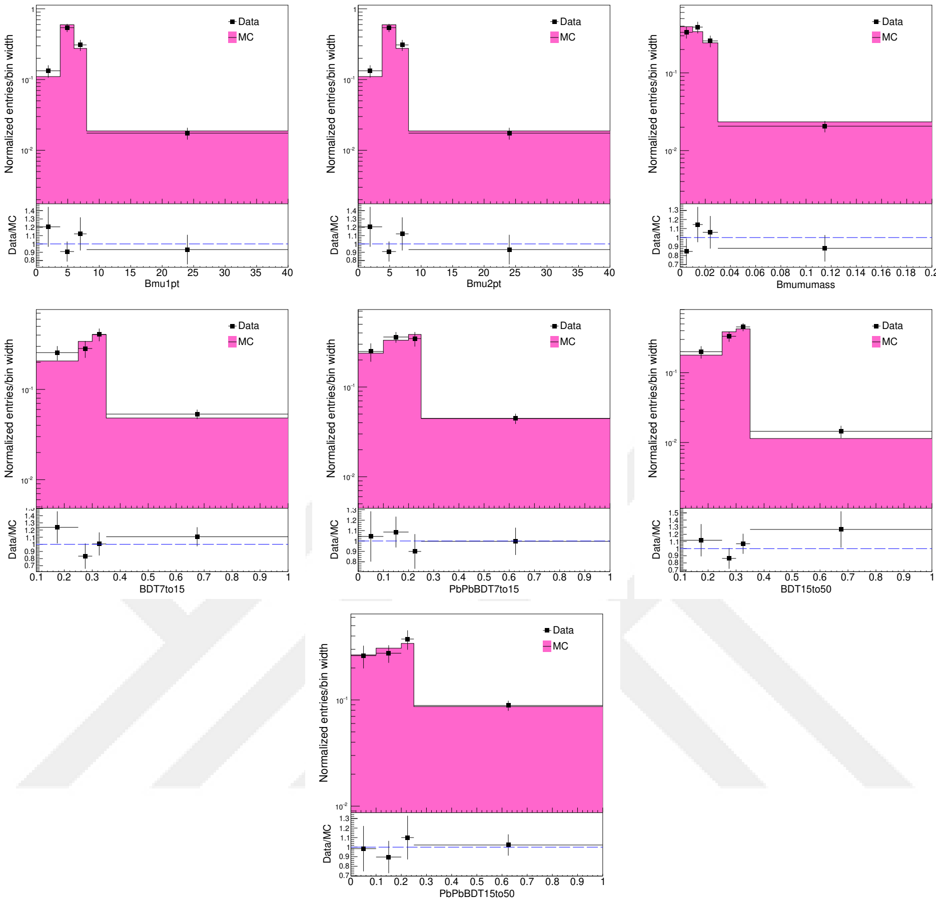

Figure D3. Comparison of various B_s^0 meson variables between data and MC in pp analysis. From left to right then top to bottom. difference between reconstructed ϕ meson mass and PDG mass, muon plus p_T, muon minus p_T, difference between reconstructed J/ψ meson mass and PDG mass, pp BDT value used in B_s^0 p_T 7 to 15 GeV/c analysis, pp BDT value used in B_s^0 p_T 15 to 50 GeV/c analysis, PbPb BDT value used in B_s^0 p_T 7 to 15 GeV/c analysis produced with pp MC and data, PbPb BDT value used in B_s^0 p_T 15 to 50 GeV/c analysis produced with pp MC and data.

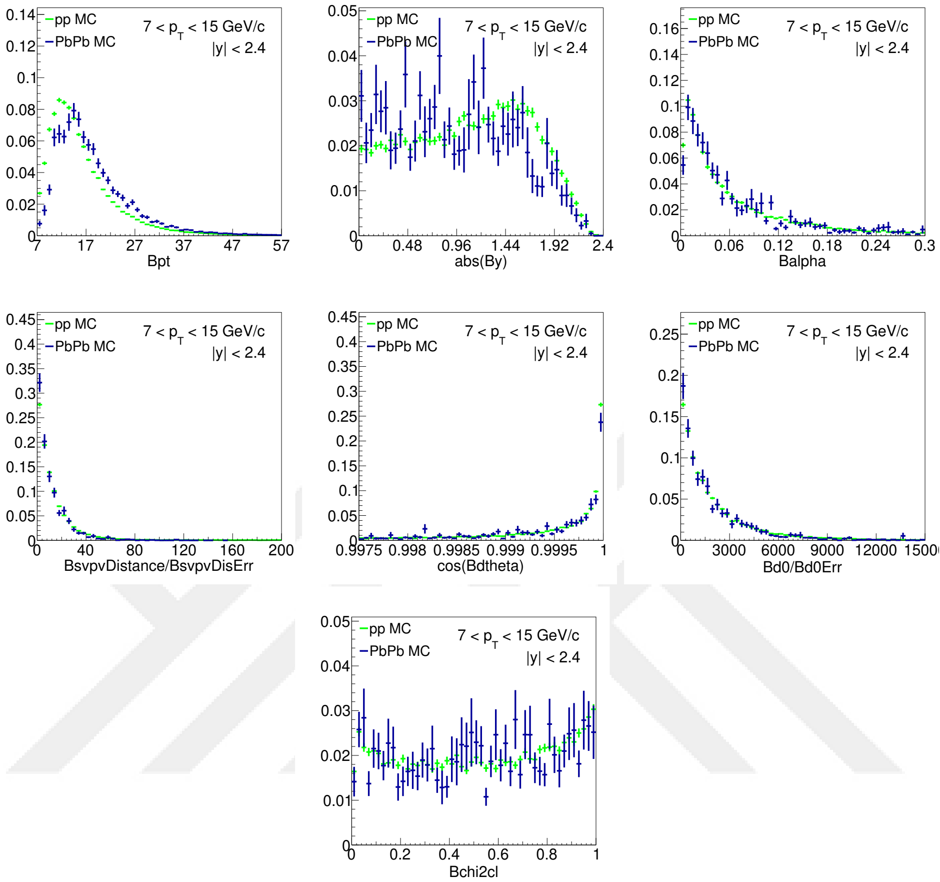

Figure D4. Comparison of various B_s^0 meson variables between data and MC in pp analysis for B_s^0 p_T 7 to 15 GeV/c. From left to right then top to bottom. B_s^0 p_T, B_s^0 rapidity, α angel, B_s^0normalized decay length, θ angel, 2D B_s^0 normalized decay length, vertex fit χ^2

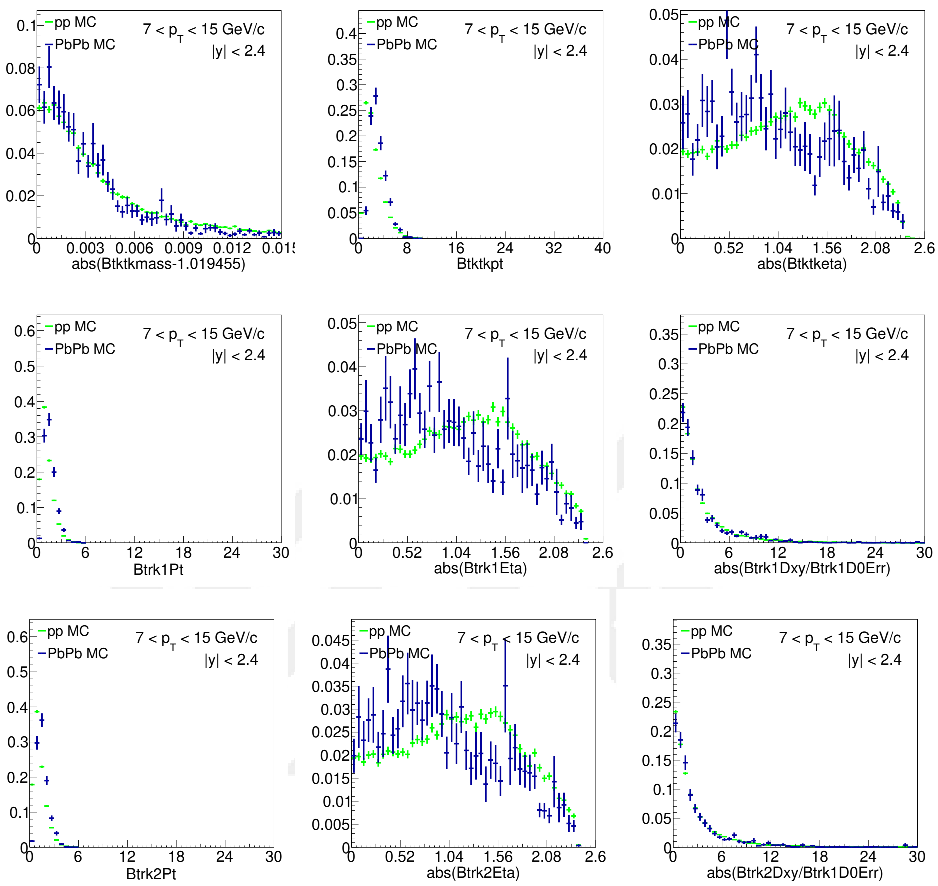

Figure D5. Comparison of various B_s^0 meson variables between data and MC in pp analysis for B_s^0 p_T 7 to 15 GeV/c. From left to right then top to bottom. difference between reconstructed ϕ meson mass and PDG mass, ϕ p_T, ϕ pseudo-rapidity, K^+ track p_T, K^+ track pseudo-rapidity, K^+ track normalized d0, K^- track p_T, K^- track pseudo-rapidity, K^- track normalized d0.

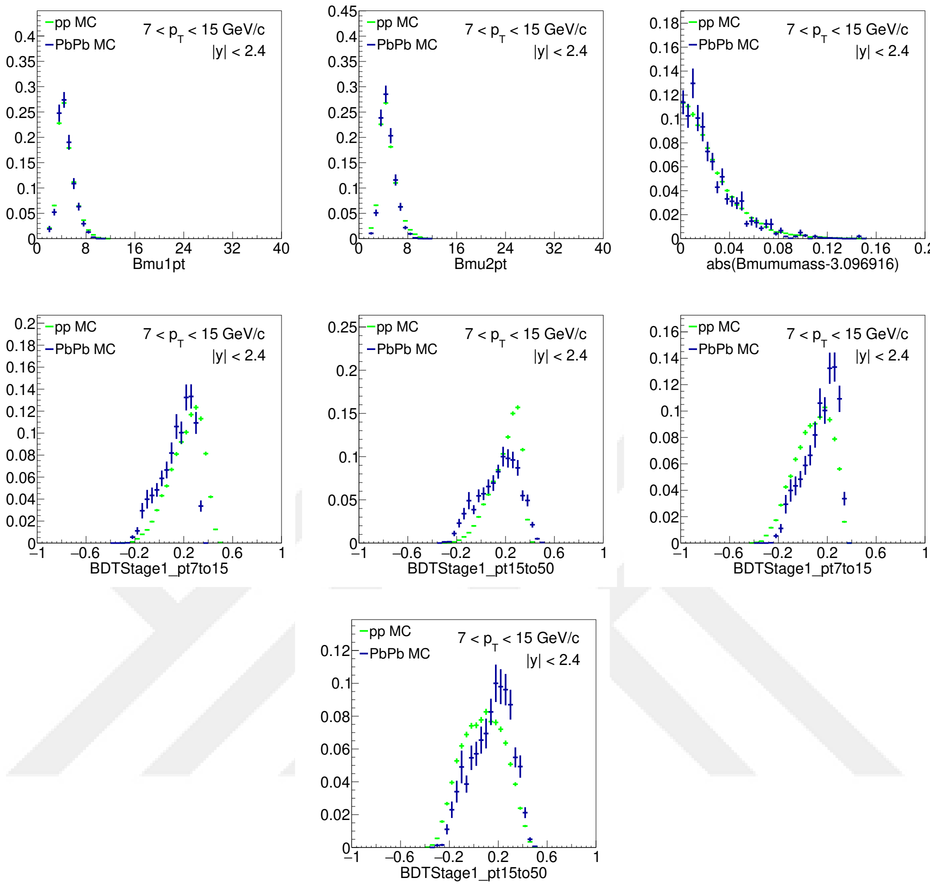

Figure D6. Comparison of various B_s^0 meson variables between data and MC in pp analysis for B_s^0 p_T 7 to 15 GeV/c. From left to right then top to bottom. muon plus p_T, muon minus p_T, difference between reconstructed J/ψ meson mass and PDG mass, pp BDT vs PbPb BDT values used in B_s^0 p_T 7 to 15 GeV/c analysis, pp BDT vs PbPb BDT values used in B_s^0 p_T 15 to 50 GeV/c analysis, PbPb BDT values used in B_s^0 p_T 7 to 15 GeV/c comparison between pp and PbPb MC, PbPb BDT values used in B_s^0 p_T 15 to 50 GeV/c comparison between pp and PbPb MC.

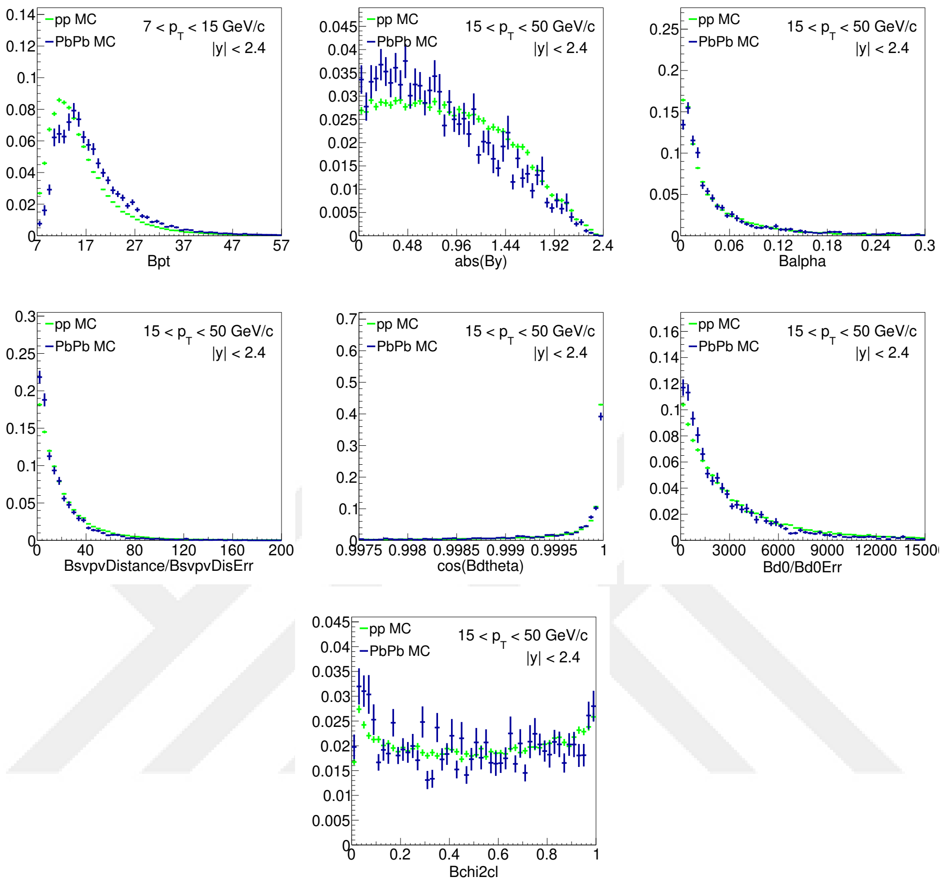

Figure D7. Comparison of various B_s^0meson variables between data and MC in pp analysis for B_s^0 p_T 15 to 50 GeV/c. From left to right then top to bottom. $B_s^0 p_T$, B_s^0 rapidity, α angel, B_s^0 normalized decay length, θ angel, 2D B_s^0 normalized decay length, vertex fit χ^2

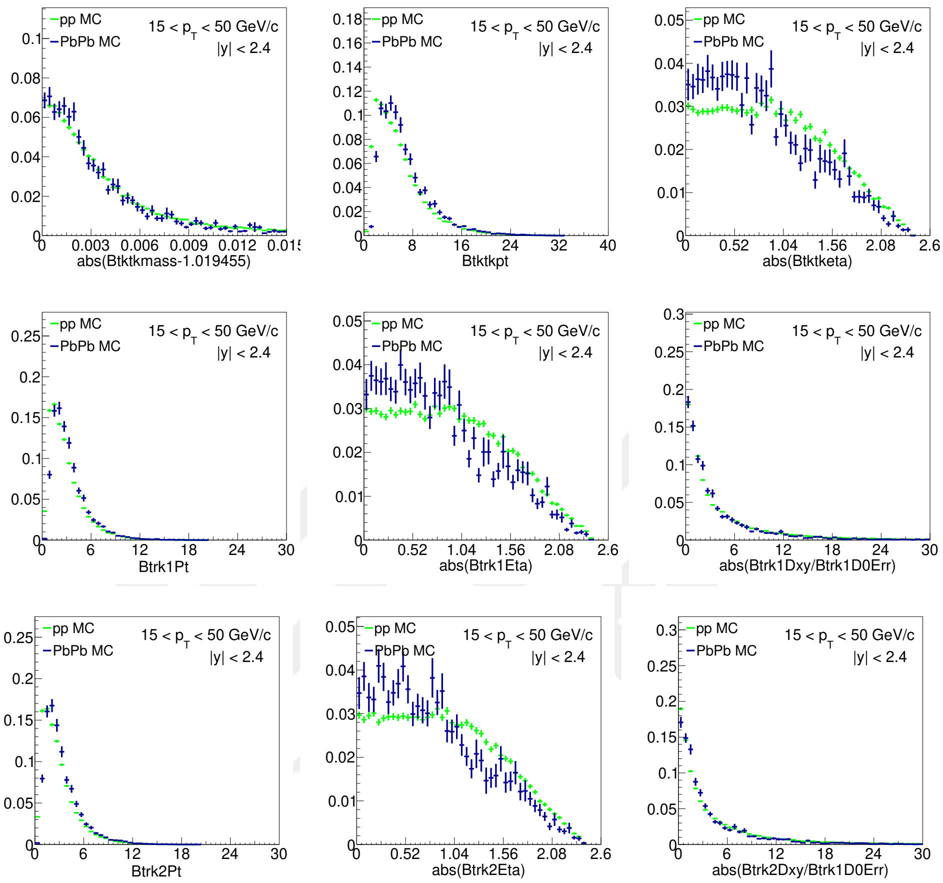

Figure D8. Comparison of various B_s^0meson variables between data and MC in pp analysis for B_s^0 p_T 15 to 50 GeV/c. From left to right then top to bottom. difference between reconstructed ϕ meson mass and PDG mass, ϕ p_T, ϕ pseudo-rapidity, K^+ track p_T, K^+ track pseudo-rapidity, K^+ track normalized d0, K^- track p_T, K^- track pseudo-rapidity, K^- track normalized d0.

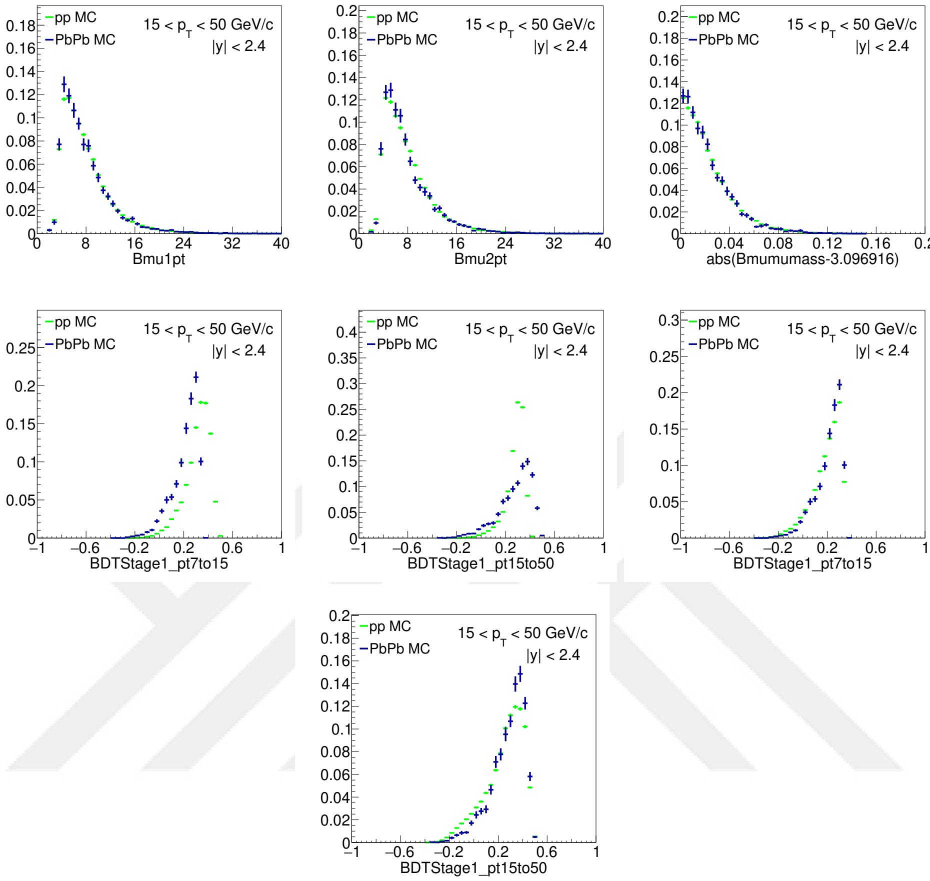

Figure D9. Comparison of various B_s^0meson variables between data and MC in pp analysis for B_s^0 p_T 15 to 50 GeV/c. From left to right then top to bottom. muon plus p_T, muon minus p_T, difference between reconstructed J/ψ meson mass and PDG mass, pp BDT vs PbPb BDT values used in B_s^0 p_T 7 to 15 GeV/c analysis, pp BDT vs PbPb BDT values used in B_s^0 p_T 15 to 50 GeV/c analysis, PbPb BDT values used in B_s^0 p_T 7 to 15 GeV/c comparison between pp and PbPb MC, PbPb BDT values used in B_s^0 p_T 15 to 50 GeV/c comparison between pp and PbPb MC.

E Systematics on Signal Extraction Fit

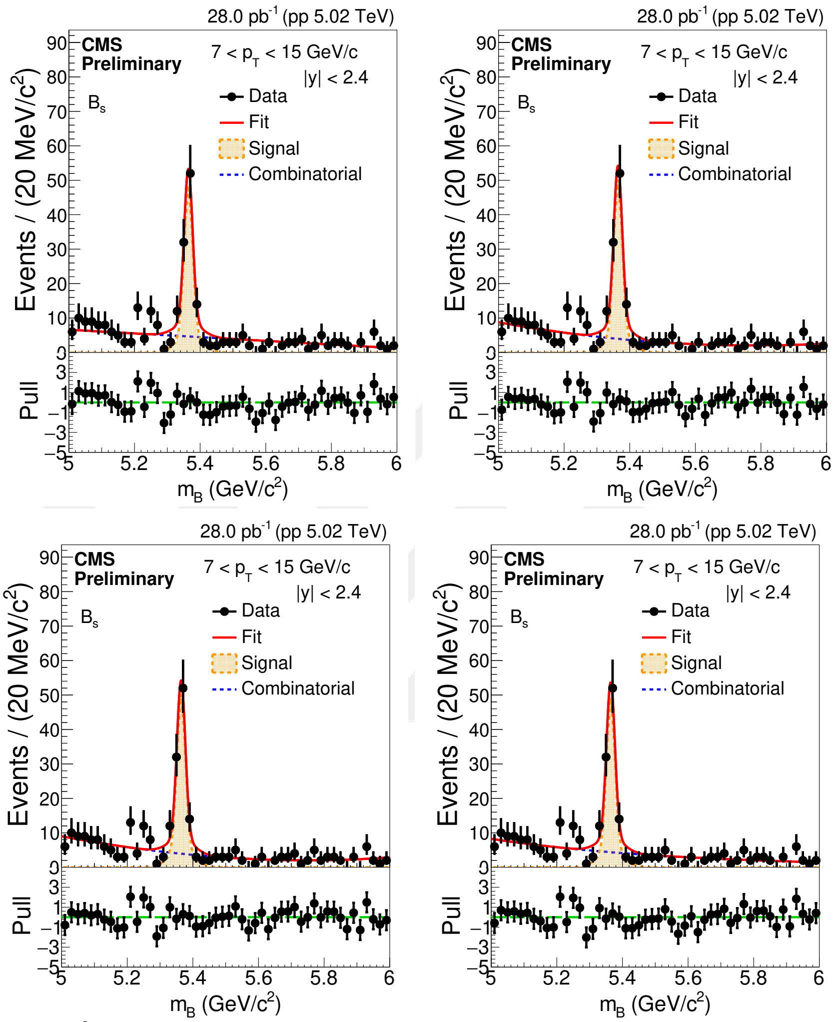

Figure E1. B_s^0 invariant mass fit for p_T interval 7 to 50 GeV/c in 5.02 TeV pp. From left to right is the default linear, the background PDF with 2nd order polynomial, 3rd order polynomial,and exponential functions are represented, respectively.

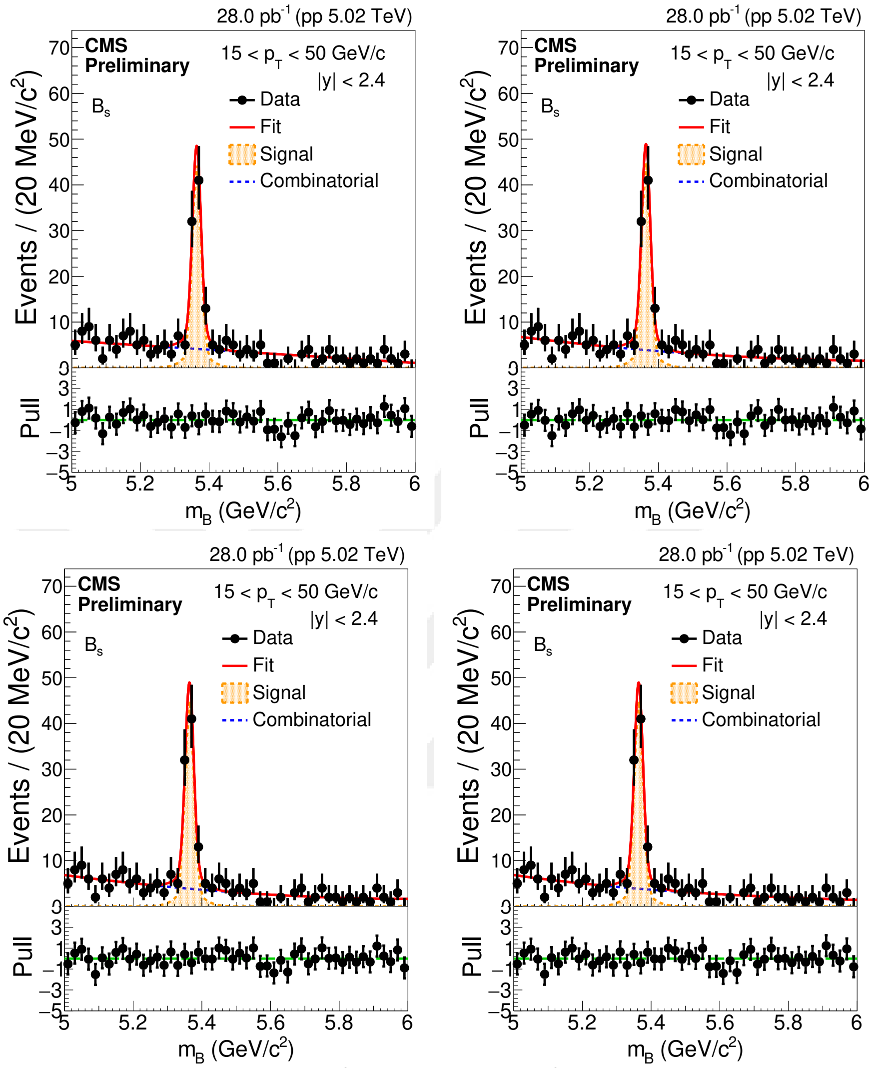

Figure E2. Invariant mass fit of B_s^0 candidates for B_s^0 p_T 15 to 50 GeV/c in 5.02 TeV pp. The background PDF from left to right is default linear, 2nd order polynomial, 3rd order polynomial, and exponential.

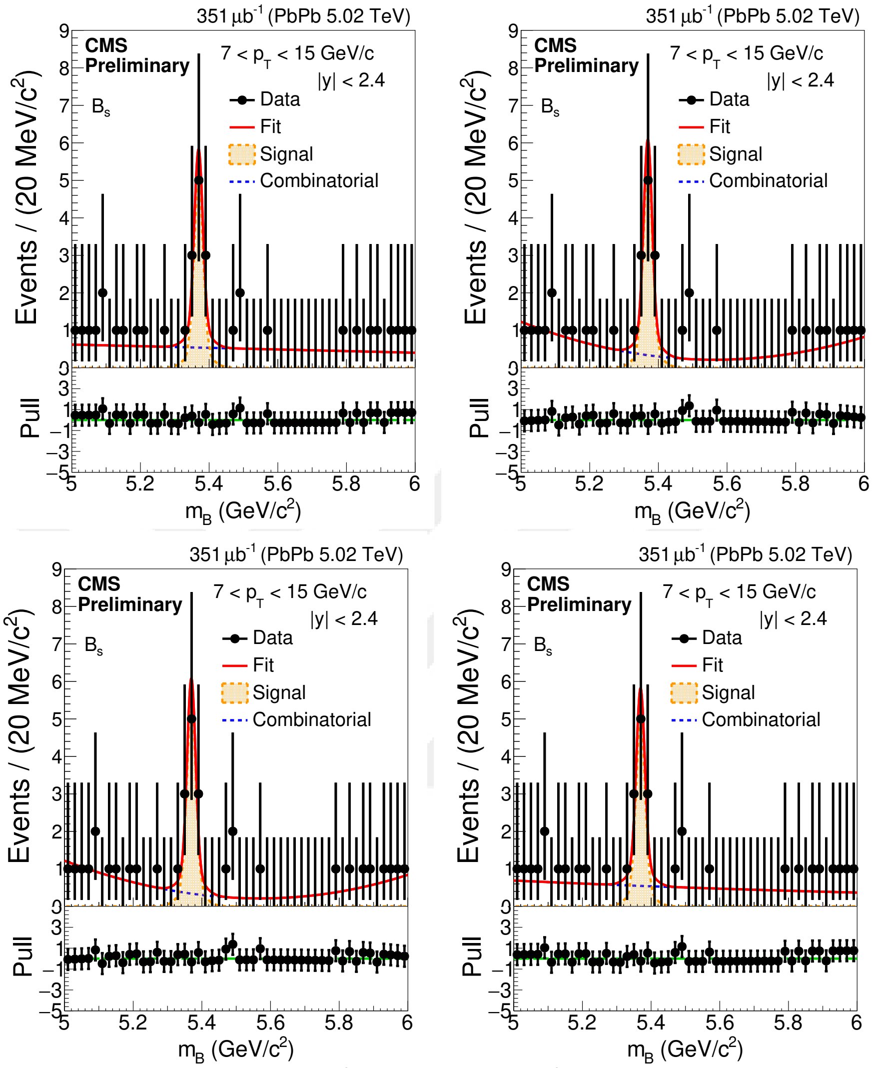

Figure E3. Invariant mass fit of B_s^0 candidates for B_s^0 p_T 7 to 15 GeV/c in 5.02 TeV PbPb. The background PDF from left to right is default linear, 2nd order polynomial, 3rd order polynomial, and exponential.

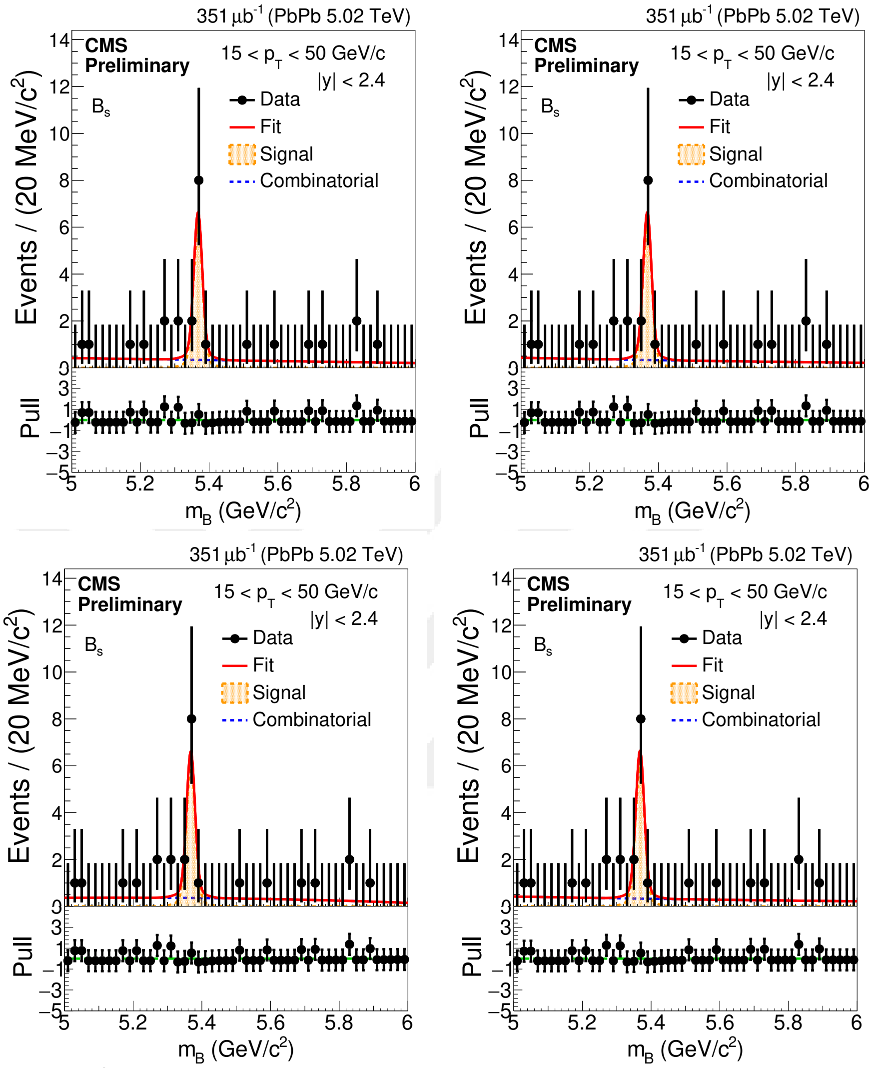

Figure E4. B_s^0 invariant mass fit for p_T interval 15 to 50 GeV/c in 5.02 TeV pp. From left to right is the default linear, the background PDF with 2nd order polynomial, 3rd order polynomial, and exponential functions are represented, respectively.

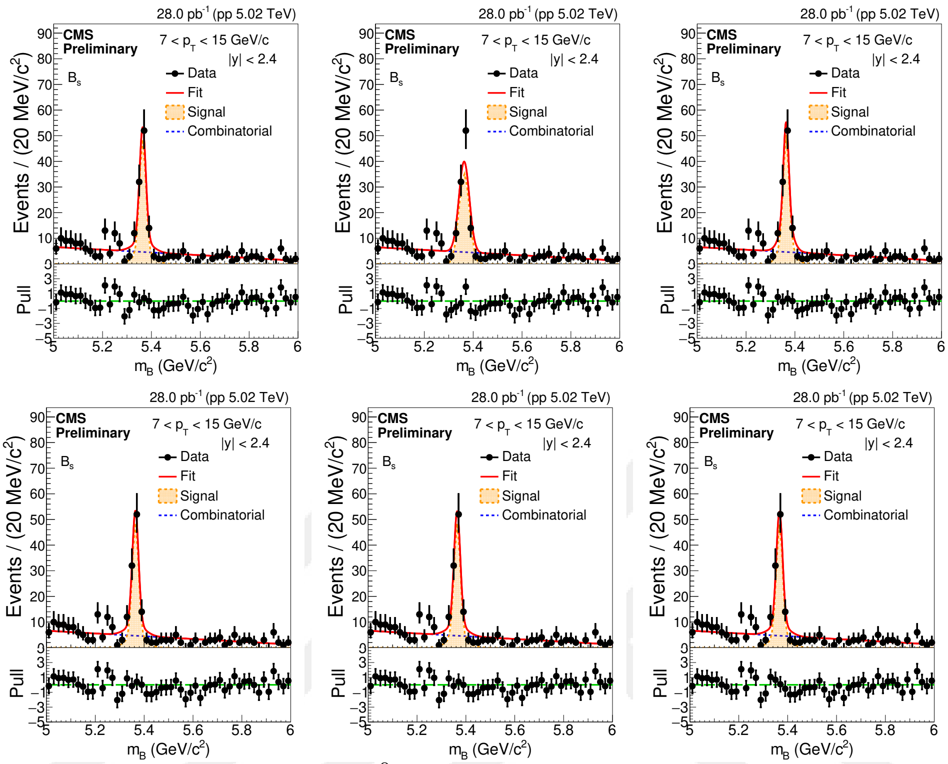

Figure E5. Invariant mass fit of B_s^0 candidates in 5.02 TeV for pp collisions with p_T interval 7 to 15 GeV/c. The upper left plot shows the signal PDF with the default setting 2nd order polynomial, the upper middle plot refers the signal PDF with single Gaussian, and the upper right plot represents the signal PDF with triple Gaussian.The bottom plots show the signal PDF with default setting width decreased,increased and mean fixed, respectively.

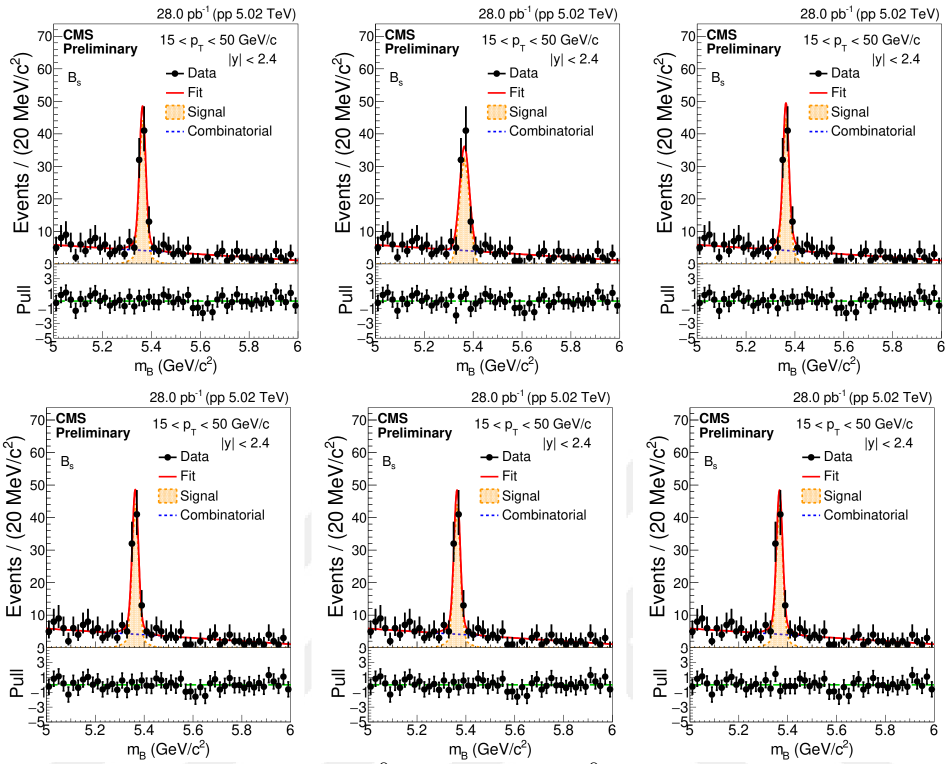

Figure E6. Invariant mass fit of B_s^0 candidates for B_s^0 p_T 15 to 50 GeV/c in 5.02 TeV pp. The signal PDF from left to right is default 2nd order polynomial, single Gaussian, triple Gaussian, width decreased, width increased, and mean fixed.

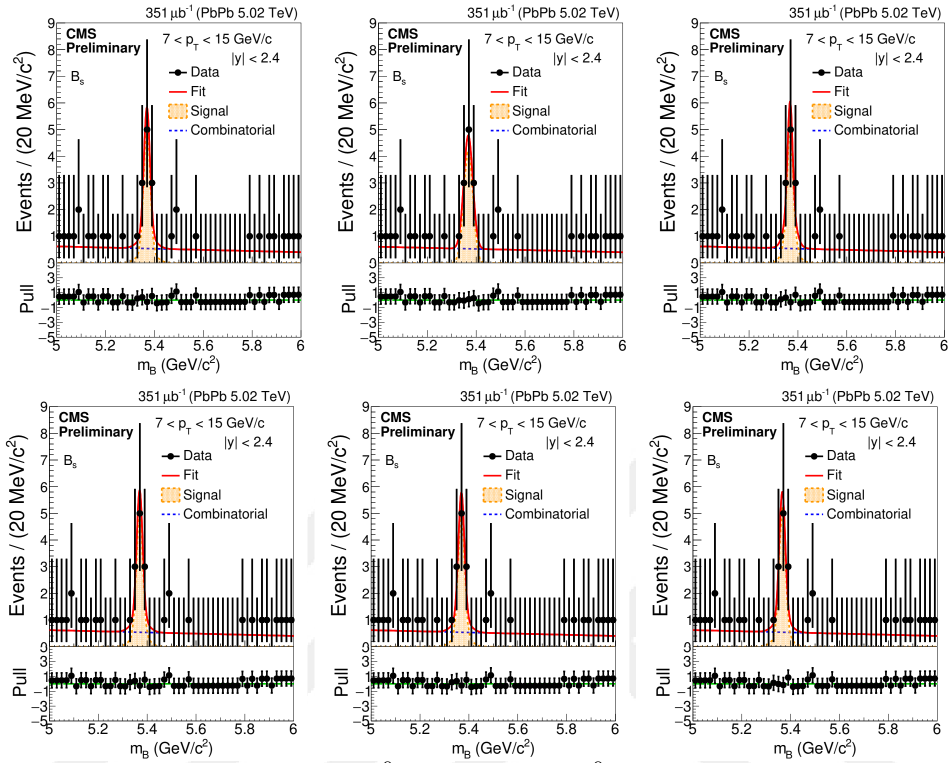

Figure E7. Invariant mass fit of B_s^0 candidates for B_s^0 p_T 7 to 15 GeV/c in 5.02 TeV PbPb. The signal PDF from left to right is default 2nd order polynomial, single Gaussian, triple Gaussian, width decreased, width increased, and mean fixed.

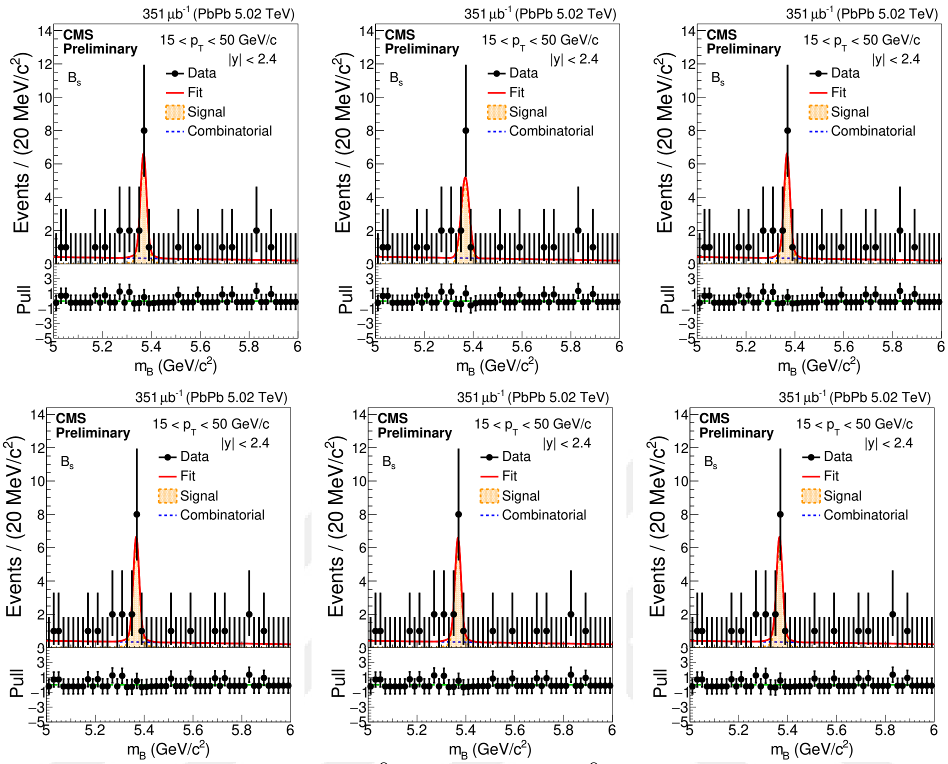

Figure E8. Invariant mass fit of B_s^0 candidates for B_s^0 p_T 15 to 50 GeV/c in 5.02 TeV PbPb. The signal PDF from left to right is default 2nd order polynomial, single Gaussian, triple Gaussian, width decreased, width increased, and mean fixed.

F Prompt J/ψ background

The B_s^0 mass spectra are performed with using prompt J/ψMC samples with different BDT cut value for PbPb B_s^0 p_T interval 7 to 15 and 15 to 50 GeV/c. The figures below represents the resulting B_s^0 mass spectra using prompt J/ψ PbPb MC samples with different BDT cut value for various J/ψ p_T interval, 0 to 3, 3 to 6, 6 to 9, 9 to 12, 12 to 15 , 15 to 30 and 30 to infinite.

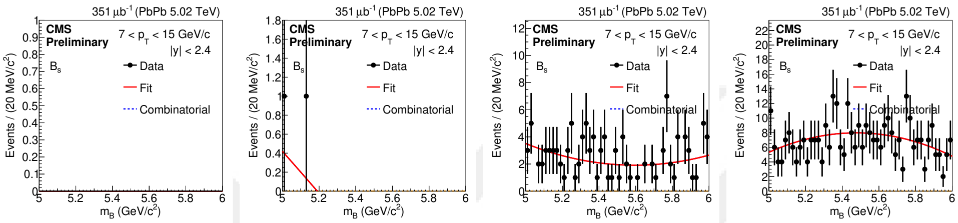

Figure F1. The resulting B_s^0 mass spectra using prompt J/ψ MC samples with various BDT cut value in PbPb B_s^0 p_T 7 to 15 GeV/c and J/ψ p_T interval 0 to 3 GeV/c sample.

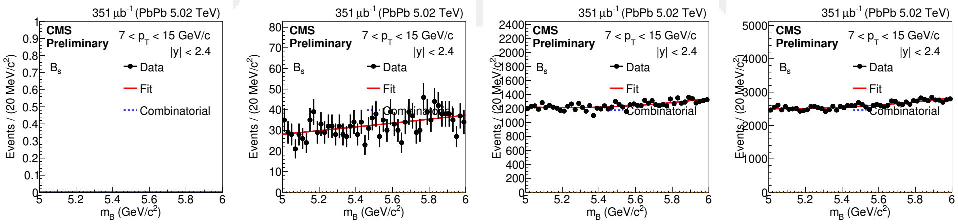

Figure F2. The resulting B_s^0 mass spectra using prompt J/ψMC samples with various BDT cut value in PbPb B_s^0 p_T 7 to 15 GeV/c and J/ψ p_T interval 3 to 6 GeV/c.

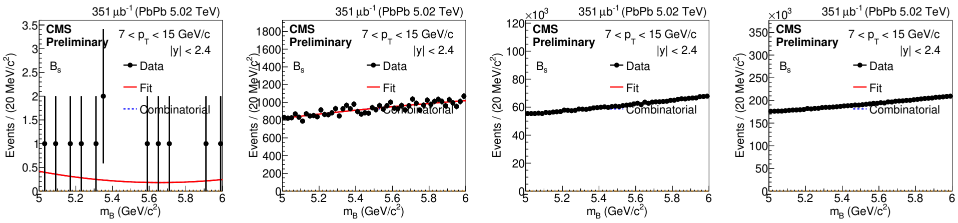

Figure F3. The resulting B_s^0 mass spectra using prompt J/ψ MC samples with various BDT cut value in PbPb B_s^0 p_T 7 to 15 GeV/c and J/ψ p_T interval 6 to 9 GeV/c

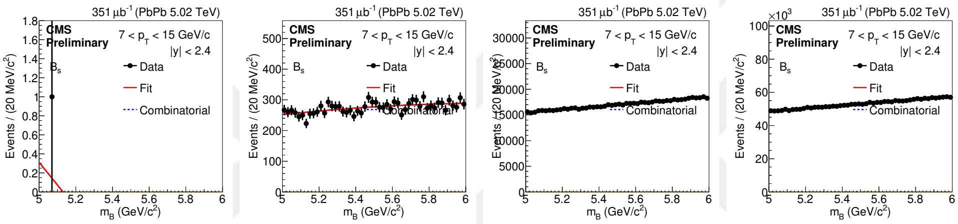

Figure F4. The resulting B_s^0 mass spectra using prompt J/ψ MC samples with various BDT cut value in PbPb B_s^0 p_T 7 to 15 GeV/c and J/ψ p_T interval 9 to 12 GeV/c.

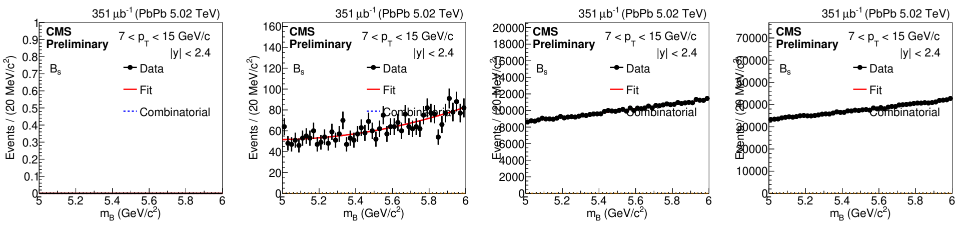

Figure F5. The resulting B_s^0 mass spectra using prompt J/ψ MC samples with various BDT cut value in PbPb B_s^0 p_T 7 to 15 GeV/c and J/ψ p_T interval 12 to 15 GeV/c.

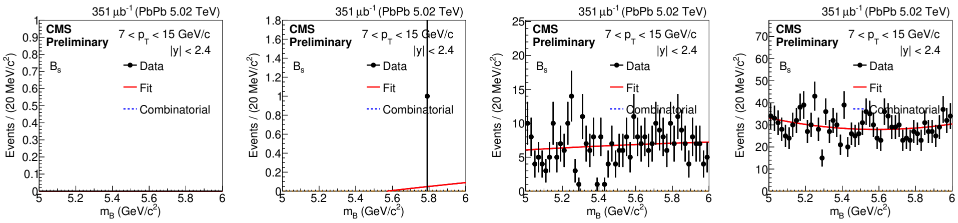

Figure F6. The resulting B_s^0 mass spectra using prompt J/ψ MC samples with various BDT cut value in PbPb B_s^0 p_T 7 to 15 GeV/c and J/ψ p_T interval 15 to 30 GeV/c.

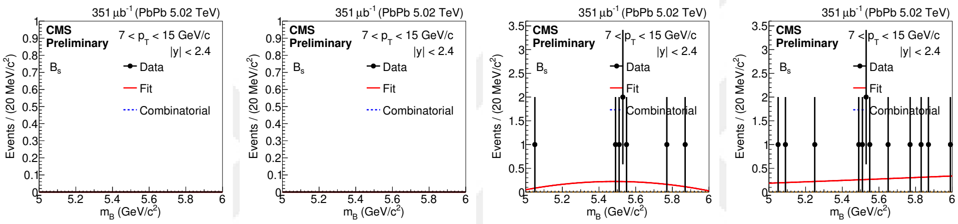

Figure F7. The resulting B_s^0 mass spectra using prompt J/ψ MC samples with various BDT cut value in PbPb B_s^0 p_T 7 to 15 GeV/c and J/ψ p_T interval above 30 GeV/c

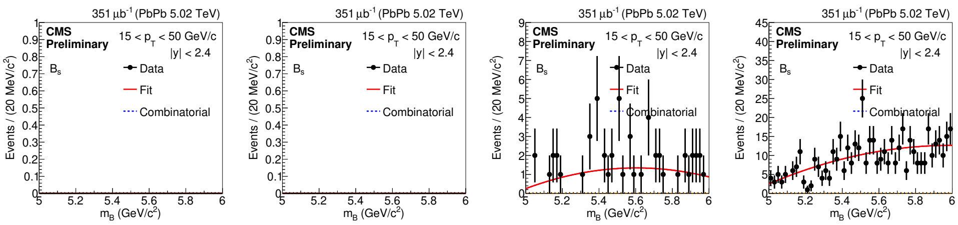

Figure F8. B_s^0 mass spectra using prompt J/ψ MC samples with various BDT cut value scan in PbPb B_s^0 p_T 15 to 50 GeV/c and J/ψ p_T 0 to 3 GeV/c sample.

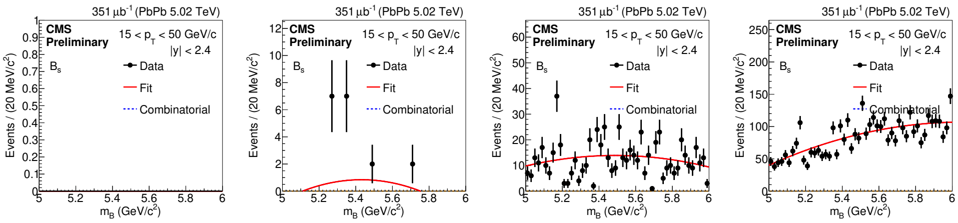

Figure F9. B_s^0 mass spectra using prompt J/ψ MC samples with various BDT cut value scan in PbPb B_s^0 p_T 15 to 50 GeV/c and J/ψ p_T 3 to 6 GeV/c sample.

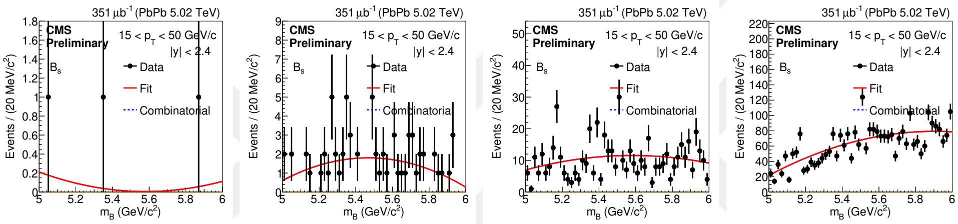

Figure F10. B_s^0 mass spectra using prompt J/ψ MC samples with various BDT cut value scan in PbPb B_s^0 p_T 15 to 50 GeV/c and J/ψ p_T 6 to 9 GeV/c sample.

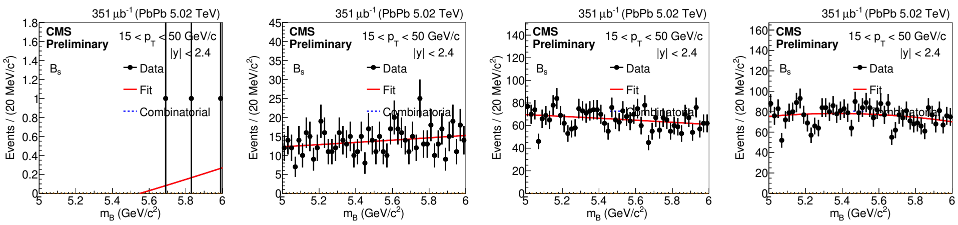

Figure F11. B_s^0 mass spectra using prompt J/ψ MC samples with various BDT cut value scan in PbPb B_s^0 p_T 15 to 50 GeV/c and J/ψ p_T 9 to 12 GeV/c sample

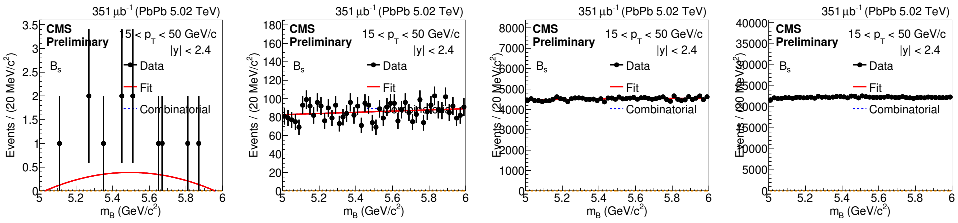

Figure F12. B_s^0 mass spectra using prompt J/ψ MC samples with various BDT cut value scan in PbPb B_s^0 p_T 15 to 50 GeV/c and J/ψ p_T 12 to 15 GeV/c sample

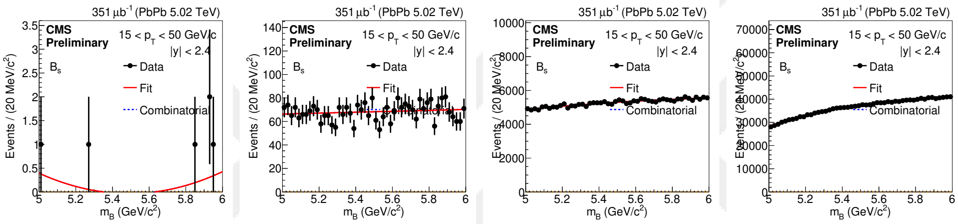

Figure F13. B_s^0 mass spectra using prompt J/ψ MC samples with various BDT cut value scan in PbPb B_s^0 p_T 15 to 50 GeV/c and J/ψ p_T 15 to 30 GeV/c sample

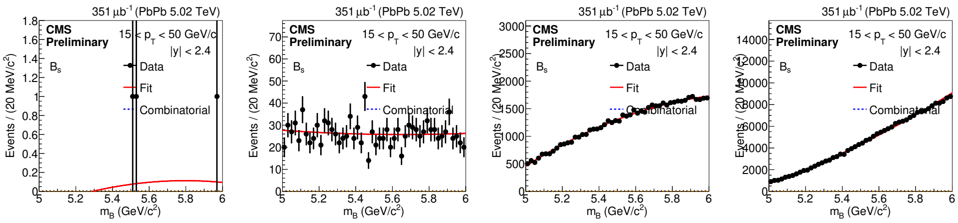

Figure F14. B_s^0 mass spectra using prompt J/ψ MC samples with various BDT cut value scan in PbPb B_s^0 p_T 15 to 50 GeV/c and J/ψ p_T larger than 30 GeV/c sample

G Cut value variation

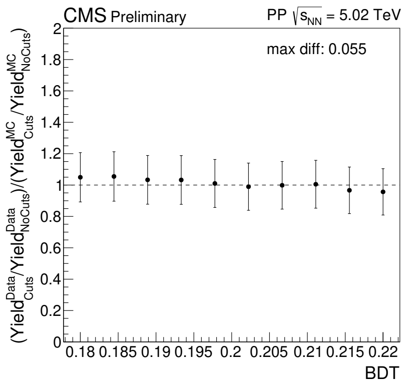

Figure G1. Double ratio of the cut variation for BDT discriminant using pp data and MC

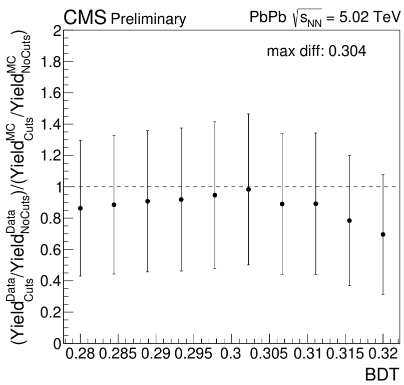

Figure G2. Double ratio of the cut variation for BDT discriminant using PbPb data and MC

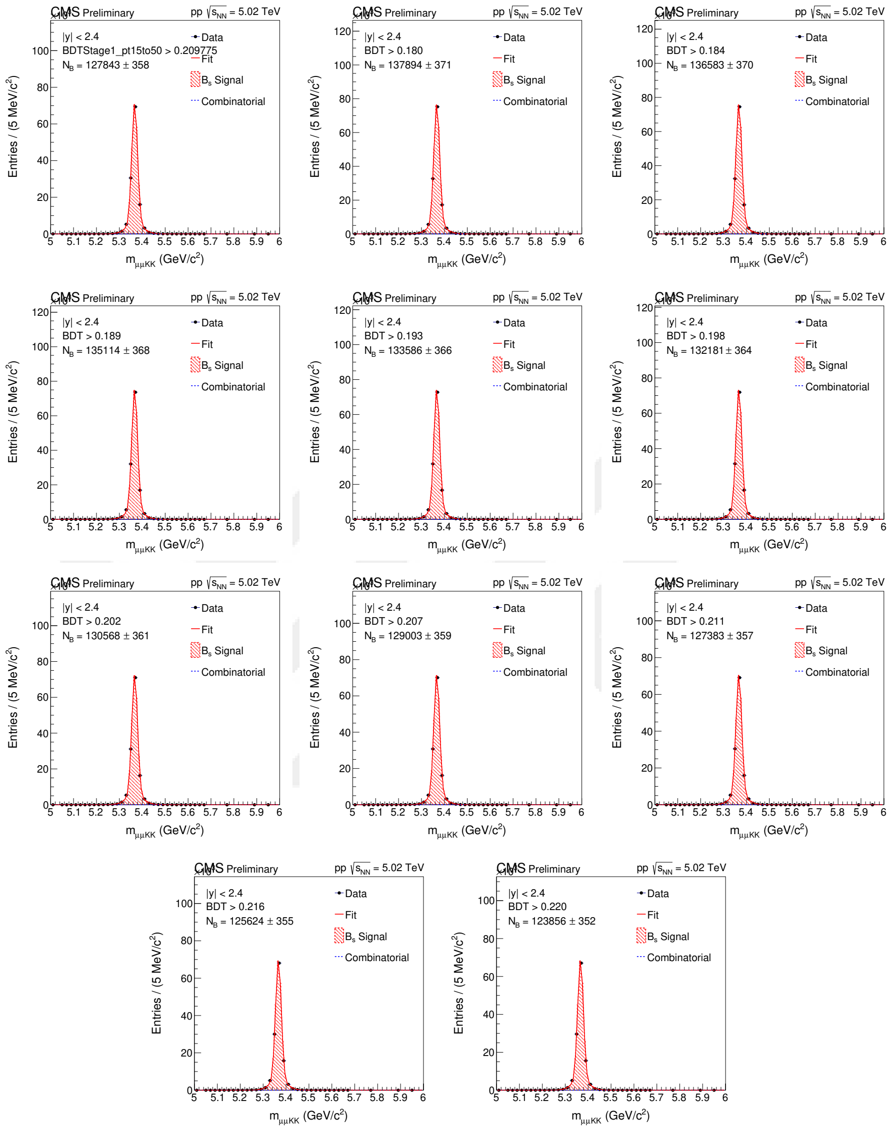

Figure G3. Scanning of BDT cut value and the mass spectrum fitting for pp MC. The 1st spectrum on the top left is derived with nominal analysis value BDT = 0.21. The following spectrums have the BDT cut value varied from 0.18 increasingly to 0.22. which is written in the plots.

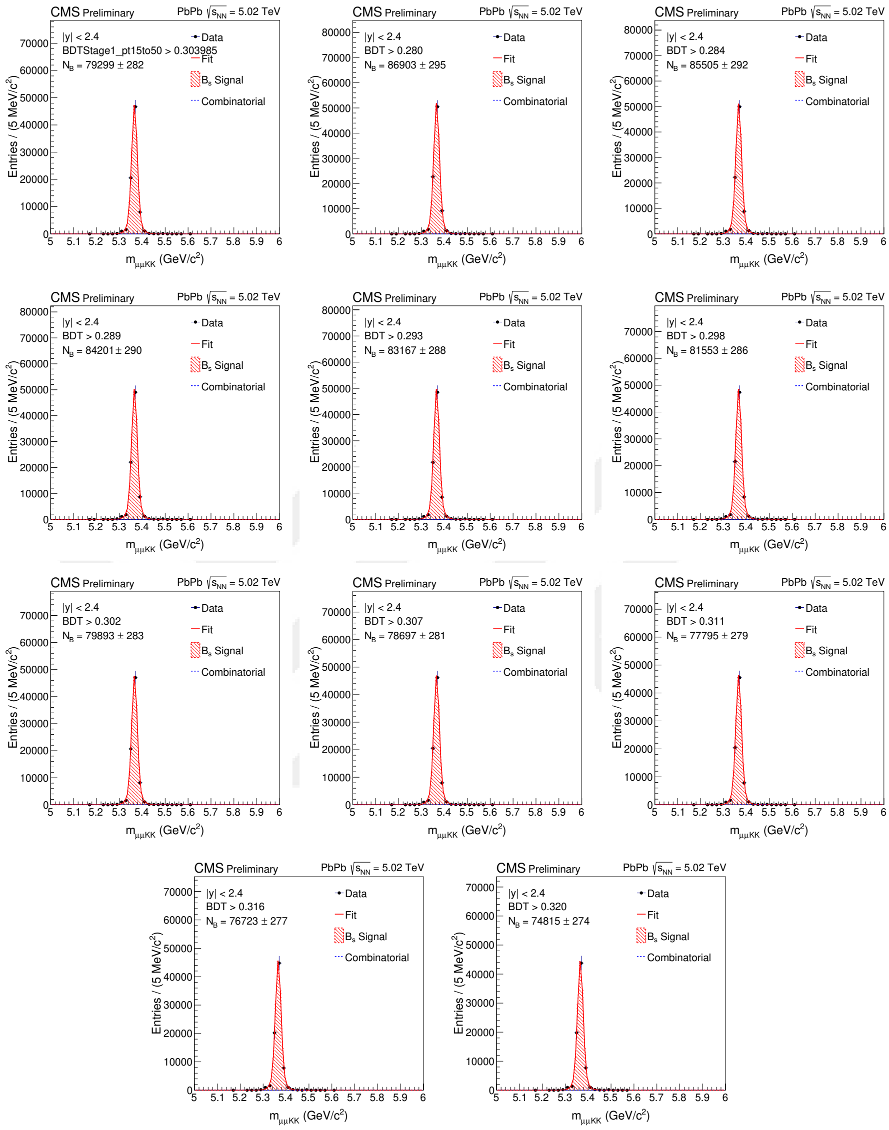

Figure G4. Scanning of BDT cut value and the summary plots of mass spectrum fitting for PbPb MC.The 1st spectrum on the top left is derived with applying nominal analysis value BDT = 0.30. The following spectra have the BDT cut value varied from 0.28 increasingly to 0.32.

H Datasets

The list of data sets are given in the following table.

Table H1. List of pp and PbPb data sets used for this analysis.

System	Primary dataset
pp	`/DoubleMu/Run2015E-PromptReco-v1/AOD`
PbPb	`HiOniaL1DoubleMu0/HIRun2015-PromptReco-v1/AOD`
PbPb	`HiOniaDoubleMu0B/HIRun2015-PromptReco-v1/AOD`
PbPb	`HiOniaDoubleMu0C/HIRun2015-PromptReco-v1/AOD`
PbPb	`HiOniaDoubleMu0D/HIRun2015-PromptReco-v1/AOD`
PbPb	Combined All

The JSON file is a lightweight data-interchange format which is easy for humans to read and write and for machines to parse and generate. The JSON is built on two structures like a collection of name or value pairs and an ordered list of values. Former one is used in various languages, this is realized as an object, record, dictionary, or associative array. The latter is used in most languages, this is realized as an array, vector, list, or sequence. These are universal data structures. All modern programming languages support these structures in one form or another. Furthermore, due to these structures, a data format can be interchangeable with programming languages.

- /afs/cern.ch/cms/CAF/CMSCOMM/COMM_DQM/certification/Collisions15/HI/
  Cert_262548-263757_PromptReco_HICollisions15_JSON_MuonPhys_v2.txt
- /afs/cern.ch/cms/CAF/CMSCOMM/COMM_DQM/certification/Colli-

sions15/5TeV/

Cert_262081-262328_5TeV_PromptReco_Collisions15_25ns_JSON_MuonPhys.txt

I Simulated Samples

The produced signal, prompt and non-prompt MC samples datasets names for pp and PbPb are listed in the following Table I1..

Table I1. MC samples data set names

pp signal
/BsToJpsiPhi_Pthat0_Bpt5p0_pp_5p02-Pythia8/HINppWinter16DR-75X_mcRun2_asymptotic_ppAt5TeV_v3-v2/AODSIM
/BsToJpsiPhi_Pthat5_Bpt5p0_pp_5p02-Pythia8/HINppWinter16DR-75X_mcRun2_asymptotic_ppAt5TeV_v3-v2/AODSIM
/BsToJpsiPhi_Pthat10_Bpt5p0_pp_5p02-Pythia8/HINppWinter16DR-75X_mcRun2_asymptotic_ppAt5TeV_v3-v2/AODSIM
/BsToJpsiPhi_Pthat15_Bpt5p0_pp_5p02-Pythia8/HINppWinter16DR-75X_mcRun2_asymptotic_ppAt5TeV_v3-v2/AODSIM
/BsToJpsiPhi_Pthat30_Bpt5p0_pp_5p02-Pythia8/HINppWinter16DR-75X_mcRun2_asymptotic_ppAt5TeV_v3-v2/AODSIM
/BsToJpsiPhi_Pthat50_Bpt5p0_pp_5p02-Pythia8/HINppWinter16DR-75X_mcRun2_asymptotic_ppAt5TeV_v3-v2/AODSIM
pp non-prompt J/ψ
/BJpsiMM_5p02TeV_TuneCUETP8M1/HINppWinter16DR-75X_mcRun2_asymptotic_ppAt5TeV_v3-v1/AODSIM
/BJpsiMM_5p02TeV_TuneCUETP8M1/HINppWinter16DR-75X_mcRun2_asymptotic_ppAt5TeV_v3_ext1-v1/AODSIM
pp prompt J/ψ
/JpsiMM_5p02TeV_TuneCUETP8M1/HINppWinter16DR-75X_mcRun2_asymptotic_ppAt5TeV_v3-v1/AODSIM
/JpsiMM_5p02TeV_TuneCUETP8M1/HINppWinter16DR-75X_mcRun2_asymptotic_ppAt5TeV_v3_ext1-v1/AODSIM
PbPb signal
/Pythia8_BJpsiMM_ptJpsi_00_03_Hydjet_MB/HINPbPbWinter16DR-75X_mcRun2_HeavyIon_v13-v1/AODSIM
/Pythia8_BJpsiMM_ptJpsi_03_06_Hydjet_MB/HINPbPbWinter16DR-75X_mcRun2_HeavyIon_v13-v1/AODSIM
/Pythia8_BJpsiMM_ptJpsi_03_06_Hydjet_MB/HINPbPbWinter16DR-75X_mcRun2_HeavyIon_v13_ext1-v1/AODSIM
/Pythia8_BJpsiMM_ptJpsi_06_09_Hydjet_MB/HINPbPbWinter16DR-75X_mcRun2_HeavyIon_v13-v1/AODSIM
/Pythia8_BJpsiMM_ptJpsi_06_09_Hydjet_MB/HINPbPbWinter16DR-75X_mcRun2_HeavyIon_v13_ext1-v1/AODSIM
/Pythia8_BJpsiMM_ptJpsi_09_12_Hydjet_MB/HINPbPbWinter16DR-75X_mcRun2_HeavyIon_v13-v1/AODSIM
/Pythia8_BJpsiMM_ptJpsi_12_15_Hydjet_MB/HINPbPbWinter16DR-75X_mcRun2_HeavyIon_v13-v1/AODSIM
/Pythia8_BJpsiMM_ptJpsi_15_30_Hydjet_MB/HINPbPbWinter16DR-75X_mcRun2_HeavyIon_v13-v1/AODSIM
/Pythia8_BJpsiMM_ptJpsi_30_inf_Hydjet_MB/HINPbPbWinter16DR-75X_mcRun2_HeavyIon_v13-v1/AODSIM
PbPb prompt J/ψ
/Pythia8_JpsiMM_ptJpsi_00_03_Hydjet_MB/HINPbPbWinter16DR-75X_mcRun2_HeavyIon_v13-v1/AODSIM
/Pythia8_JpsiMM_ptJpsi_03_06_Hydjet_MB/HINPbPbWinter16DR-75X_mcRun2_HeavyIon_v13-v1/AODSIM
/Pythia8_JpsiMM_ptJpsi_03_06_Hydjet_MB/HINPbPbWinter16DR-75X_mcRun2_HeavyIon_v13_ext1-v1/AODSIM
/Pythia8_JpsiMM_ptJpsi_06_09_Hydjet_MB/HINPbPbWinter16DR-75X_mcRun2_HeavyIon_v13-v1/AODSIM
/Pythia8_JpsiMM_ptJpsi_06_09_Hydjet_MB/HINPbPbWinter16DR-75X_mcRun2_HeavyIon_v13_ext1-v1/AODSIM
/Pythia8_JpsiMM_ptJpsi_09_12_Hydjet_MB/HINPbPbWinter16DR-75X_mcRun2_HeavyIon_v13-v1/AODSIM
/Pythia8_JpsiMM_ptJpsi_12_15_Hydjet_MB/HINPbPbWinter16DR-75X_mcRun2_HeavyIon_v13-v1/AODSIM
/Pythia8_JpsiMM_ptJpsi_15_30_Hydjet_MB/HINPbPbWinter16DR-75X_mcRun2_HeavyIon_v13-v1/AODSIM
/Pythia8_JpsiMM_ptJpsi_30_Inf_Hydjet_MB/HINPbPbWinter16DR-75X_mcRun2_HeavyIon_v13-v1/AODSIM